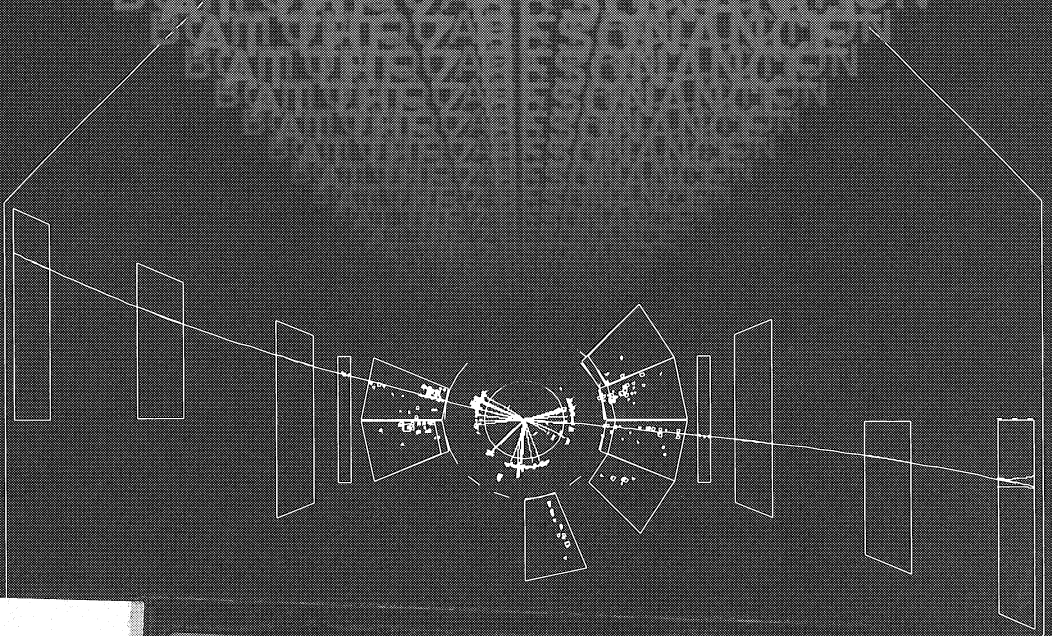


~~EX 10394~~

SW 94.11

# BOTTOM QUARK PRODUCTION AT THE Z RESONANCE



CERN LIBRARIES, GENEVA

CERN LIBRARIES, GENEVA



CM-P00068751

Thesis-1993-Foreman

Tim Foreman

# Bottom Quark Production at the Z Resonance

## ACADEMISCH PROEFSCHRIFT

TER VERKRIJGING VAN DE GRAAD VAN DOCTOR AAN  
DE UNIVERSITEIT VAN AMSTERDAM, OP GEZAG VAN  
DE RECTOR MAGNIFICUS PROF. DR. P.W.M. DE  
MEIJER IN HET OPENBAAR TE VERDEDIGEN IN DE  
AULA DER UNIVERSITEIT (OUDE LUTHERSE KERK,  
INGANG SINGEL 411, HOEK SPUI), OP DINSDAG 22  
JUNI 1993 TE 10.30 UUR.

door

**Tim Foreman**

geboren op 29 oktober 1964 te Haarlem

#177097

**PROMOTIECOMMISSIE:**

**Promotor:** Prof. Dr. P. Duinker  
**Copromotor:** Dr. V. Innocente

**Overige leden:**  
Prof. Dr. J. Engelen  
Prof. Dr. K.J.F. Gaemers  
Prof. Dr. A. Lagendijk  
Dr. G.G.G. Massaro  
Prof. Dr. A. Tenner  
Prof. Dr. B.Q.P.J. de Wit

FACULTEIT DER NATUUR- EN STERRENKUNDE

The work described in this thesis is part of the research program of the "Nationaal Instituut voor Kernfysica en Hoge-Energie Fysica (NIKHEF-H)" in Amsterdam. The author was financially supported by "Stichting voor Fundamenteel Onderzoek der Materie (FOM)".

ISBN: 90-9006217-3

*To Margret  
To Yuri*

# Contents

<b>Introduction</b>	<b>1</b>
<b>1 The theory</b>	<b>3</b>
1.1 The Standard Model . . . . .	4
1.2 The $b$ quark: an overview . . . . .	7
1.3 Cross sections . . . . .	9
1.4 Forward backward asymmetry . . . . .	13
1.5 $B^0\bar{B}^0$ oscillations . . . . .	15
1.6 Heavy flavour fragmentation . . . . .	17
1.7 Heavy flavour decay . . . . .	21
<b>2 The <math>L_3</math> experiment</b>	<b>25</b>
2.1 Introduction . . . . .	26
2.2 The muon detector . . . . .	28
2.3 The muon filter . . . . .	31
2.4 The hadron calorimeter . . . . .	31
2.5 The scintillation counters . . . . .	33
2.6 The electromagnetic calorimeter . . . . .	34
2.7 The central track detector . . . . .	35
2.8 The luminosity monitor . . . . .	36
2.9 The $L_3$ trigger . . . . .	37
2.10 The $L_3$ software packages . . . . .	40
2.11 LEP . . . . .	45
<b>3 The <math>L_3</math> muon reconstruction</b>	<b>49</b>
3.1 Introduction . . . . .	50
3.2 Simulation of muon tracks in the $L_3$ detector . . . . .	50
3.3 The $L_3$ muon reconstruction . . . . .	53
3.4 AMUI: combining all information . . . . .	73
3.5 The resolution of the muon chamber system . . . . .	74
3.6 Inefficiencies of reconstructed data muons with respect to Monte Carlo . . . . .	76
<b>4 Heavy flavour production</b>	<b>81</b>
4.1 Motivation . . . . .	82
4.2 Selection of $b\bar{b}$ events . . . . .	84
4.3 Trigger efficiency and data handling . . . . .	86
4.4 Monte Carlo simulation and classification . . . . .	87
4.5 Selection criteria . . . . .	88

4.6	Background . . . . .	93
4.7	Final event sample . . . . .	94
<b>5</b>	<b><math>B^0\bar{B}^0</math> Mixing</b>	<b>97</b>
5.1	Introduction . . . . .	98
5.2	Selection of dimuon events . . . . .	98
5.3	The counting method . . . . .	99
5.4	The four dimensional unbinned likelihood fit . . . . .	103
5.5	Determination of $\chi_s$ and CKM matrix elements . . . . .	105
<b>6</b>	<b>Forward backward asymmetry</b>	<b>111</b>
6.1	Introduction . . . . .	112
6.2	Event selection and angular distribution . . . . .	112
6.3	Simple fit method . . . . .	113
6.4	The two dimensional unbinned likelihood fit . . . . .	117
6.5	Determination of $\sin^2 \bar{\theta}_W$ . . . . .	120
<b>7</b>	<b>Measurement of <math>\text{Br}(b \rightarrow \mu + X)</math>, <math>\Gamma_{b\bar{b}}</math> and <math>\Gamma_{c\bar{c}}</math></b>	<b>123</b>
7.1	Introduction . . . . .	124
7.2	Determination of $\text{Br}(b \rightarrow \mu + X)$ . . . . .	124
7.3	Determination of CKM matrix element $ V_{cb} $ . . . . .	127
7.4	Determination of $\Gamma_{b\bar{b}}$ and $\Gamma_{c\bar{c}}$ . . . . .	129
	<b>Conclusion</b>	<b>133</b>
	<b>Appendix A</b>	<b>135</b>
	<b>References</b>	<b>139</b>
	<b>Summary</b>	<b>143</b>
	<b>Samenvatting</b>	<b>147</b>
	<b>Acknowledgements</b>	<b>151</b>
	<b>Curriculum Vitae</b>	<b>153</b>

# Introduction

The discovery, in 1983 at CERN, of the predicted intermediate vector bosons,  $W^\pm$  and the  $Z^0$ [1], has been a great success of the Standard Model, the theory describing the interactions between all fundamental particles. A drawback, however, is its large number of free parameters. Assuming the neutrinos to be massless, the Standard Model, containing three families is characterised by 18 parameters. These are three coupling constants, six quark masses, three lepton masses, three quark mixing angles and one phase and the mass and the vacuum expectation value of the Higgs particle. These parameters have to be determined experimentally. Before the discovery of the  $b$  quark, in 1977, only the three coupling constants, four quark masses, three lepton masses, one quark mixing angle, the so-called Cabibbo angle, and the weak mixing angle were known more or less accurately.

With the numerous  $Z^0$ 's produced with the Large Electron Positron collider, LEP, at CERN, some parameters of the Standard Model can be determined more and more accurately. This thesis describes the study of heavy flavour production and its implications on these Standard Model parameters. Heavy flavours are selected by the "lepton tagging" method. This method relies upon certain properties of the lepton to indicate the production of a heavy quark pair. Since the production of inclusive taus is very small and the tau life time very short as compared to muons and electrons, only the latter leptons are suited for this kind of analysis. The author of this thesis participated in the  $L_3$  inclusive muon analysis. Therefore, this thesis focuses on the part of the analysis that is done by muon tagging only.

The theory relevant for the analyses, presented in this thesis, is described in the first chapter. The second chapter describes the  $L_3$  experiment. Chapter 3 is devoted to the  $L_3$  muon simulation and reconstruction. In chapter 4, the event selection is discussed, followed by a detailed study of the Monte Carlo and data event samples thus obtained. The event selection is focused mainly on selecting  $e^+e^- \rightarrow b\bar{b}$  events, but as  $e^+e^- \rightarrow c\bar{c}$  events are not rejected rigorously by this selection, most of them are still present in the sample. The so-called mixing parameter,  $\chi_B$ , is determined in chapter 5. The determination of this parameter serves two purposes: it constrains the above mentioned quark mixing angles, also described in this chapter, and it allows us to calculate the forward backward asymmetry,  $A_{b\bar{b}}$ . The observed forward backward asymmetry,  $A_{b\bar{b}}^{\text{obs}}$ , is measured, which together with the mixing parameter gives  $A_{b\bar{b}}$ . Moreover, since the data contains  $c\bar{c}$  events, the forward backward asymmetry for  $e^+e^- \rightarrow c\bar{c}$ ,  $A_{c\bar{c}}$ , can also be measured and the description of these computations can be found in chapter 6. Having obtained  $A_{b\bar{b}}$ , the Standard Model weak mixing angle and the top quark mass are calculated. The branching ratio  $\text{Br}(b \rightarrow \mu + X)$  is determined in chapter 7. Like the mixing parameter, this quantity serves two purposes as well: it constrains the quark mixing angles and it allows for determining the partial width of the  $Z^0$  decaying into a  $b\bar{b}$  pair,  $\Gamma_{b\bar{b}}$ , both described in the same chapter. Apart from  $\Gamma_{b\bar{b}}$ ,  $\Gamma_{c\bar{c}}$  is extracted from the data. This thesis ends with a chapter devoted to drawing conclusions from the performed analyses.

In relativistic quantum field theory it is convenient to choose both the velocity of light in vacuum and Planck's constant dimensionless and equal to unity ( $c = \hbar = 1$ ). These factors will be suppressed in the formulae in this thesis. With this convention only one dimensional unit remains: for example length may be chosen, in which case mass parameters have dimension  $[\text{length}]^{-1}$ , or one may adopt mass as the basic unit so that length and time have dimension  $[\text{mass}]^{-1}$ .



# Chapter 1

## The theory

and the differential Born cross section for  $e^+e^- \rightarrow ff$  changes to [11]:

$$\frac{d\sigma}{d\Omega} = \frac{\alpha^2}{4s} \beta^2 \left\{ Q_f^2 [1 + \cos^2\theta + (1 - \beta^2) \sin^2\theta] \right. \quad (1.5)$$

$$- 8Q_f \lambda_1 (v_e v_f [1 + \cos^2\theta + (1 - \beta^2) \sin^2\theta] - \beta a_f \cos\theta)$$

$$+ 4\lambda_2 (v_f^2 (1 + 4v_f^2) [1 + \cos^2\theta + (1 - \beta^2) \sin^2\theta]$$

$$\left. + \beta^2 a_f^2 (1 + 4v_f^2) [1 + \cos^2\theta] - 16\beta v_e v_f a_f \cos\theta \right\}$$

with

$$\lambda_1 = \frac{1}{16 \sin^2 \theta_W \cos^4 \theta_W} \frac{s(s - M_Z^2)}{(s - M_Z^2)^2 + \Gamma_Z^2 M_Z^2} \quad (1.6)$$

$$\lambda_2 = \frac{1}{256 \sin^4 \theta_W \cos^4 \theta_W} \frac{1}{(s - M_Z^2)^2 + \Gamma_Z^2 M_Z^2}$$

Figure 1.4 shows the Feynman diagram which together with figure 1.3 corresponds to equation 1.5.

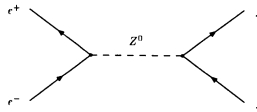


Figure 1.4: First order Feynman diagrams corresponding to the reaction  $e^+e^- \rightarrow Z^0 \rightarrow ff$ .

tion 1.5.

QED corrections, which include initial and final state photon radiation, are of utmost importance. Initial state photon radiation has a strong influence on the cross section around the  $Z^0$  resonance ( $\approx 35\%$  [12]). QCD radiative gluon corrections, affecting only the final state, give a correction of approximately 4% to the total cross section for heavy flavours [12].

Higher order corrections to the diagrams above, such as final state fermion mass effect, vacuum polarisation corrections of propagators and vertex corrections, shown schematically in figure 1.5, play an important role and have to be accounted for. These corrections can be taken into account by redefining the constants involved in the Born formulae, yielding the so-called improved Born formalism.

For heavy flavour production, the improved Born cross section, is given by [12, 13]:

$$\sigma = \beta \frac{3 - \beta^2}{2} \sigma^{VV} + \beta^3 \sigma^{AA} = \sigma_H^V + \sigma_H^A \quad (1.7)$$

## 1.1 The Standard Model

The Standard Model, which describes the interactions between all (known) fundamental particles<sup>1</sup>, is based on the gauge group  $SU_C(3) \times SU_L(2) \times U_Y(1)$ . The groups  $SU_C(3)$  and  $SU_L(2) \times U_Y(1)$  describe a specific part of the Standard Model and have their own typical gauge coupling constants. The group  $SU_L(2) \times U_Y(1)$  corresponds to the unification of the quantum mechanical extension of Maxwell's electromagnetic theory (called quantum electrodynamics or QED, specifying the interactions between the fundamental particles and the photon) and the theory describing the weak force, which is, for instance, responsible for the instability of many nuclei through  $\beta$ -decay.  $SU_L(2) \times U_Y(1)$  is referred to as the Standard Model of the electroweak theory [2]. The group  $SU_C(3)$  describes the strong interaction between the coloured quarks and gluons. This part of the Standard Model is referred to as quantum chromodynamics or QCD.

The Standard Model, in its present form, contains three types of fundamental particles:

### 1. The spin $\frac{1}{2}$ fermions: quarks and leptons

They are treated as pointlike particles which couple to the force carriers related to  $SU_C(3)$  and  $SU_L(2) \times U_Y(1)$ . Two quarks and two leptons together form a family. The number of families is not constrained by the Standard Model itself and therefore has to be determined by experiment. The number of light neutrino families has been determined by the four LEP experiments [3] to be  $3.00 \pm 0.05$ . Assuming that all neutrinos are massless, this implies that the number of families equals three. Hence, the number of fermions equals twelve, see table 1.1. The main difference between quarks and leptons is the fact that

	Leptons		Quarks	
Charge $Q_f$	0	-1	$\frac{2}{3}$	$-\frac{1}{3}$
Isospin $I_3^f$	$\frac{1}{2}$	$-\frac{1}{2}$	$\frac{1}{2}$	$-\frac{1}{2}$
1st family	$\nu_e$	$e$	$u$	$d$
2nd family	$\nu_\mu$	$\mu$	$c$	$s$
3rd family	$\nu_\tau$	$\tau$	$t$	$b$

Table 1.1: *The left handed leptons and quarks as arranged in the three families. The charge is in units of positron charge.*

only quarks take part in the strong interaction, because only they have a colour charge, the charge related to the strong force. In the Standard Model the left handed quarks and leptons are arranged in three doublets whereas the right handed quarks and leptons are

<sup>1</sup>The quantisation of the gravitational force has not yet resulted in a satisfactory addition to the Standard Model.

arranged in singlets.

## 2. The spin 1 gauge bosons: the force carriers

These are the eight coloured gluons  $g$  belonging to  $SU_C(3)$ , the charged vector bosons  $W^\pm$ , the neutral vector boson  $Z^0$  and the electromagnetic force carrier, the photon  $\gamma$ , of  $SU_L(2) \times U_Y(1)$  (see table 1.2).

Force	Mediator
Strong	massless gluons ( $g$ )
Electromagnetic	massless photon ( $\gamma$ )
Weak	massive intermediate vector bosons ( $W^\pm, Z^0$ )

Table 1.2: *The three Standard Model forces and their associated mediators.*

## 3. The neutral spin 0 Higgs boson: $H$

All particles are assumed to get their mass by interacting with the Higgs field. The neutrinos, the gluons and the photon form an exception, since they are assumed to be massless. The principle describing the mass generation for the vector bosons is called the Higgs mechanism and proceeds through so-called spontaneous symmetry breaking [4]. The fermion masses are generated by Yukawa couplings to the Higgs field. The Standard Model does not predict the mass of this Higgs boson and for as long as this particle is not found, this part of the theory remains speculative.

In the Standard Model with three families, the bottom quark plays an important role. The  $b$  quark was proposed as the fifth quark in 1973 by Kobayashi and Maskawa [5], together with the as yet unobserved sixth quark, the top quark. The six quarks were also needed to restore lepton quark symmetry after the discovery of the third lepton, the  $\tau$  [6]. The existence of the  $b$  quark was experimentally confirmed in 1977 with the discovery of the  $\Upsilon$  resonances, which are bound states of a  $b$  quark and its antiquark  $\bar{b}$  [7]. Over the last fifteen years, the knowledge of the  $b$  quark properties has become more and more detailed, both through the investigation of the  $\Upsilon$  resonances and, especially, through the study of the weak decays of  $B$  mesons which contain a  $\bar{b}$  quark. The year 1987, in particular, was fruitful with the observation of  $B^0\bar{B}^0$  oscillations [8].

The weak interaction quark eigenstates are mixtures of the flavour (mass) eigenstates. This implies that the weak interaction, contrary to the electromagnetic and strong interactions, violates flavour conservation. Such a violation does not occur in the lepton sector provided that the neutrinos are massless. The transformation between the weak and flavour eigenstates is described by the quark mixing matrix, the Cabibbo-Kobayashi-Maskawa (CKM) matrix  $V$ , which generalises the four quark case, where the matrix is

parametrised by a single angle  $\theta$ , the Cabibbo angle. By convention, the charge  $\frac{2}{3}$  quarks ( $u, c, t$ ) are unmixed and all the mixing is expressed in terms of the matrix  $V$  operating on the charge  $-\frac{1}{3}$  quarks ( $d, s, b$ ):

$$\begin{pmatrix} d' \\ s' \\ b' \end{pmatrix} = V \begin{pmatrix} d \\ s \\ b \end{pmatrix} = \begin{pmatrix} V_{ud} & V_{us} & V_{ub} \\ V_{cd} & V_{cs} & V_{cb} \\ V_{td} & V_{ts} & V_{tb} \end{pmatrix} \begin{pmatrix} d \\ s \\ b \end{pmatrix} \quad (1.1)$$

This unitary  $3 \times 3$  matrix with complex elements is determined by three angles and one phase, which possibly accounts for the observed CP violation in the  $K$  meson system. The strength of the coupling between the charge  $-\frac{1}{3}$  and charge  $\frac{2}{3}$  quarks is then given by the elements of the CKM matrix. The coupling between the quarks is illustrated in figure 1.1. In this figure only flavour changing charged currents are allowed. Flavour changing neutral currents are absent in the lowest order perturbation theory. This is retained in the unitarity of the CKM matrix.

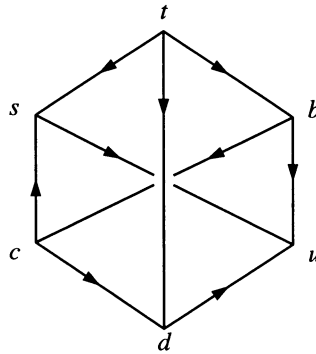
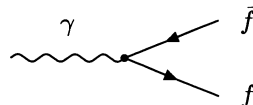


Figure 1.1: The allowed transitions between the six quarks in the Standard Model with three families.

At the time the Standard Model of the electroweak interactions was developed, it was realised that, in addition to the charged weak currents, neutral weak currents had to exist, in order to keep the theory renormalisable. Thus, apart from the electromagnetic neutral current, another neutral current had to play a role in the description of the electroweak interactions. Since both neutral currents couple to the fundamental fermions, the so-called weak mixing angle  $\theta_W$  was introduced to describe the relation between the weak and electromagnetic neutral currents. In terms of this angle  $\theta_W$  and the electric charge  $e$  of the positron, the couplings of the fermions to the massive  $W$  and  $Z$  bosons and the massless photon  $\gamma$  can be written as follows [9]:

- $-ieQ_f\gamma_\mu :$



$$\bullet \quad ie\gamma_\mu(v_f - a_f\gamma_5) \frac{1}{2\sin\theta_W \cos\theta_W} : \quad \begin{array}{c} Z^0 \\ \text{---} \end{array} \begin{array}{l} \nearrow \bar{f} \\ \searrow f \end{array}$$

$$\bullet \quad ie\gamma_\mu(1 - \gamma_5) \frac{1}{2\sqrt{2}\sin\theta_W} : \quad \begin{array}{c} W^\pm \\ \text{---} \end{array} \begin{array}{l} \nearrow \bar{f}' \\ \searrow f \end{array}$$

in which  $\gamma_i$  with ( $i = 1, 2, 3, 4, 5$ ) are the Dirac  $\gamma$ -matrices. The vector and axial vector coupling constants  $v_f$  and  $a_f$  are defined by:

$$v_f = I_3^f - 2Q_f \sin^2 \theta_W \quad \text{and} \quad a_f = I_3^f \quad (1.2)$$

The subscript  $f$  refers to the particular fermion produced,  $Q_f$  is its electromagnetic charge in units of the positron charge and  $I_3^f$  the third component of the fermion weak isospin, a quantum number reflecting the  $SU_L(2)$  symmetry of the electroweak interactions. The mixing angle  $\theta_W$  is given by the relation between the masses of the  $W$  and  $Z$  bosons:

$$\sin^2 \theta_W = 1 - \frac{M_W^2}{M_Z^2} \quad (1.3)$$

A remarkable aspect of the Standard Model is that the three coupling constants are not real constants but they are said to be running. This means that their values change with the energy scale at which the interaction takes place. Even more remarkable is the fact that two of them become stronger ( $U_Y(1)$  and  $SU_L(2)$ ) and the other becomes weaker ( $SU_C(3)$ ) as the energy increases. This effect is a consequence of renormalisation in a Yang-Mills theory.

## 1.2 The $b$ quark: an overview

The investigation of  $B$  hadrons, i.e. hadrons containing a  $b$  quark, allows for the determination of five more parameters of the Standard Model. These are the masses of the  $b$  and (indirectly) the  $t$  quarks, which together represent the third family, two quark mixing angles and the phase  $\delta$ , which could be responsible for the CP violation. These quantities can be determined by measuring the lifetime and the semileptonic branching ratios of  $B$  hadrons, by studying flavour oscillations in the neutral  $B$  meson system and by searching for rare  $B$  decays. For the determination of the mass of the  $t$  quark from  $b$  quark related physics, theoretical input is needed. The best way to determine this mass is the direct method of studying states with a  $t$  quark. Then only the determination of the mass of the Higgs boson remains in order to fix all the parameters of the Minimal Standard Model.

$\Upsilon (b\bar{b})$ mass (in MeV)	
$\Upsilon(1S)$	$9460.32 \pm 0.22$
$\Upsilon(2S)$	$10023.30 \pm 0.31$
$\Upsilon(3S)$	$10355.3 \pm 0.5$
$\Upsilon(4S)$	$10580.0 \pm 3.5$
$B^\pm (u\bar{b})$	
Mass	$5277.6 \pm 1.4$ MeV
Mean lifetime	$(11.8 \pm 1.1) 10^{-13}$ s $c\tau_B = 0.35$ mm
$B^0 (d\bar{b})$	
Mass	$5279.4 \pm 1.5$ MeV
$\tau_{B^0}/\tau_{B^+}$	0.44 to 2.05, at 90% C.L.
$B$	
$\text{Br}(b \rightarrow \ell + X)$	$(23.1 \pm 1.1)$ %
$\text{Br}(b \rightarrow e + X)$	$(12.1 \pm 0.6)$ %
$\text{Br}(b \rightarrow \mu + X)$	$(11.0 \pm 0.9)$ %

Table 1.3: Some of the properties of the  $b$  quark system as known before the startup of LEP and SLC.

Furthermore, the importance of  $b$  quark related physics lies in the fact that its investigation allows for valuable tests of the validity of the Standard Model. Certain processes which are induced by loop diagrams, such as flavour oscillations in the neutral  $B$  system or rare decays of  $B$  mesons, are also sensitive to physics beyond the Standard Model with three generations. The observation of CP violation in the  $B$  system will certainly shed light on this important phenomenon, which so far has not been fully understood. In this respect, the physics of  $B$  mesons is complementary to that of the  $K$  mesons, which has contributed enormously to our understanding of elementary particles and their interactions.

Information on  $B$  mesons and their decays has been obtained mainly by studying  $B$  mesons from the decay of the  $\Upsilon(4S)$  meson that is produced in  $e^+e^-$  annihilations at the CESR and DORIS  $e^+e^-$  storage rings. Since the  $B$  mesons at CESR and DORIS are produced (almost) at rest, lifetime measurements could only be made at the higher energy  $e^+e^-$  machines PETRA and PEP. For this reason, proposals for possible future high luminosity  $\Upsilon(4S)$  machines contain beams with unequal energies. This will cause the produced  $B$  mesons to travel a measurable distance in a laboratory system.  $B^0\bar{B}^0$  oscillations have been studied at all  $e^+e^-$  machines and at the CERN and Fermilab  $p\bar{p}$  colliders.

Table 1.3 shows the properties of the  $b$  quark system as they were known before the advent of LEP and SLC [10]. From this table one can see that a pair of  $B$  mesons can most efficiently be produced from the  $\Upsilon(4S)$  or higher state. The lower  $\Upsilon$  states can only decay

through a three gluon decay mode which gives a very narrow width; for instance the width of the  $\Upsilon(1S)$  resonance is  $52.1 \pm 2.1$  keV, which is very small compared to the width of the  $\Upsilon(4S)$  resonance which is approximately  $23.8 \pm 2.2$  MeV.

## 1.3 Cross sections

For pointlike spin  $\frac{1}{2}$  fermions in the centre of mass system, the differential Born, i.e. to first order in perturbation, cross section for  $e^+e^- \rightarrow f\bar{f}$  via single photon annihilation is [11]:

$$\frac{d\sigma}{d\Omega} = \frac{\alpha^2}{4s} \beta \left[ 1 + \cos^2 \theta + (1 - \beta^2) \sin^2 \theta \right] Q_f^2 \quad (1.4)$$

where  $\beta$  is the velocity of the final state fermion in the centre of mass system and  $\theta$  is defined in figure 1.2.

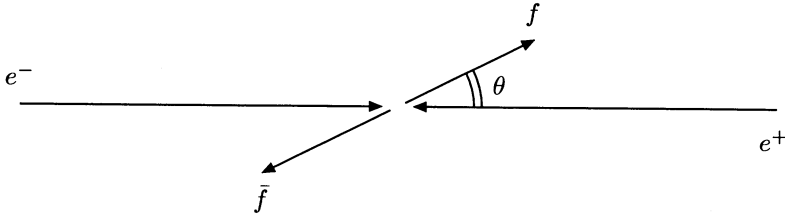


Figure 1.2: Definition of the production angle  $\theta$ : the opening angle between the fermion and the  $e^-$  direction.

In this equation  $\alpha = \alpha(s)$  is the running QED coupling constant,  $\alpha(M_Z^2) \approx 1/128$ , and  $s$  is the centre of mass energy squared. Figure 1.3 shows the corresponding Feynman

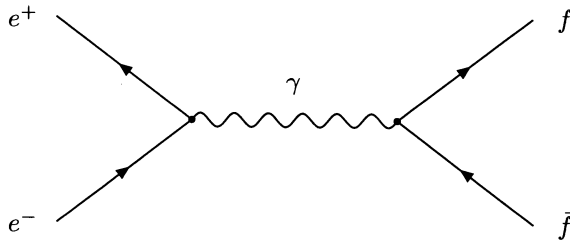


Figure 1.3: First order Feynman diagram corresponding to the reaction  $e^+e^- \rightarrow \gamma \rightarrow f\bar{f}$ .

diagram of equation 1.4.

At higher energies, the  $Z^0$ , with mass  $M_Z$  and width  $\Gamma_Z$ , must be taken into account

and the differential Born cross section for  $e^+e^- \rightarrow f\bar{f}$  changes to [11]:

$$\begin{aligned} \frac{d\sigma}{d\Omega} = \frac{\alpha^2}{4s} \beta \left\{ & Q_f^2 [1 + \cos^2 \theta + (1 - \beta^2) \sin^2 \theta] \right. \\ & - 8Q_f \chi_1 \left( v_e v_f [1 + \cos^2 \theta + (1 - \beta^2) \sin^2 \theta] - \beta a_f \cos \theta \right) \\ & + 4\chi_2 \left( v_f^2 (1 + 4v_e^2) [1 + \cos^2 \theta + (1 - \beta^2) \sin^2 \theta] \right. \\ & \left. \left. + \beta^2 a_f^2 (1 + 4v_e^2) [1 + \cos^2 \theta] - 16\beta v_e v_f a_f \cos \theta \right) \right\} \end{aligned} \quad (1.5)$$

with

$$\begin{aligned} \chi_1 &= \frac{1}{16 \sin^2 \theta_W \cos^2 \theta_W} \frac{s(s - M_Z^2)}{(s - M_Z^2)^2 + \Gamma_Z^2 M_Z^2} \\ \chi_2 &= \frac{1}{256 \sin^4 \theta_W \cos^4 \theta_W} \frac{s^2}{(s - M_Z^2)^2 + \Gamma_Z^2 M_Z^2} \end{aligned} \quad (1.6)$$

Figure 1.4 shows the Feynman diagram which together with figure 1.3 corresponds to equation 1.5.

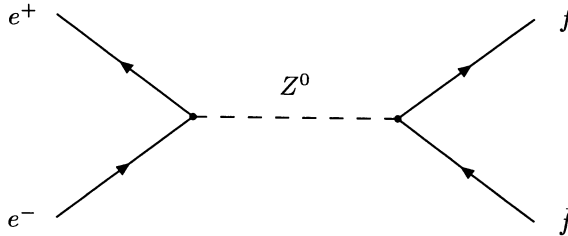


Figure 1.4: First order Feynman diagrams corresponding to the reaction  $e^+e^- \rightarrow Z^0 \rightarrow f\bar{f}$ .

tion 1.5.

QED corrections, which include initial and final state photon radiation, are of utmost importance. Initial state photon radiation has a strong influence on the cross section around the  $Z^0$  resonance ( $\approx 35\%$  [12]). QCD radiative gluon corrections, affecting only the final state, give a correction of approximately 4% to the total cross section for heavy flavours [12].

Higher order corrections to the diagrams above, such as final state fermion mass effect, vacuum polarisation corrections of propagators and vertex corrections, shown schematically in figure 1.5, play an important role and have to be accounted for. These corrections can be taken into account by redefining the constants involved in the Born formulae, yielding the so-called improved Born formalism.

For heavy flavour production, the improved Born cross section, is given by [12, 13]:

$$\sigma = \beta \frac{3 - \beta^2}{2} \sigma^{VV} + \beta^3 \sigma^{AA} = \sigma_B^V + \sigma_B^A \quad (1.7)$$



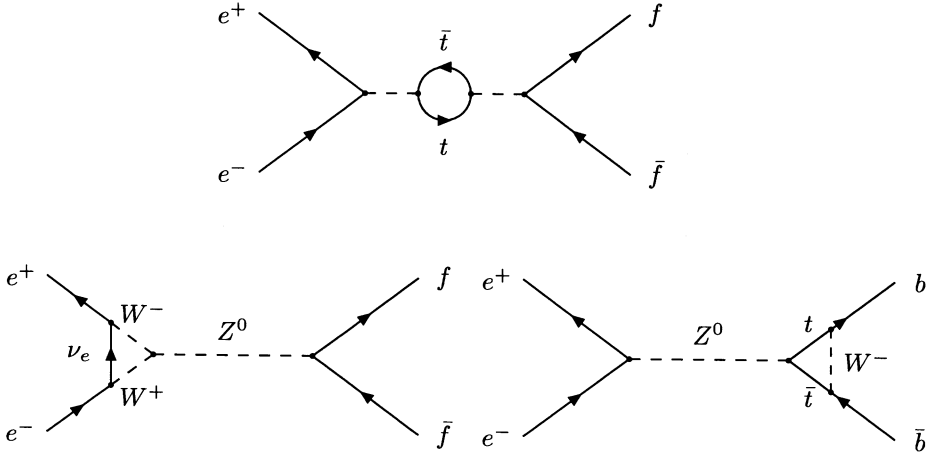


Figure 1.5: An example of a vacuum polarisation correction for the  $Z^0$  propagator and two vertex corrections.

with

$$\begin{aligned}
 \sigma^{VV} &= \frac{4\pi\alpha^2(M_Z^2)Q_e^2Q_f^2}{3s} \\
 &+ \frac{4\bar{G}_\mu\alpha(M_Z^2)}{\sqrt{2}}Q_eQ_f\bar{v}_e\bar{v}_f\frac{M_Z^2(s-M_Z^2)}{(s-M_Z^2)^2 + ([s/M_Z]\Gamma_Z)^2} \\
 &+ \frac{\bar{G}_\mu^2(\bar{v}_e^2 + \bar{a}_e^2)\bar{v}_f^2}{2\pi}\frac{M_Z^4s}{(s-M_Z^2)^2 + ([s/M_Z]\Gamma_Z)^2} \\
 \sigma^{AA} &= \frac{\bar{G}_\mu^2(\bar{v}_e^2 + \bar{a}_e^2)\bar{a}_f^2}{2\pi}\frac{M_Z^4s}{(s-M_Z^2)^2 + ([s/M_Z]\Gamma_Z)^2}
 \end{aligned} \tag{1.8}$$

in which  $\bar{G}_\mu$  is the effective muon decay constant. The effective electroweak vector and axial vector couplings,  $\bar{v}_f$  and  $\bar{a}_f$ , and the effective weak mixing angle,  $\sin^2\bar{\theta}_W$ , are expressed as:

$$\bar{a}_f = I_3^f + \frac{2}{3}\delta_{fb}\Delta\rho_t \quad \bar{v}_f = (I_3^f - 2Q_f\sin^2\bar{\theta}_W) + \frac{2}{3}\delta_{fb}\Delta\rho_t \tag{1.9}$$

and

$$\begin{aligned}
 \sin^2\bar{\theta}_{Wf} &= \sin^2\theta_W + \cos^2\theta_W\Delta\rho_t + \frac{\alpha}{4\pi}\left[\ln\left(\frac{M_H}{17.3}\right) + 1\right] - 2 \\
 \bar{G}_\mu &= G_\mu/(1 - \Delta\rho_t) \\
 \Delta\rho_t &= \frac{3\sqrt{2}G_\mu M_t^2}{16\pi^2} \\
 \delta_{fb} &= 1 \text{ for } b \text{ quarks and } 0 \text{ otherwise}
 \end{aligned} \tag{1.10}$$

The additional correction in equation 1.9 for the production of  $b\bar{b}$  pairs comes from top quark vertex corrections as shown in the lower right diagram in figure 1.5.

The effect of these corrections to the Born level cross section, calculated with the program ZFITTER [14], is shown in figure 1.6. ZFITTER uses analytical formulae to calculate cross sections, forward-backward asymmetries and angular distributions of final state fermions in  $e^+e^-$  interactions. It includes electroweak radiative corrections to  $\mathcal{O}(\alpha)$  and a common exponentiation of initial and final state bremsstrahlung. Furthermore, the  $\mathcal{O}(\alpha)$  corrections are supplemented with  $\mathcal{O}(\alpha, \alpha_s)$  and leading  $\mathcal{O}(\alpha^2 M_t^4/M_W^4)$  corrections from top quark insertions in the gauge boson self-energies.

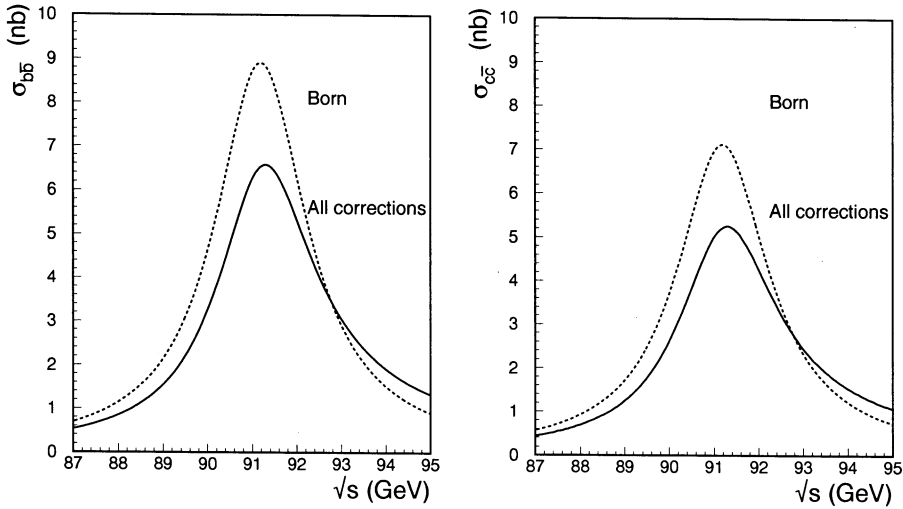


Figure 1.6: ZFITTER cross section predictions for the process  $e^+e^- \rightarrow b\bar{b}$  (left) and  $e^+e^- \rightarrow c\bar{c}$  (right). The dashed lines are the Born cross sections, the solid lines are the ones with full QED and QCD corrections. The integration has been performed over the angular region  $35^\circ < \theta < 145^\circ$ .

For many applications the improved Born approximation is an excellent description for the partial  $Z$  decay width into heavy quarks,

$$\Gamma_{q\bar{q}} = \beta \frac{3 - \beta^2}{2} \Gamma_{q\bar{q}}^V + \beta^3 \Gamma_{q\bar{q}}^A \quad (1.11)$$

with

$$\Gamma_{q\bar{q}}^V = \frac{\bar{G}_\mu M_Z^3}{2\sqrt{2}\pi} \bar{v}_q^2 \quad \text{and} \quad \Gamma_{q\bar{q}}^A = \frac{\bar{G}_\mu M_Z^3}{2\sqrt{2}\pi} \bar{a}_q^2 \quad (1.12)$$

where  $\bar{G}_\mu$ ,  $\bar{v}_q^2$  and  $\bar{a}_q^2$  are defined in equations 1.9 and 1.10. Final state photon and gluon emission are identical to those discussed above and the corrections are in the order of 0.05%

and 4% respectively [12]. The program ZFITTER predicts the following heavy flavour partial widths:

$$\Gamma_{b\bar{b}} = 376 \text{ MeV} \quad \text{and} \quad \Gamma_{c\bar{c}} = 297 \text{ MeV} \quad (1.13)$$

All electroweak predictions are obtained by using the parameters  $\sin \theta_W = 0.222$ ,  $M_Z = 91.181 \text{ GeV}$ ,  $M_t = 193 \text{ GeV}$ ,  $M_H = 300 \text{ GeV}$  [15] and  $\alpha_s = 0.115$  [16] unless specified otherwise.

Figure 1.7 shows  $\Gamma_{b\bar{b}}$  (left) and  $\Gamma_{b\bar{b}}/\Gamma_{\text{had}}$  (right) as a function of the mass of the top quark,  $M_t$ .

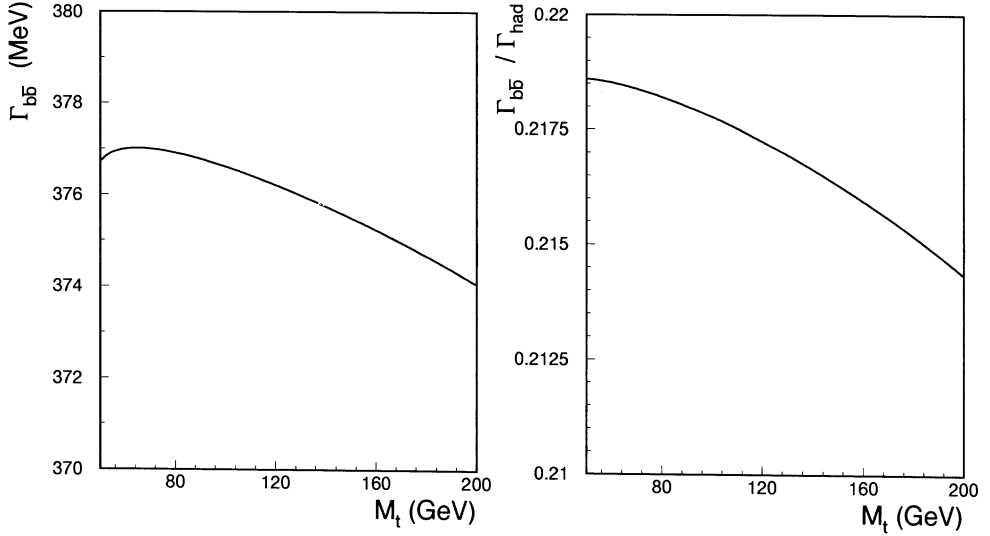


Figure 1.7:  $\Gamma_{b\bar{b}}$  (left) and  $\Gamma_{b\bar{b}}/\Gamma_{\text{had}}$  (right) as a function of the mass of the top quark,  $M_t$ .

## 1.4 Forward backward asymmetry

The forward backward asymmetry is defined as:

$$A_{FB} = \frac{\sigma_F - \sigma_B}{\sigma_F + \sigma_B} \quad (1.14)$$

with

$$\sigma_F = \int_0^1 d(\cos \theta) \frac{d\sigma}{d \cos \theta} \quad \text{and} \quad \sigma_B = \int_{-1}^0 d(\cos \theta) \frac{d\sigma}{d \cos \theta} \quad (1.15)$$

where the angle  $\theta$  is defined in figure 1.2. Integrating equation 1.5 over  $\phi$  gives  $d\sigma/d \cos \theta$ . From this equation it can be seen that:

$$\frac{d\sigma}{d \cos \theta} \sim (1 + \cos^2 \theta + \frac{8}{3} A_{FB} \cos \theta) \quad (1.16)$$

which demonstrates that  $A_{FB}$  is a result of the interference between the pure photon and  $Z^0$  boson exchange diagrams. In the improved Born approximation,  $A_{FB}$ , for the fermion of type  $f$ , can be cast into the form [13]:

$$A_{f\bar{f}} = \frac{3}{4} \frac{\beta^2 \sigma_f^{VA}}{\sigma_f} \quad (1.17)$$

in which  $\sigma^{VA}$  is defined by:

$$\begin{aligned} \sigma^{VA} &= \frac{4\bar{G}_\mu \alpha(M_Z^2)}{\sqrt{2}} Q_e Q_f \bar{a}_e \bar{a}_f \frac{M_Z^2 (s - M_Z^2)}{(s - M_Z^2)^2 + ([s/M_Z] \Gamma_Z)^2} \\ &+ \frac{2\bar{G}_\mu^2}{\pi} \bar{v}_e \bar{a}_e \bar{v}_f \bar{a}_f \frac{M_Z^4 s}{(s - M_Z^2)^2 + ([s/M_Z] \Gamma_Z)^2} \end{aligned} \quad (1.18)$$

On top of the  $Z^0$  resonance, the asymmetry is dominated by the pure  $Z^0$  amplitude.

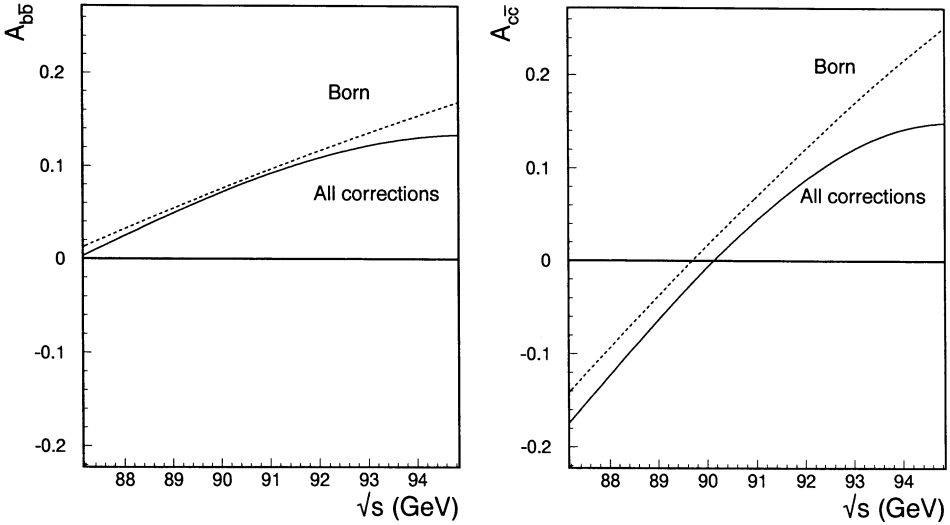


Figure 1.8: ZFITTER predictions for the forward backward asymmetries of  $e^+e^- \rightarrow b\bar{b}$  (left) and  $e^+e^- \rightarrow c\bar{c}$  (right) as a function of the centre of mass energy  $\sqrt{s}$ .

Therefore, to a very good approximation,

$$A_{f\bar{f}} = \frac{3}{4} \frac{2\bar{v}_e \bar{a}_e}{\bar{v}_e^2 + \bar{a}_e^2} \frac{2\bar{v}_f \bar{a}_f}{\bar{v}_f^2 + \bar{a}_f^2} = \frac{3}{4} A_e A_f \quad (1.19)$$

which defines the quantity  $A_f$ :

$$A_f = \frac{2\bar{v}_f \bar{a}_f}{\bar{v}_f^2 + \bar{a}_f^2} \quad (1.20)$$

Figure 1.8 shows the forward backward asymmetries for  $e^+e^- \rightarrow b\bar{b}$  (left) and  $e^+e^- \rightarrow c\bar{c}$  (right) as a function of the centre of mass energy  $\sqrt{s}$ , as predicted by the program ZFITTER, with and without higher order corrections.

## 1.5 $B^0\bar{B}^0$ oscillations

Investigating the oscillations in the neutral  $B$  meson systems, i.e.  $B_d^0\bar{B}_d^0$  and  $B_s^0\bar{B}_s^0$ , will provide constraints on the parameters of the Standard Model. In particular, the CKM matrix elements  $V_{td}$  and  $V_{ts}$  can be obtained from this analysis. Massive or exotic virtual particles can also contribute to the amount of mixing and this makes the mixing phenomenon sensitive to physics beyond the Standard Model [17].

Oscillations in the neutral  $B$  meson systems proceed via box diagrams as shown in figure 1.9. The  $B_q^0\bar{B}_q^0$  system can be described by the following phenomenological Hamiltonian matrix  $H$ :

$$H \begin{pmatrix} B_q^0 \\ \bar{B}_q^0 \end{pmatrix} = \begin{pmatrix} M_q - \frac{1}{2}i\Gamma_q & p_q^2 \\ q_q^2 & M_q - \frac{1}{2}i\Gamma_q \end{pmatrix} \begin{pmatrix} B_q^0 \\ \bar{B}_q^0 \end{pmatrix} \quad (1.21)$$

The diagonal elements in this matrix describe the decay of the  $B_q^0$  ( $\bar{B}_q^0$ ) meson with  $M_q$  and  $\Gamma_q$ , the mass and the decay width of the meson respectively. The off-diagonal elements are responsible for the  $B_q^0\bar{B}_q^0$  mixing:

$$\begin{aligned} p_q^2 &= \langle B_q^0 | H | \bar{B}_q^0 \rangle \\ q_q^2 &= \langle \bar{B}_q^0 | H | B_q^0 \rangle \end{aligned} \quad (1.22)$$

The quantities  $p_q^2$  and  $q_q^2$  can be evaluated by calculating the box diagrams from figure 1.9.

By diagonalising  $H$  the mass eigenstates can be determined:

$$|B_q^{1,2}\rangle = \frac{1}{\sqrt{|p_q|^2 + |q_q|^2}} \left( |p_q\rangle |B_q^0\rangle \pm |q_q\rangle |\bar{B}_q^0\rangle \right) \quad (1.23)$$

If  $p_q \neq q_q$  then  $|B_q^{1,2}\rangle$  are not eigenstates of CP since:

$$\langle B_q^1 | B_q^2 \rangle = \frac{|p_q|^2 - |q_q|^2}{|p_q|^2 + |q_q|^2} \neq 0 \quad (1.24)$$

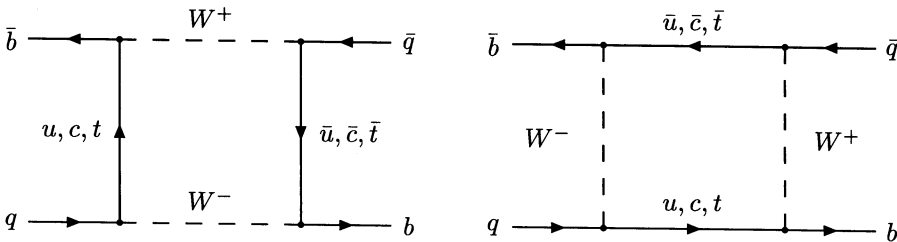


Figure 1.9: Box diagrams for  $B_q^0\bar{B}_q^0$  transitions.

In the context of the Standard Model, this effect has been shown to have an order of magnitude of about  $10^{-3}$  to  $10^{-4}$  [12].

Neglecting CP violations in the neutral  $B$  meson system (i.e.  $p_q = q_q$ ), the mass eigenstates  $B_q^1$  and  $B_q^2$ , obtained by diagonalising matrix  $H$ , are linear combinations of the flavour eigenstates:

$$|B_q^{1,2}\rangle = \frac{1}{\sqrt{2}} \left( |B_q^0\rangle \pm |\bar{B}_q^0\rangle \right) \quad (1.25)$$

with mass  $M_{1,2}$  and decay rate  $\Gamma_{1,2}$  where

$$\begin{aligned} M_{1,2} &= M_q \pm \frac{1}{2} \Delta M_q \quad \text{with} \quad \Delta M_q = \text{Re}(p_q^2) \\ \Gamma_{1,2} &= \Gamma_q \pm \frac{1}{2} \Delta \Gamma_q \quad \text{with} \quad \Delta \Gamma_q = 2 \text{Im}(p_q^2) \end{aligned} \quad (1.26)$$

The oscillation frequency between the  $B_q^0$  and  $\bar{B}_q^0$  flavour eigenstates is proportional to the mass difference between the two mass eigenstates,  $\Delta M_q$ . For this mass difference one obtains [17]:

$$\Delta M_q = \frac{G_F^2}{6\pi^2} B_{B_q} f_{B_q}^2 M_{B_q} |V_{tb}^* V_{tq}|^2 M_t^2 \mathcal{F} \left( \frac{M_t^2}{M_W^2} \right) \eta_{\text{QCD}} \quad (1.27)$$

with

$$\mathcal{F}(x) = \frac{x}{4} \left( 1 + \frac{3-9x}{(1-x)^2} + \frac{6x^2 \ln(x)}{(1-x)^3} \right) \quad (1.28)$$

where  $B_{B_q}$  is the so-called bag parameter and  $f_{B_q}$  the  $B_q$  decay constant:  $B_{B_q}^{1/2} f_{B_q} = 140 \pm 40 \text{ MeV}$  [17].  $M_{B_q}(M_t)$  is the mass of the  $B_q$  meson ( $t$  quark) and  $\eta_{\text{QCD}}$  is a QCD correction factor,  $\eta_{\text{QCD}} \approx 0.85$ .

The amount of mixing is measured by determining the mixing parameter  $\chi_q$ :

$$\chi_q = \frac{P(B_q^0 \rightarrow \bar{B}_q^0)}{P(B_q^0 \rightarrow B_q^0) + P(\bar{B}_q^0 \rightarrow \bar{B}_q^0)} = \frac{x_q^2 + y_q^2}{2(1 + x_q^2)} \quad (1.29)$$

in which  $x_q = \Delta M_q / \Gamma_q$  and  $y_q = \Delta \Gamma_q / 2\Gamma_q$ . Unlike for  $K^0$  mesons, where  $\Delta \Gamma \approx \Gamma$ , for  $B^0$  mesons  $\Delta \Gamma_q \ll \Delta M_q$  [12]. This implies that:

$$\chi_q = \frac{x_q^2}{2(1 + x_q^2)} \quad (1.30)$$

By measuring  $\chi_q$ ,  $\Delta M_q$  can be calculated, via equation 1.30. This, together with equation 1.27, gives information about the CKM matrix elements.

If discrimination between the various hadrons containing  $b$  quarks is not possible, as is the case in the analysis described in this thesis, not  $\chi_q$  but  $\chi_B$  is measured:

$$\chi_B = \frac{Br(b \rightarrow B \rightarrow \bar{B})}{Br(b \rightarrow B)} = \frac{Br(b \rightarrow B^0 \rightarrow \bar{B}^0)}{Br(b \rightarrow B)}$$

$$\begin{aligned}
&= \frac{Br(b \rightarrow B_s^0) Br(b \rightarrow B_s^0 \rightarrow \bar{B}_s^0)}{Br(b \rightarrow B) Br(b \rightarrow B_s^0)} \\
&+ \frac{Br(b \rightarrow B_d^0) Br(b \rightarrow B_d^0 \rightarrow \bar{B}_d^0)}{Br(b \rightarrow B) Br(b \rightarrow B_d^0)} \\
&= f_s \chi_s + f_d \chi_d
\end{aligned} \tag{1.31}$$

The relative abundances  $f_d$  and  $f_s$  in this equation are assumed to be 0.40 and 0.12 respectively. These values correspond to a strange quark suppression factor  $\gamma_s = f_s/f_d = 0.3$ , which is consistent with measurements at LEP [18] and lower energy  $e^+e^-$  colliders [19, 20]. Assuming  $f_u = f_d$ , a  $b$ -baryon fraction of  $f_B = 0.08$  is implied.

In the analysis described in this thesis, the  $b$  quarks are tagged by their semileptonic decay into muons. Thus what is really measured is:

$$\chi'_B = \frac{Br(b \rightarrow B \rightarrow \bar{B} \rightarrow \mu X)}{Br(b \rightarrow B \rightarrow \mu X)} \tag{1.32}$$

which, under the assumption that all hadrons containing a  $b$  quark have the same semileptonic branching ratio, equals  $\chi_B$ .

If CP violations can not be neglected, there will be an asymmetry in  $P(B_q^0 \rightarrow \bar{B}_q^0)$  versus  $P(\bar{B}_q^0 \rightarrow B_q^0)$  and, as a consequence, an asymmetry in the number of positive dimuons compared to the number of negative dimuons coming from a semileptonic  $B$  decay.

Two methods are used to measure the mixing parameter  $\chi_B$ . These methods, their results and their implications will be described in chapter 5.

## 1.6 Heavy flavour fragmentation

Figure 1.10 schematically shows an  $e^+e^-$  annihilation in which the  $Z^0$  produces a quark antiquark pair, which generates a large number of hadrons in the final state. Depending on the energy scale  $Q^2$  of the interaction, this process can be split into four parts. The first part is described completely by the electroweak theory of the Standard Model. The other three parts are dominated by QCD. Part two can be calculated with perturbative QCD due to the fact that in this energy region the strong coupling constant,  $\alpha_s$ , is small. Two approaches to the modeling of perturbative QCD exist. One is the matrix element method, in which Feynman diagrams are calculated exactly, order by order. Because of the technical difficulties of these calculation, only the second order matrix element is presently available. Therefore, a maximum of four partons in the final state can be produced. The other approach is the parton shower method. In this method, an arbitrary number of partons are branched in order to yield a description of multi jet events, with no explicit upper limit on the number of partons involved. It is based on the approximation of the full matrix element expression. Part three and four, however, cannot be calculated using perturbative QCD, since at these energy scales the strong coupling constant is too large. At present, one has to rely on QCD inspired phenomenological models that are developed by combining simple kinematical considerations with the results from  $e^+e^-$  experiments. Part four in figure 1.10, the decay of unstable hadrons into experimentally visible particles, is completely described by empirical results such as measured branching ratios and masses of the produced particles.

The phenomenological models for heavy quarks are based on very simple kinematical considerations, which were first pointed out by Bjorken and Suzuki [21]. Attaching a light antiquark  $\bar{q}$  (or diquark  $qq$  for baryon production) to a heavy quark  $Q$  decelerates the heavy quark in this so-called fragmentation process only slightly. Thus  $Q$  and  $Q\bar{q}$  (or  $Qqq$ ) carry almost the same energy.

Where to draw the borderline between region two and three depends on the energy scale at which one can still perform perturbative QCD calculations to predict the interactions. As stated above, this depends on the size of the running strong coupling constant which in turn depends on the energy scale at which the interaction takes place: typically a few GeV. This means that, for heavy quarks,  $\alpha_s$  is smaller at the quark energy scale. Mele and Nason have taken advantage of this and have performed purely perturbative (next-to-leading) QCD calculations, where they show that, for heavy flavours, the simple kinematical considerations, as pointed out by Bjorken and Suzuki, are valid already at the perturbative level [22]. As non-perturbative effects cannot be neglected, purely perturbative QCD does not suffice and phenomenological models have to be used.

Three widely used phenomenological models are:

- the Colour String Fragmentation Model [23],
- the Independent Fragmentation Model [24] and
- the Cluster Fragmentation Model [25].

In the Colour String Fragmentation Model, fragmentation proceeds along so-called QCD inspired, colour-flux lines between quarks and gluons. As the distance between the quark

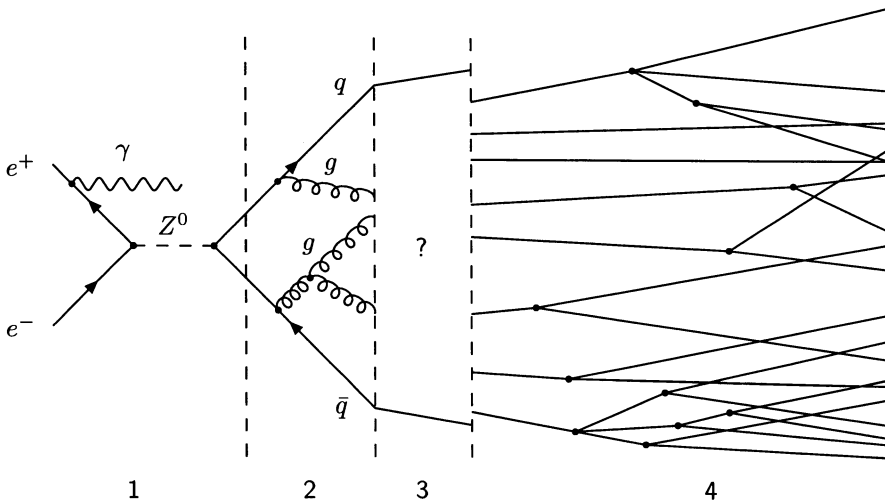


Figure 1.10: Schematic illustration of an  $e^+e^-$  annihilation where the  $Z^0$  produces a quark antiquark pair which generates a large number of hadrons in the final state.



and antiquark becomes bigger, this string is stretched and may eventually break, producing a new quark antiquark pair resulting into two new colourless systems. The sharing of energy and momentum between these new systems is given by a scaling function. The new systems may again break up, until only on-mass shell hadrons remain. The advantage of this model is that at all steps in the process, energy and momentum are conserved.

The Independent Fragmentation Model is carried out in almost the same manner as the Colour String Fragmentation Model. The sharing of energy and momentum, however, is done in isolation from each other, which results in violation of energy and momentum conservation during the fragmentation process. The independent fragmentation model was shown to fail to describe some experimental data [26].

In the Cluster Fragmentation Model, gluons from the perturbative phase are first split into quark and anti-quark pairs. The quark and anti-quark pairs then form colourless clusters which, depending on their masses, decay either into lower mass clusters or directly into particles. In the cluster fragmentation, the distributions of particle momenta are determined by the momenta of the clusters and their decay properties.

The fragmentation process in the first two models is parametrised by a scaling function  $f(z)$  where  $z$  is defined by

$$z = \frac{(E + p_{\parallel})_{\text{hadron}}}{(E + p)_{\text{quark}}} \quad (1.33)$$

$(E + p_{\parallel})_{\text{hadron}}$  is the sum of the energy and momentum component, parallel to the fragmentation direction carried by the primary hadron.  $(E + p)_{\text{quark}}$  is the energy-momentum of the quark.

Examples of  $f(z)$  are:

- Lund [27]:  $f(z) \propto \frac{1}{z}(1-z)^a \exp(-\frac{bM_T^2}{z})$
- Peterson [28]:  $f(z) \propto (z[1 - \frac{1}{z} - \frac{\epsilon_Q}{1-z}])^{-1}$

	Parameter	Value
Peterson	$\epsilon_Q$	0.535
Lund	$a$	0.500
	$b$	0.900
	$M_T^2$	0.250
Collins and Spiller	$\epsilon_Q$	0.807
Kartvelishvili	$\alpha_Q$	3.25

Table 1.4: Typical fragmentation parameters.

- Collins and Spiller [29]:  $f(z) \propto \left(\frac{1-z}{z} + \frac{2-z}{1-z}\epsilon_Q\right)(1+z^2)\left(1 - \frac{1}{z} - \frac{\epsilon_Q}{1-z}\right)^{-2}$
- Kartvelishvili [30]:  $f(z) \propto z^{\alpha_Q}(1-z)$

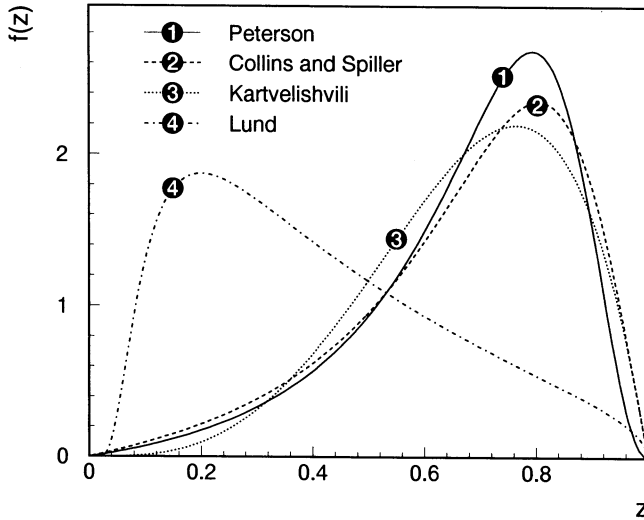


Figure 1.11: The four scaling functions as mentioned in the text. The parameters were chosen in such a way that the average  $z$  is the same for all distributions (0.68), except for the Lund scaling function which represents the distribution for a  $K$  meson.

In these equations,  $\epsilon_Q$ ,  $a$ ,  $b$  and  $\alpha_Q$  are the so-called fragmentation parameters and  $M_T$  the transverse mass defined by  $M_T^2 = m^2 + p_\perp^2$ . The Lund scaling function is well suited to describe the fragmentation of the light quarks, whereas it does not give a good description for heavy quark fragmentation. For this purpose, the other scaling functions are used. Figure 1.11 shows the four scaling functions with the fragmentation parameters as shown in table 1.4. The parameters were chosen in such a way that the average  $z$  is the same for all distributions (0.68), except for the Lund scaling function which represents the distribution for a  $K$  meson. The so-called hardness of the fragmentation is determined by this average value for  $z$ : the more this value is peaked towards 1.0, the harder the fragmentation.

The Peterson function has been widely adopted in analyses determining the hardness of heavy quark fragmentation functions; its biggest attraction being that it follows directly from the afore mentioned simple kinematical considerations, pointed out by Bjorken and Suzuki.

Although  $z$ , the quantity defined in equation 1.33, is the best choice to describe the fragmentation process theoretically (see [31]), it is difficult to be determined experimentally, since it is not possible to measure the energy and momentum of the primary quark directly.

Therefore numerous quantities approximating  $z$  are used in the literature, of which one has become particularly popular. This frequently used experimental variable is

$$x_E = \frac{E_{\text{hadron}}}{E_{\text{beam}}} \quad (1.34)$$

and is a directly measurable quantity.

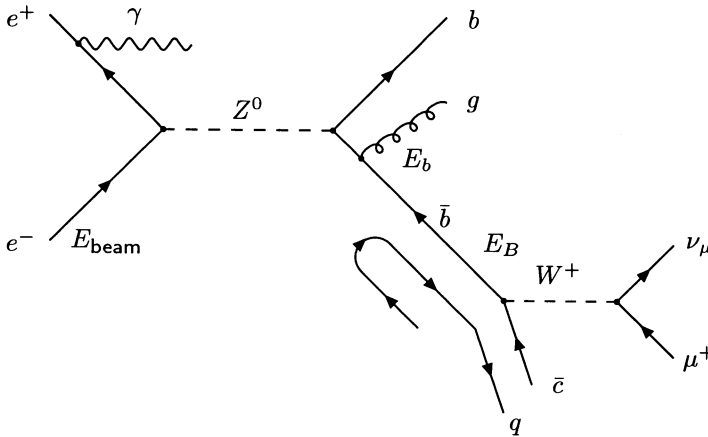


Figure 1.12: Schematic illustration of an  $e^+e^-$  annihilation where the  $Z^0$  produces a  $b\bar{b}$  pair, producing a  $B$  meson which decays semileptonic into a muon and neutrino.

In publications, often only  $\langle x_E \rangle_Q$  is quoted, assuming a scaling function  $f(x_E)$  to describe the fragmentation distribution. The drawback of this quantity lies in the fact that (initial and final) photon and gluon radiation will reduce the quark energy:  $E_{\text{quark}} \leq E_{\text{beam}}$ . As a consequence,  $\langle x_E \rangle_Q$  depends on the centre of mass energy of the experiment and on the Monte Carlo models used. This is schematically illustrated by figure 1.12.

Heavy flavours are well suited for studying the fragmentation mechanism since heavy quark pair production is suppressed during the process itself. Hence, a heavy quark is almost always a primary quark.

## 1.7 Heavy flavour decay

The description of weak decays of hadrons is complicated by the fact that the decaying quarks are not free particles, but bound by the strong force. Therefore, QCD effects have to be taken into account, making the weak decays of hadrons a testing ground for QCD as well.

For heavy mesons, such as  $B^0$  or  $B^+$ , an approximate description of their weak decays is given by the Spectator Model. In this model, the heavy  $b$  quark, e.g. in  $\bar{B}_d^0 = b\bar{d}$ , decays

into a lighter ( $c$  or  $u$ ) quark by emission of a  $W^-$  boson, while the  $\bar{d}$  quark, having no influence on the decay rate, acts as a spectator. Semileptonic decays are obtained if the  $W$  boson couples to a lepton  $\ell$  ( $\ell = e, \mu, \tau$ ) and its antineutrino. Figure 1.13 shows two examples of heavy meson decay in the Spectator Model.

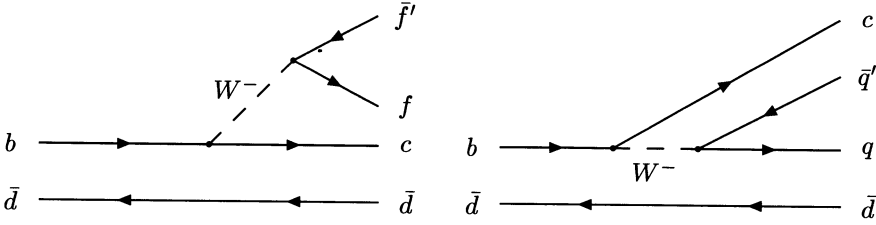


Figure 1.13: Two examples of heavy meson decay in the Spectator Model.

The semileptonic decay rate,  $\Gamma_{\text{sl}}$ , as calculated in the ACCMM model is [32]:

$$\Gamma_{\text{sl}} = \frac{G_F^2 m_b^5}{192\pi^3} \left\{ |V_{ub}|^2 \mathcal{I}\left(\frac{m_u}{m_b}, \frac{m_\ell}{m_b}, 0\right) \mathcal{F}_{\text{sl}}(b \rightarrow u) + |V_{cb}|^2 \mathcal{I}\left(\frac{m_c}{m_b}, \frac{m_\ell}{m_b}, 0\right) \mathcal{F}_{\text{sl}}(b \rightarrow c) \right\} \quad (1.35)$$

The function  $\mathcal{I}(x, y, z)$  describes the phase space corrections and  $\mathcal{F}_{\text{sl}}$  incorporates radiative gluon corrections:

$$\begin{aligned} \mathcal{I}(\epsilon_q, 0, 0) &= f_q \simeq (1 - 8\epsilon_q^2 + 8\epsilon_q^6 - \epsilon_q^8 - 24\epsilon_q^4 \ln \epsilon_q) \\ \mathcal{F}_{\text{sl}}(b \rightarrow q) &= \left(1 - \frac{2}{3} \frac{\alpha_s(m_b^2)}{\pi} \left[ (\pi^2 - \frac{31}{4})(1 - \epsilon_q)^2 + \frac{3}{2} \right] \right) \end{aligned} \quad (1.36)$$

where  $\epsilon_q = m_q/m_b$ .

To calculate  $\mathcal{I}$  and  $\mathcal{F}_{\text{sl}}$ , the following quark mass values are used:  $m_b = 4.95 \pm 0.07$  GeV and  $m_b - m_c = 3.30 \pm 0.02$  GeV. These values are obtained by the ARGUS Collaboration in the framework of the ACCMM model from a fit to the lepton momentum spectrum in semileptonic  $B$ -meson decays [33]. In order to include uncertainties in the model, the error on  $m_b$  is increased to  $\pm 0.3$  GeV and  $m_u = 0.2 \pm 0.2$  GeV is taken, keeping the above error on  $m_b - m_c$ . The value used for  $\alpha_s(m_b^2)$  is  $0.20 \pm 0.03$ , which has been obtained from extrapolating the  $L_3$  measured value at  $\sqrt{s} \approx M_Z$ ,  $\alpha_s = 0.115 \pm 0.009$  [16], to  $Q^2 = m_b^2$ . In this way, it is assumed that, in accordance with the spectator model, the light  $B$ -mesons produced at the  $\Upsilon(4S)$  have the same semileptonic widths as the heavier  $B$ -hadrons which can be produced from the  $Z^0$ :

$$\Gamma_{\text{sl}} = \frac{\text{Br}(b \rightarrow \ell X)}{\tau_B} = \frac{G_F^2 m_b^5}{192\pi^3} (0.84|V_{ub}|^2 + 0.40|V_{cb}|^2) \quad (1.37)$$

in which  $\tau_B$  is the average lifetime of all  $B$  hadrons.

In the Spectator Model lifetimes of charged and neutral hadrons should be the same. However in  $B$  decays, as in charmed particles, non-spectator effects can take place, such as interference effects due to the presence of identical quarks in the final state, flavour

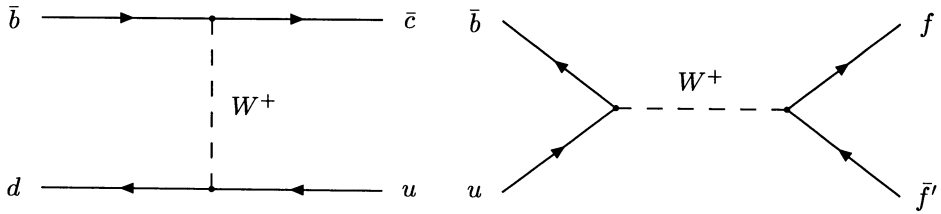


Figure 1.14: An example of  $W$  exchange in  $B^0$  decays and an example of flavour annihilation in  $B^+$  decays.

annihilation by  $W$  exchange or soft gluon effects. In figure 1.14 an example of  $W$  exchange in  $B^0$  decays and an example of flavour annihilation in  $B^+$  decays is displayed.

Generally, non-spectator effects are expected to decrease the lifetime and semileptonic branching ratios of the  $B^0$ . However, a difference of more than 10% is not expected, justifying the averaging of lifetimes and branching ratios for unknown mixtures of  $B$  particles [34].



# Chapter 2

## The L<sub>3</sub> experiment

### 2.2.2 The precision chambers

The momentum measuring, or "P" chambers, each contain a few hundred signal wires, the so-called sense wires, and a total of about 3000 field shaping wires. These wires are about 5.6 m long and are supported by three bridges, one at each end, precisely positioning the wires and one in the middle to reduce the gravitational sag of the wires to 96  $\mu\text{m}$ . The drift times measured by the wires are converted into digits by (multi hit) TDC's, time to digit converters. The cell structure of the chambers contain 16, 24 and 16 sense wires for the MI, MM and MO chamber respectively, each cell being exactly 101.500 mm wide, see figure 2.4.

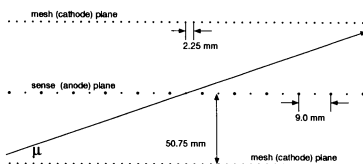


Figure 2.4: Wire configuration of a precision chamber cell. The open circles in the middle plane stand for the sense wires, the closed circles for the field (shaping) wires. The closed circles in the upper and lower wire plane are the mesh wires.

The chamber cell has been designed to have a uniform electric field throughout the active region. The sense wires are spaced 9 mm apart and interspaced with field wires. Three additional guard wires beyond the last sense wire equalize the drift time behaviour of the sense wire plane. A plane of cathode (mesh) wires spaced 2.25 mm apart, is at 50.75 mm from the sense wire plane.

The time-to-distance conversion function, called the cellmap function, has been mapped in test beam runs and its dependence on slope of the track, magnetic field and barometric pressure was measured, see [37] and section 3.3.1. Chapter 3 will elaborate more on the geometry of the P chamber cells while discussing the reconstruction algorithm.

### 2.2.3 The Z chambers

Z chambers consist of two layers of drift cells offset by one half cell with respect to each other, to solve the left-right ambiguities, see figure 2.5. So in total, if a muon passes through both MI and MO, its position in the (r,z) plane is measured eight times. Measured resolution [41] is found to be 700  $\mu\text{m}$ .

## 2.1 Introduction

The  $L_3$  detector is one of the four large detectors at the CERN electron-positron collider LEP. The experiment is designed to measure electrons, muons, photons and jets. Not attempting to identify hadrons,  $L_3$  has aimed at providing a better resolution for electrons, muons and photons. The experiment uses a time expansion chamber for charged tracks and vertex detection, a large scale electromagnetic shower detector and an accurate muon detector.

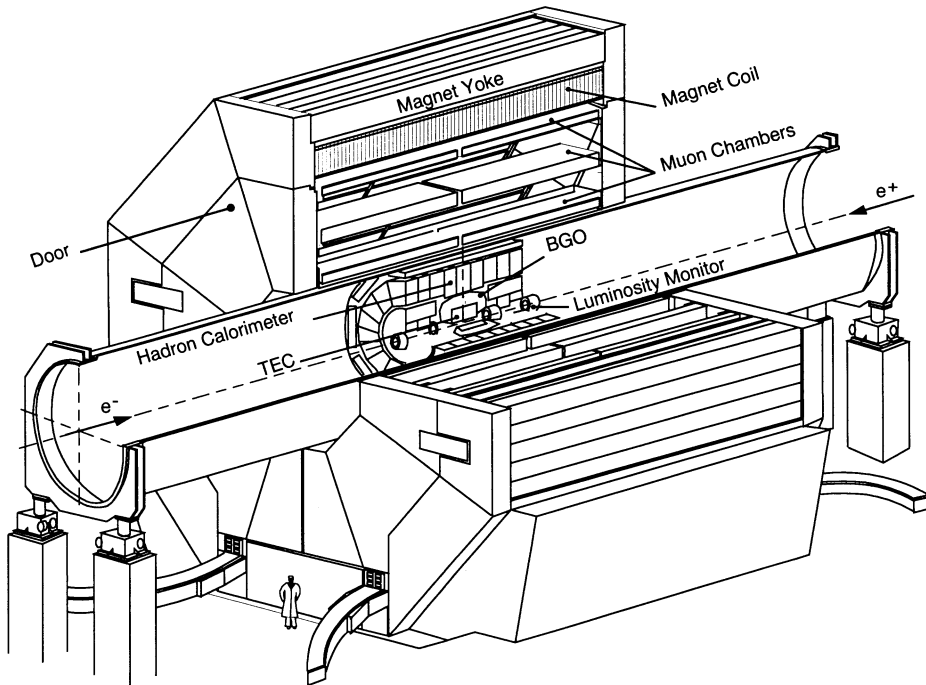


Figure 2.1: *Perspective view of the  $L_3$  detector. Starting from the beam pipe, the time expansion chamber (TEC), the electromagnetic calorimeter (BGO), the hadron calorimeter, the support tube, the muon chambers, the aluminium coil and the return yoke of the magnet are visible.*

All detectors are installed inside an octagonally shaped magnet. The magnet is a so-called warm magnet, giving a relatively low magnetic field of 0.5 T. A relatively low magnetic field is used because of the fact that the muon momentum,  $p$ , resolution improves linearly with the field,  $B$ , but quadratically with the effective length of the track,  $L$ , inside the field:

$$\frac{\Delta p}{p} = \frac{\Delta s}{s} = \frac{8}{0.2998} \frac{\Delta s}{BL^2 p} \quad (2.1)$$



in which  $s$  is the sagitta and  $\Delta s$  its error, see [35] and  $\Delta B$  and  $\Delta L$  are assumed to be negligible. In this equation  $p$  is in GeV,  $B$  is in T, and both  $L$  and  $s$  are in m. The sagitta,  $s$ , of a curve is defined as the maximum deviation of that curve from a straight line going through two fixed points on the curve (see figure 2.2):

$$s = y_2 - \frac{y_1 + y_3}{2} \quad (2.2)$$

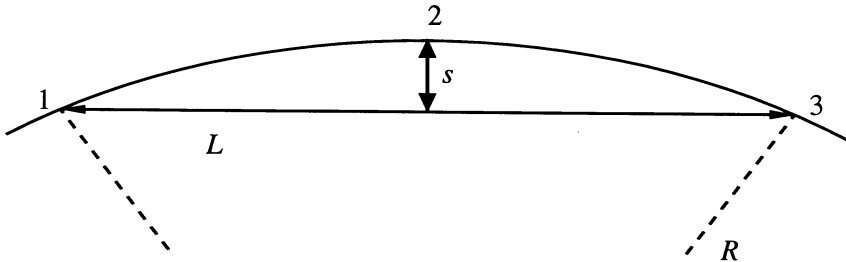


Figure 2.2: Definition of the sagitta,  $s$ , of a curved track.

To protect the detectors inside the magnet from the radiated heat an active thermal shield is placed on the inside of the coil. This keeps the volume occupied by the muon chambers at a constant temperature of  $21.0 \pm 1.5^\circ\text{C}$ . The poles of the magnet are double doors, which makes it possible to access the detectors (see figure 2.1). Going outwards from the beam pipe, the following detectors are installed.

- A central detector (Time Expansion Chamber, TEC), detecting charged particles (section 2.7).
- An electromagnetic calorimeter (BGO, named after its type of crystal material used:  $\text{Bi}_4\text{Ge}_3\text{O}_{12}$ ) to measure photon and electron energies (section 2.6).
- A scintillation counter array, used to measure the arrival time of traversing particles (section 2.5).
- A hadron calorimeter (HCAL), measuring hadron energies. This calorimeter also acts as a filter to provide a clean muon sample by absorbing the hadrons. In addition, the HCAL tracks muons as well (section 2.4).
- A muon detector (MUon CHambers, MUCH) consisting of 176 large drift chambers which are able to measure the sagitta of muon tracks (section 2.2).

The detectors (not including the magnet) are supported by a steel tube, 32 m long with a diameter of 4.45 m. Both ends of this tube rest on adjustable jacks, placed on concrete pillars. In this way all  $L_3$  detectors can be aligned relative to the LEP beam. The muon

chambers are supported by two torque tubes on rails, attached to the exterior of the support tube. Due to this construction, the muon chambers can 'easily' be pulled outside the magnet without interference with the other detectors. The detectors are complemented by a luminosity monitor, triggering and data taking electronics and a cluster of online and offline computers.

## 2.2 The muon detector

### 2.2.1 Design considerations

The  $L_3$  muon detector has been designed [36] to measure the momentum of high energy muons to an accuracy of 2.0%. For the 1990 data, a resolution of  $\Delta p/p = 2.5\%$  at  $p = 45$  GeV has been reached, thus providing a 1.8% dimuon mass resolution at 90 GeV. This is achieved by using a configuration of three layers of drift chambers which measure the curvature of a muon track in the region between the support tube and the magnetic coil, as is shown in figure 2.3.

The drift chambers are mounted on two Ferris wheels called Master and Slave, which are mirror images of one another. The Master Ferris wheel is located at positive  $z$ . A Ferris wheel has eight independent units, called octants, which are attached to the torque tube. Each octant is made out of five precision chambers. There are two chambers (MO) in the outer layer, two chambers (MM) in the middle and one inner chamber (MI) (figures 2.3A and B). These chambers measure the track coordinates in the bending plane.

In addition, the top and bottom covers of the MI and MO chambers are made of (less precise) drift chambers and they measure the  $z$  coordinate along the beam, as will be described in section 2.2.3.

In order to reach the afore mentioned resolution, a 45 GeV muon track sagitta  $s$ , must be measured with an accuracy  $\Delta s$  better than  $90 \mu\text{m}$ . This follows from equation 2.1 and the fact that  $s(45 \text{ GeV}) = 3.57 \text{ mm}$ . There are four components to  $\Delta s$ :

- one due to the intrinsic resolution of the chambers,  $\Delta s_{\text{ch}}$ ,
- one due to the multiple scattering,  $\Delta s_{\text{ms}}$ ,
- one due to the systematic error in the relative alignment of the three layers,  $\Delta s_{\text{al}}$ ,  
and
- one due to the systematic error in the electronics and electron drift path reconstruction,  $\Delta s_{\text{dp}}$ .

From measurements with a test chamber [37], a single wire resolution of about  $200 \mu\text{m}$  was found. Using the multiple-sampling technique described in [38], the maximum error on the measurement in MI and MO,  $\epsilon_1$  and  $\epsilon_3$  respectively, and MM,  $\epsilon_2$ , can be calculated:

$$\epsilon_1 = \epsilon_3 = \frac{200 \mu\text{m}}{\sqrt{(0.9 \times 16)}} = 53 \mu\text{m}, \quad (2.3)$$

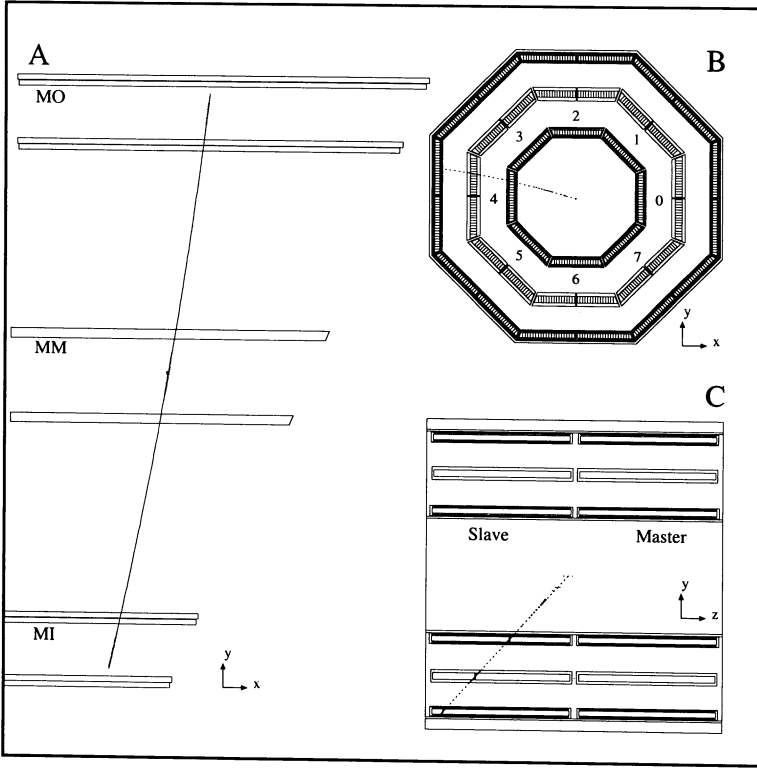


Figure 2.3: Three views of the muon chamber system, containing a muon track from a real hadronic event. Picture A shows the right half of octant 4: an MI chamber at the bottom (cut in two), an MM chamber in the middle and an MO chamber at the top. Picture B shows the  $xy$  view of the eight octants and picture C shows the  $yz$  view.

$$\epsilon_2 = \frac{200 \mu\text{m}}{\sqrt{(0.9 \times 24)}} = 43 \mu\text{m}, \quad (2.4)$$

where the factor 0.9 takes into account 10% inefficiencies and 16 (24) is the number of measurements in MI/MO (MM). This means that  $\Delta s_{\text{ch}}$  is about  $57 \mu\text{m}$ . The multiple scattering contribution,  $\Delta s_{\text{ms}}$ , is estimated to be about  $31 \mu\text{m}$  at 45 GeV[39]. Regarding the alignment of the chambers, muons coming from the origin and more energetic than 3 GeV are confined to one octant. Therefore alignment is only critical between chambers of the same octant. This is taken care of by complex optical and mechanical measurements (RASNIK, see [40]) as well as UV laser and cosmic ray verification. A systematic error of about  $30 \mu\text{m}$  was found [35]. Combining these three components with a  $\Delta s_{\text{dp}}$  of  $50 \mu\text{m}$ , the total error,  $\Delta s$ , stays below  $90 \mu\text{m}$ .

### 2.2.2 The precision chambers

The momentum measuring, or "P" chambers, each contain a few hundred signal wires, the so-called sense wires, and a total of about 3000 field shaping wires. These wires are about 5.6 m long and are supported by three bridges, one at each end, precisely positioning the wires and one in the middle to reduce the gravitational sag of the wires to  $96 \mu\text{m}$ . The drift times measured by the wires are converted into digits by (multi hit) TDC's, time to digit converters. The cell structure of the chambers contain 16, 24 and 16 sense wires for the MI, MM and MO chamber respectively, each cell being exactly 101.500 mm wide, see figure 2.4.

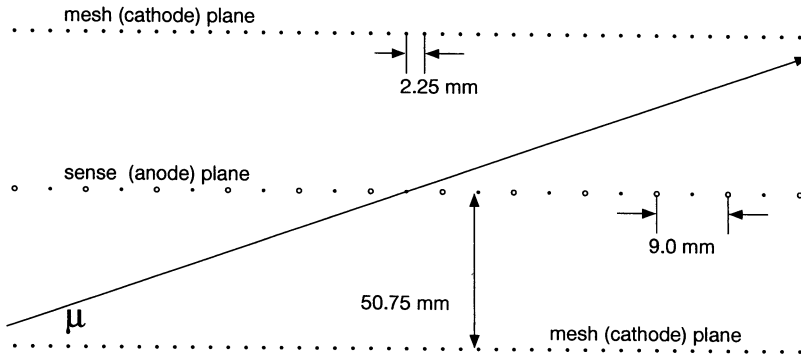


Figure 2.4: *Wire configuration of a precision chamber cell. The open circles in the middle plane stand for the sense wires, the closed circles for the field (shaping) wires. The closed circles in the upper and lower wire plane are the mesh wires.*

The chamber cell has been designed to have a uniform electric field throughout the active region. The sense wires are spaced 9 mm apart and interspaced with field wires. Three additional guard wires beyond the last sense wire equalise the drift time behaviour of the sense wire plane. A plane of cathode (mesh) wires spaced 2.25 mm apart, is at 50.75 mm from the sense wire plane.

The time-to-distance conversion function, called the cellmap function, has been mapped in test beam runs and its dependence on slope of the track, magnetic field and barometric pressure was measured, see [37] and section 3.3.1. Chapter 3 will elaborate more on the geometry of the P chamber cells while discussing the reconstruction algorithm.

### 2.2.3 The Z chambers

Z chambers consist of two layers of drift cells offset by one half cell with respect to each other, to solve the left-right ambiguities, see figure 2.5. So in total, if a muon passes through both MI and MO, its position in the  $(r, z)$  plane is measured eight times. Measured resolution [41] is found to be  $700 \mu\text{m}$ .

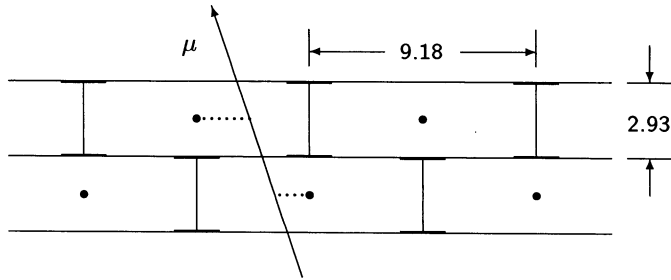


Figure 2.5: Schematic side view of the wire configuration of a Z layer (the units are in cm).

## 2.3 The muon filter

The muon filter is mounted on the inside wall of the support tube and adds 1.0 absorption length,  $\lambda_I$ , to the hadron calorimeter. It consists of eight identical octants, each made of six absorber plates, interleaved with five layers of proportional chambers and followed by five absorber plates matching the circular shape of the support tube, conform the left picture of figure 2.6. It covers a polar angle region of  $53^\circ \leq \theta \leq 127^\circ$ . The coordinates of the hits measured by the muon filter are only in the  $(r, \phi)$  plane.

## 2.4 The hadron calorimeter

The energy of hadrons coming from  $e^+e^-$  collisions is measured in  $L_3$  by the “total absorption” technique (calorimetry) with the BGO crystals and the uranium hadron calorimeter. The hadron calorimeter is made out of two parts: the barrel part, HBAR (section 2.4.1) and the forward-backward part, HCAP (section 2.4.2).

It is a fine-sampling calorimeter made out of depleted uranium absorber plates interspersed with proportional wire chambers. It acts as a filter as well as a calorimeter, allowing only non-showering particles to reach the precision muon chambers. Uranium has a short absorption length,  $\lambda_I$ , thus maximising the amount of absorber material in the available space. Because uranium is radioactive it acts as a built in gamma source for the calibration of the wire chambers. By orienting the wires in alternating planes in different directions, a better determination of hadron jet directions is possible.

### 2.4.1 The barrel hadron calorimeter

The hadron calorimeter barrel, shown schematically in figure 2.6, covers the central region ( $35^\circ \leq \theta \leq 145^\circ$ ). It has a modular structure consisting of 9 rings made out of 16 modules each. The innermost ring is centered at the interaction vertex and flanked on either side by one ring of long modules followed by three rings of short modules.

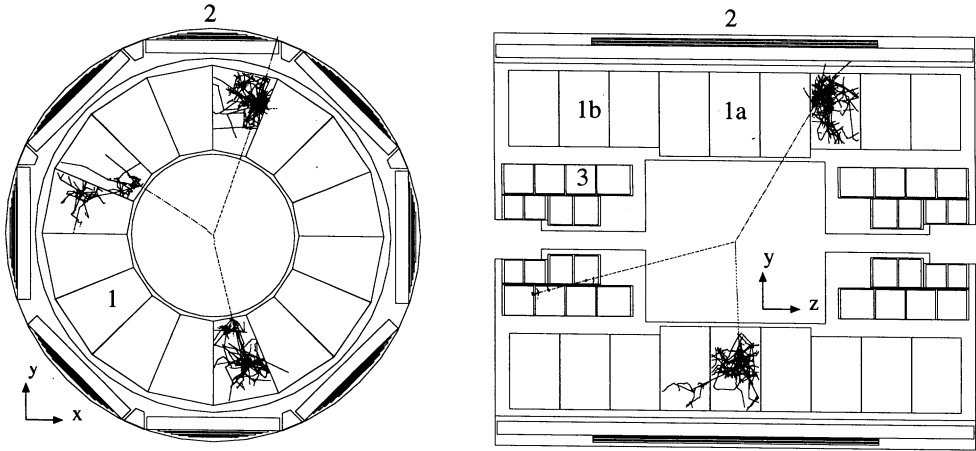


Figure 2.6: The left picture shows the  $xy$  view of the barrel hadron calorimeter (1) and the muon filter modules (2) surrounding it. The right picture shows the  $yz$  view with the endcaps of the hadron calorimeter (3). (1a) are the so-called long modules, (1b) the short ones. The tracks displayed are simulated tracks of charged pions and their shower products in the calorimeter. They are different for the left and right plot.

Over the barrel region, the amount of material traversed by a particle originating at the vertex varies between 5.9 and 7.2 nuclear absorption lengths. The response of prototypes and the finished modules to beams of hadrons and electrons with energies ranging from 1 to 50 GeV was measured. The resolution of the hadron and electromagnetic calorimeters combined,  $\sigma$ , defined as the standard deviation of a gaussian fit to the pulse height distribution, as a function of  $E$  was found to be:

$$\frac{\sigma}{E} = \left( \frac{55}{\sqrt{E}} + 5 \right) \% \quad (2.5)$$

where the energy  $E$  is in GeV.

Using two-jet events with both jets in the barrel part of the detector, a total energy resolution of 10.2% has been reached [42]. This value compares very well with the  $\sigma/E$  relation as found in the test beam. Figure 2.7 shows the total energy distribution for two-jet events (left) and the acollinearity angle between the jets (right) for data (solid dots) and for Monte Carlo (histogram) for the complete solid angle. The acollinearity angle between the jets is defined as 180 degrees minus the angle between the two jet directions. Assuming the same accuracy for each jet, an accuracy of 30 mrad on the determination of single jet angles is obtained for data and 28 mrad for Monte Carlo events.

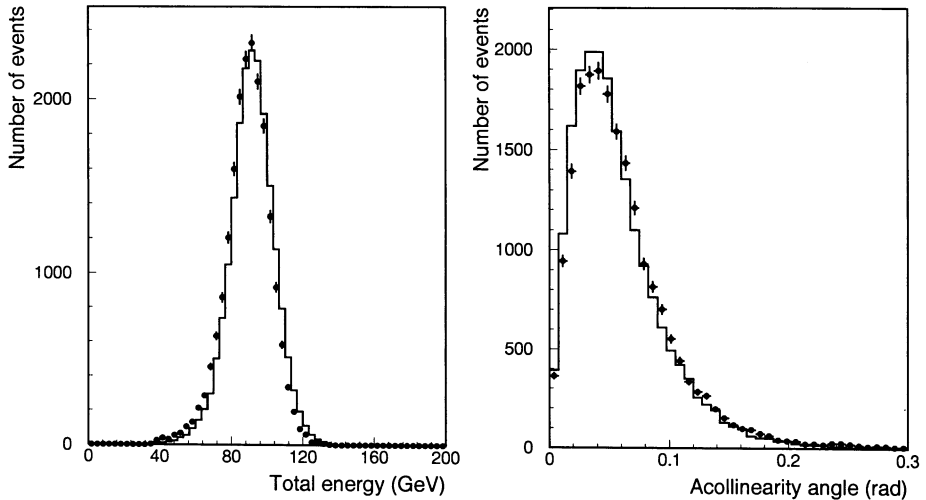


Figure 2.7: Left: The distribution of the total energy measured with the calorimeters for two-jet events for data (solid dots) and for Monte Carlo (histogram) for the complete solid angle. Right: The acollinearity angle between the two jets for data (solid dots) and for Monte Carlo (histogram) for the complete solid angle.

### 2.4.2 The forward-backward hadron calorimeter

The endcaps of the hadron calorimeter cover the polar angle region  $5.5^\circ \leq \theta \leq 35^\circ$  and  $145^\circ \leq \theta \leq 174.5^\circ$  over the full azimuthal range (see figure 2.6). The solid angle covered by the endcaps (18% of  $4\pi$ ) extends the coverage of the calorimeter to 99.5% of  $4\pi$ .

The HCAP is made out of removable half-rings to provide easy access to the inner detectors. Just like the barrel, HCAP is made out of separate modules, consisting of layers of uranium plates with proportional wire chambers in between. The wires of two overlapping chambers are rotated over  $22.5^\circ$  in  $\phi$  with respect to each other. In this way the coordinates of  $\phi$  orthogonal to  $\theta$  can be measured and gaps are arranged such that they do not coincide in successive layers.

## 2.5 The scintillation counters

The scintillation counters are situated between the hadron calorimeter and the electromagnetic calorimeter. The counters cover a polar angle region of  $34^\circ \leq \theta \leq 146^\circ$  and they cover therefore the acceptance of the middle muon chambers (MM). In the azimuthal angle  $\phi$ , 93% of the solid angle is covered.

The good time resolution ( $\approx 0.46$  ns) of the scintillation counters can be used to discriminate dimuon events from cosmic muons. A single cosmic muon which passes near

the interaction point resembles a muon pair produced in an  $e^+e^-$  interaction. The time-of-flight difference, however, between opposite scintillation counters is about 6 ns for a cosmic muon and zero for muon pairs, as can be seen in figure 2.8.

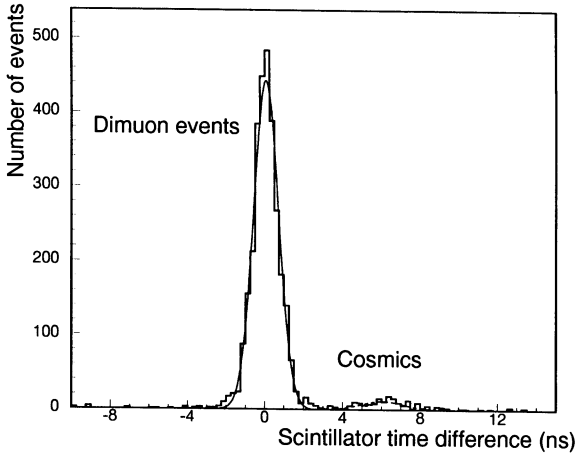


Figure 2.8: *The scintillation counter time difference distribution for dimuon events and cosmics. Through both peaks a Gaussian is fit.*

## 2.6 The electromagnetic calorimeter

The electromagnetic detector has a very good energy and spatial resolution for photons and electrons from 100 MeV to 45 GeV. It uses bismuth germanium oxide ( $\text{Bi}_4\text{Ge}_3\text{O}_{12}$ , or BGO) as both showering and detecting medium. BGO is a suitable material for an electromagnetic calorimeter because it has high stopping power (short radiation length,  $X_0 = 1.12$  cm), low afterglow and it is not hygroscopic.

The electromagnetic calorimeter consists of approximately 11,000 BGO crystals pointing to the interaction region (see figure 2.9). Each crystal is 24 cm long resulting in a total radiation length of  $21X_0$ . It is a truncated pyramid of about  $2 \times 2$  cm<sup>2</sup> at the inner end and  $3 \times 3$  cm<sup>2</sup> at the outer end. For electrons and photons, the energy resolution is about 6% at 100 MeV and about 1% for energies above 2 GeV and the measured spatial resolution above 2 GeV is better than 1 mm [43]. The detector surrounds the vertex chamber and is made of two half barrels (EBAR). Two endcaps (ECAP) complete the electromagnetic calorimeter.

The barrel contains 7680 crystals, giving a polar angle coverage of  $42^\circ \leq \theta \leq 138^\circ$  (figure 2.9).

The two endcaps are made out of 1536 BGO crystals each, covering the angular region of  $10^\circ \leq \theta \leq 35^\circ$ . Both endcaps have a hole of three by three crystals to allow for the RFQ, a device to calibrate the crystals in situ (figure 2.9). Installation took place between



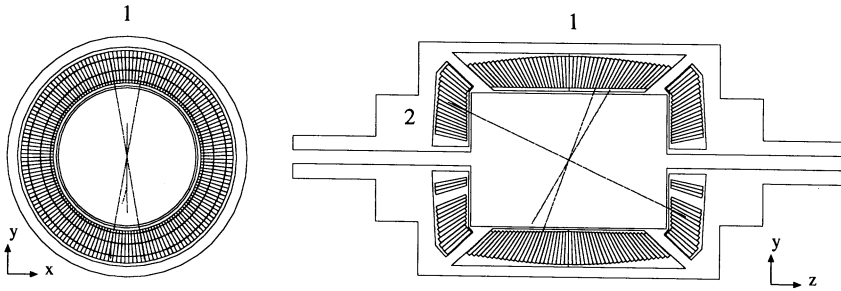


Figure 2.9: The left picture shows the  $xy$  view of the barrel electromagnetic calorimeter (1). The right plot shows the  $yz$  view in which the barrel (1) as well as the encaps (2) can be seen.

the 1990 and 1991 running periods of LEP. Because of extensive shielding and cabling of the TEC, the endcaps do not closely fit to the barrel.

Before the installation of the BGO endcaps in 1991, another electromagnetic calorimeter was installed to enable low energy single photon analysis [44]. These so-called veto counters, large blocks of electromagnetic absorber (lead plates interspaced with sheets of scintillator material), added 15 radiation lengths. When the BGO endcaps were installed the veto counters were removed.

## 2.7 The central track detector

The  $L_3$  central track detector is designed for the detection of charged particles. It is a so-called time-expansion-chamber, TEC, and is made out of two concentric cylindrical drift chambers surrounded by two cylindrical proportional chambers with cathode strip read-out, the Z detector.

The two inner cylinders consist out of 12 and 24 sectors respectively (see figure 2.10). Their sensitive length is 982 mm. There are three types of sense wires: standard wires (SW) to measure the  $r\phi$  coordinate, charge division (CD) wires to measure the  $z$  coordinate and groups of five grid wires on each side of the amplification region which determine the left-right ambiguity by measuring the induced signals (LR wires).

The inner sectors include 8 SW, 2 CD wires while the outer sectors include 54 SW, 14 LR wires and 9 CD wires.

During the operation of 1990, the CD and LR wires did not perform as designed and the Z detector was switched off part of the time because it caused too much noise. This made it almost impossible to measure the  $z$  coordinates of the hits found by the TEC. Furthermore, due to a broken wire in outer sector 12 of the TEC, this sector was also switched off during the 1990 run. During the shutdown between the 1990 and 1991 data taking, the noise problems were solved and the broken wire was taken out.

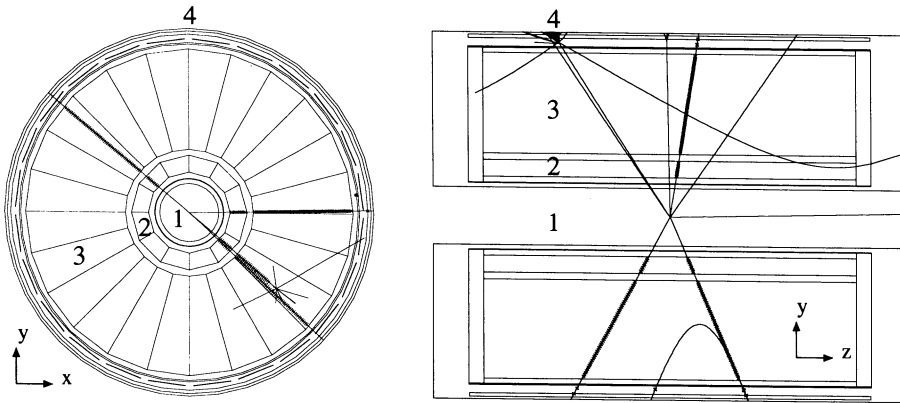


Figure 2.10: The left picture shows the  $xy$  view of the TEC. The right plot shows the  $yz$  view. (1) is the beam pipe, (2) an inner sector, (3) an outer sector and (4) belongs to a Z layer. The tracks drawn in both views are simulated tracks of charged particles and are different for both plots.

## 2.8 The luminosity monitor

The  $L_3$  luminosity monitor is designed for luminosity measurements at LEP by measuring the rate of small angle Bhabha events,  $N_{\text{Bhabha}}$ . Because the cross section,  $\sigma_{\text{Bhabha}}$ , for the Bhabha process ( $e^+e^- \rightarrow e^+e^-$ ) is well known, the integrated luminosity,  $\mathcal{L}_{\text{int}}$ , of the running period can be calculated:

$$\mathcal{L}_{\text{int}} = N_{\text{Bhabha}}/\sigma_{\text{Bhabha}} \quad (2.6)$$

The monitor is located at about 2.7 m from the interaction point in the angular region  $30 \text{ mrad} \leq \theta \leq 65 \text{ mrad}$ , where the contribution of diagrams describing the  $Z^0$  exchange is very small [15]. The monitor, as is shown in figure 2.11, consists of a cylindrical BGO array arranged in 8 rings.

To ensure optimum shower containment, the acceptance is limited to crystals that are not at the edge of the half rings (see figure 2.11). Thus the luminosity monitor will accept a polar angular region of 30.92 - 64.41 mrad for 1990 and 29.56 - 61.66 mrad for 1991 and an azimuthal angular region of  $|\phi - 90^\circ| > 11.25^\circ$  and  $|\phi - 270^\circ| > 11.25^\circ$  with full efficiency, corresponding to an effective Bhabha cross-section of about 88.5 nb for 1990 and 90.7 nb for 1991. At an average luminosity of  $10^{31} \text{ cm}^{-2}\text{s}^{-1}$  a trigger rate of about 1 Hz will result, to be compared to the 0.3 Hz expected rate from  $Z^0$  events. Thus, after a 3 hour run the statistical error will be around 1%. The  $L_3$  1990 and 1991 luminosity measurements reach a 0.6% systematic precision [45]. In table 2.1 the various contributions to the systematic errors are shown.

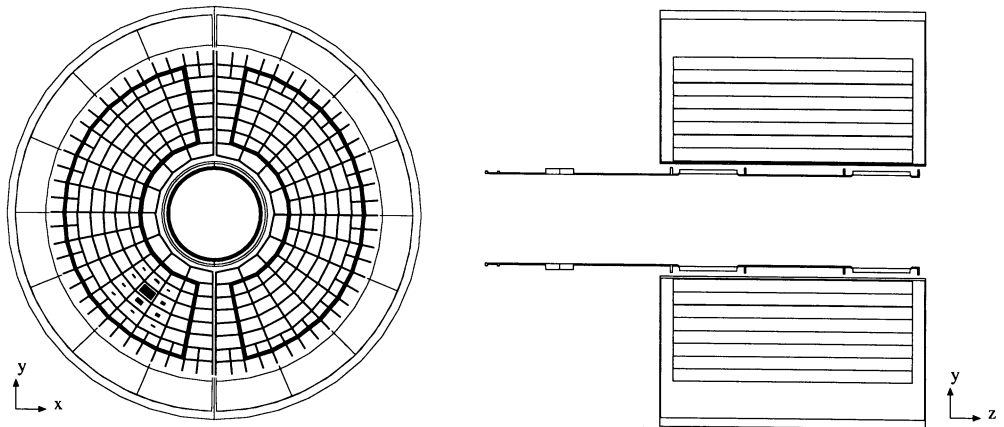


Figure 2.11: Endview (left) and the side view (right) of the luminosity monitor showing the half rings of 8 rings of BGO crystals. The fiducial volume is shown by the line drawn in bold.

## 2.9 The $L_3$ trigger

After each beam crossing, the  $L_3$  trigger decides if an  $e^+e^-$  interaction took place and if so it decides whether the event should be recorded. This function is performed at three levels reducing the 45 kHz beam crossing rate to a few Hz of tape writing rate. At the same time the quality of the accepted data and the detector parameters (for detector calibration) are monitored. The trigger control box implements the final level-1 trigger decision and distributes it to all subdetectors and higher level triggers. It synchronises the whole data acquisition system.

Contribution	1990 and 1991 (%)
Luminosity trigger uncertainty	< 0.1
Geometry of luminosity monitor	0.4
Bhabha event selection criteria	0.3
Background subtraction	< 0.1
Monte Carlo statistics	0.1
Theoretical systematic uncertainty	0.3
<b>Total systematic error</b>	<b>0.6</b>

Table 2.1: The various contributions to the systematic error on the 1990 and 1991 luminosity measurement.

### 2.9.1 The level-1 trigger

The level-1 trigger is operated at 45 kHz, i.e. within 22  $\mu$ s it decides whether or not to start digitising and storing the detector data or clearing the electronics. A negative decision at level-1 does not contribute to the dead time. The level-1 trigger is a logical OR of 4 trigger conditions:

- calorimetric (energy) trigger
- muon trigger in logical AND with the scintillator trigger
- TEC trigger
- scintillator trigger

These four triggers are described below. The trigger rates quoted are from the 1990 running period of LEP.

#### Calorimetric trigger

The calorimetric trigger itself consists of 6 subtriggers again all in a logical OR state and reaches a final decision in 21  $\mu$ s. It processes the information from the ECAL, HCAL and luminosity monitor (256, 384 and 32 channels respectively). These subtriggers together describe the calorimetric trigger:

- Total energy trigger ( $\sim 0.2$  Hz): if the total energy detected in the calorimeters is larger than a certain threshold this trigger is satisfied. This cut is divided into four cuts in logical OR:
  - The energy in HBAR and EBAR should be more than 15 GeV,
  - The energy in all (including the endcaps) the calorimeters should be more than 20 GeV,
  - The energy in EBAR only is larger than 10 GeV,
  - The energy in the (including the veto counters or endcaps) electromagnetic calorimeter is larger than 20 GeV.
- Cluster trigger ( $\sim 1.2$  Hz): the number of clusters found, where the minimal cluster energy is 1 GeV, should be bigger than 7.
- Single photon trigger ( $\sim 2.1$  Hz): the energy in the BGO is larger than 1.0 GeV and the area of the hit should be small and contain at least 80% of all the energy deposited in the BGO.
- Hit counting trigger ( $\sim 0.2$  Hz): The energy of one or more of the calorimetric trigger channels is above a certain value.
- Luminosity trigger ( $\sim 0.6$  Hz): more than 15 GeV in both monitors or more than 25 GeV in one and more than 5 GeV in the other. (Only every other event is written to tape).

- Single tag trigger ( $\sim 0.2$  Hz): more than 30 GeV in one luminosity monitor. (Only every 20th event is written to tape).

The total rate of this trigger is about 3.0 Hz.

### Muon trigger

The muon trigger uses the information from MUCH and looks for tracks pointing to the interaction region. It accepts events with a transverse momentum larger than 1 GeV. The muon trigger consists of three subtriggers:

- Single muon trigger ( $\sim 2.2$  Hz): two out of three P chambers are hit and three out of four Z chambers in the same octant covering the angular range of:  $44^\circ \leq \theta \leq 136^\circ$
- Dimuon trigger ( $\sim 6.0$  Hz): two out of three P chambers are hit and one of the MI Z chambers in the same octant together with two out of three P chambers hit in one of the five opposite chambers, covering the angular range of:  $36^\circ \leq \theta \leq 144^\circ$
- Small angle dimuon trigger ( $\sim 4.2$  Hz): one P chamber hit in MI and one Z chamber hit in MI in the same octant together with the same conditions in one of the three opposite octants, covering the angular range of:  $24^\circ \leq \theta \leq 44^\circ$  and  $136^\circ \leq \theta \leq 156^\circ$ . Furthermore, the tracks should be in opposite  $z$  direction.

The muon trigger rate is 9.5 Hz. However, after requiring at least one scintillator counter in time, this rate goes down to 1.5 Hz.

### TEC trigger

The TEC looks for two back to back tracks within a cone of  $20^\circ$ . The rate of this trigger is 1.2 Hz.

### Scintillator trigger

The scintillator trigger, based on the signals from 30 counters, requires a coincidence of five out of the 30 counters and serves as a simple backup for the energy trigger. This trigger rate is about 0.2 Hz.

If the event is rejected by the level-1 trigger the system is reset by the trigger control box and ready for the next event. This signal also stops the level three trigger, which started working in parallel. If, however, the event is accepted, the trigger control box starts the subdetector data conversions and buffering and the level-2 trigger is activated.

## 2.9.2 Higher level triggers

Based on all level-1 trigger data and decisions, the level-2 trigger makes a more complex coincidence. The level-3 trigger is embedded in the main flow of the data acquisition. Unlike

the level-1 and level-2 triggers, the level-3 trigger has access to the complete digitised data with finer granularity and higher resolution. Algorithms, comparable to the ones used in the offline reconstruction program, are applied to reject background events. In case of a positive level-2 and level-3 decision, the event is written on tape.

The level-4 trigger is an offline implementation of the level-3 trigger. It contains more refined algorithms and it served as a temporary substitute and testing ground for the 1990 level-3 trigger. During the 1991 running period most of the level-4 software was implemented in the level-3 trigger.

## 2.10 The $L_3$ software packages

Just like building the  $L_3$  detector, “building” the  $L_3$  software took several years and it is still subject to changes in order to bring it to perfection. In this section the  $L_3$  simulation and reconstruction packages, Sigel3 and Regel3 respectively, will be described shortly after which the data flow in  $L_3$  is illustrated. Before describing Sigel3, the structure of the  $L_3$  database system is discussed in the next paragraph.

### 2.10.1 The $L_3$ database system

Nowadays high energy physics experiments require the use of powerful database systems. The data consists usually of a part that is largely time independent, for instance the parameters which describe the geometry of the experimental setup, and another part whose content may vary with time and with different frequencies, like the temperature of a particular subdetector and the calibration corrections for a particular sensor. This data has therefore to be recorded repeatedly with a frequency depending on the data type. The time dependent data represents a large amount of information. The  $L_3$  database is split into six independent subdetectors and three global databases. The amount of information stored in these individual files is in the order of 10 MB per file. As an example, the database belonging to the muon detector contains among other things:

- alignment (RASNIK) information of the relative position of the chambers,
- $t_0$  values for every P and Z chamber wire,
- the information of malfunctioning wires,
- high voltage settings of the wires,
- the conditions of the drift gas, like pressure and temperature.

Since the  $L_3$  experiment is operating in a multi-user and multi-computer environment a centralised database is maintained by a database ‘server’, a program that controls all the different databases, streamlines the communication between them and avoids clashes between different processes, like writing at the same time to the same database file.

### 2.10.2 Sigel3: the $L_3$ detector response simulation package

Precisely simulating detector response to an interaction is very useful for a number of reasons. A good understanding of how the detector reacts to a specific simulated interaction will provide useful information for studying the data sample and hence systematic errors will be reduced, thus resulting in more precise analyses. The geometrical detector acceptance can be studied and precisely calculated as well as acceptances in specific phase space regions. The exclusion of specific phase space regions is obtained by the application of so-called cuts on event parameters. The way this procedure is used will be shown in the analysis chapters of this thesis. Furthermore, simulating detector response can be used to test the reconstruction package while developing it.

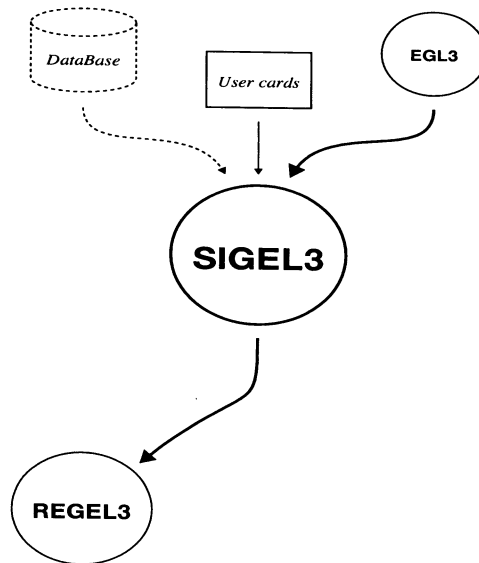


Figure 2.12: *The input and output of Sigel3, the  $L_3$  simulation software.*

Sigel3 has been designed to simulate the response of the  $L_3$  detector to events taking place at LEP with the best accuracy and the highest precision. To achieve these goals the following ingredients are necessary:

- The geometry of the apparatus is described in a realistic way.
- The particles are tracked from the interaction vertex through the detector, correctly simulating all physical processes, to the best of our knowledge, that may occur.
- The response of all subdetectors is simulated using all the knowledge one has about its behaviour.

To perform these tasks, Sigel3 has been built around the Geant3 [46] package which:

- provides powerful tools to describe the geometry of any experimental set-up,
- uses accurate tracking routines which take into account all dominant physical processes,
- provides the user with a modular framework and many utilities which may also be used in the reconstruction phase.

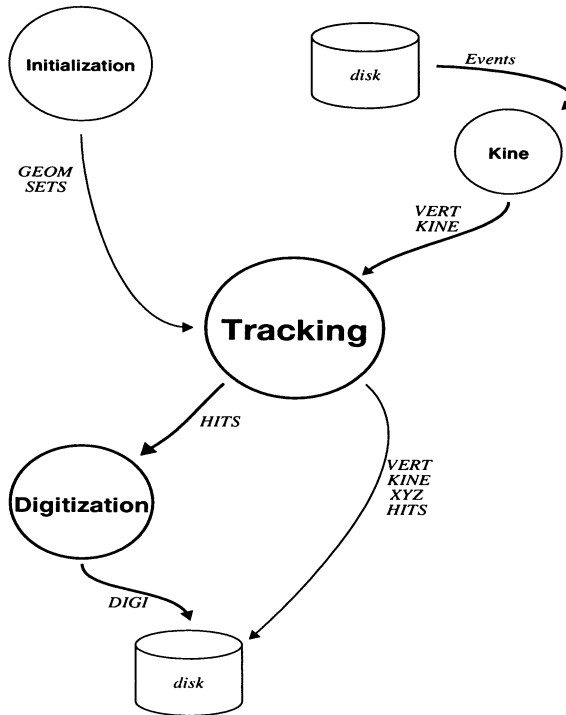


Figure 2.13: The internal structure of the  $L_3$  simulation package Sigel3.

As shown in figure 2.12, Sigel3 can take input from the database, describing any deviation between the  $L_3$  detector, as programmed with Geant, and the real detector (e.g. broken wires) and giving realistic detector noise. It needs input from the user by the use of so-called data cards, a set of specific commands e.g. where Sigel3 has to save its output on disk, and most importantly from Egl3, the  $L_3$  generator package. Egl3 is a special  $L_3$  interface ensuring that all the different  $e^+e^-$  generators (see box 2.1) give the same output format.

Figure 2.13 shows the internal structure of Sigel3. First the detector geometry is set up in the initialisation phase. Once this is done the Egl3 generator output is read from disk



### Box 2.1 Physics generators

By calculating all the Feynman diagrams up to the  $n$ th order of a specific process, an approximated cross-section can be computed. Using this cross-section and relevant branching ratios and decay rates, known from experiment, generators calculate the reaction kinematics of such a process. Since successively generated events ought to be independent of each other, during this generation so-called weighted pseudo random numbers are used. Hadronic (QCD) final states cannot (yet) be described by calculating diagrams alone, for the details of hadronisation and fragmentation are still unknown, and phenomenological models and hadron decays from lower centre of mass energy experiments have to be used.

Generators predicting kinematics for (non Standard Model) new particles are of course all speculative and must be used with great care. There are also a few generators calculating background processes to the  $Z^0$  physics, viz. cosmic muon simulation and the simulation of the two photon process. As a last remark it should be noted that the CPU time spent generating one event is generally much less than the time needed to simulate the  $L_3$  detector response of that event.

BABAMC	radiative bhabha scattering in the 2nd and 3rd order QED
KORALZ	$e^+e^- \rightarrow \tau^+\tau^-(\gamma)$ or $\rightarrow \mu^+\mu^-(\gamma)$ or $\rightarrow \nu\bar{\nu}$
JETSET7.3	$e^+e^- \rightarrow Z^0/\gamma \rightarrow q\bar{q}(\gamma)$

which contains the kinematics from the particles produced in the  $e^+e^-$  interaction and the vertices belonging to the produced particles.

The particles are tracked through the detector by Geant where the interactions with the detector and the possible particle decays are simulated. If a particle passes through a sensitive volume of the detector, information quanta like position and energy are stored. These information quanta are called hits. With these hits the response signals of the detector are calculated such that they are as close as possible to the ones generated by the real detector, including resolution effects and digitisation. Section 3.2 explains this procedure for the special case of the muon subdetector.

Once all particles have decayed, are stopped in the detector or have left the detector, the digits, combined with the information of the corresponding sensor (a wire, a photodiode or a scintillator), are stored on disk together with the generator information, the particle trajectories in the detector and the hits as calculated by Geant. The output thus obtained is ready for reconstruction and analysis.

### 2.10.3 Regel3: the $L_3$ reconstruction package

The package Regel3 is a program that uses the digitised output of the detector or the output from Sigel3, the package described in the previous paragraph, as input.

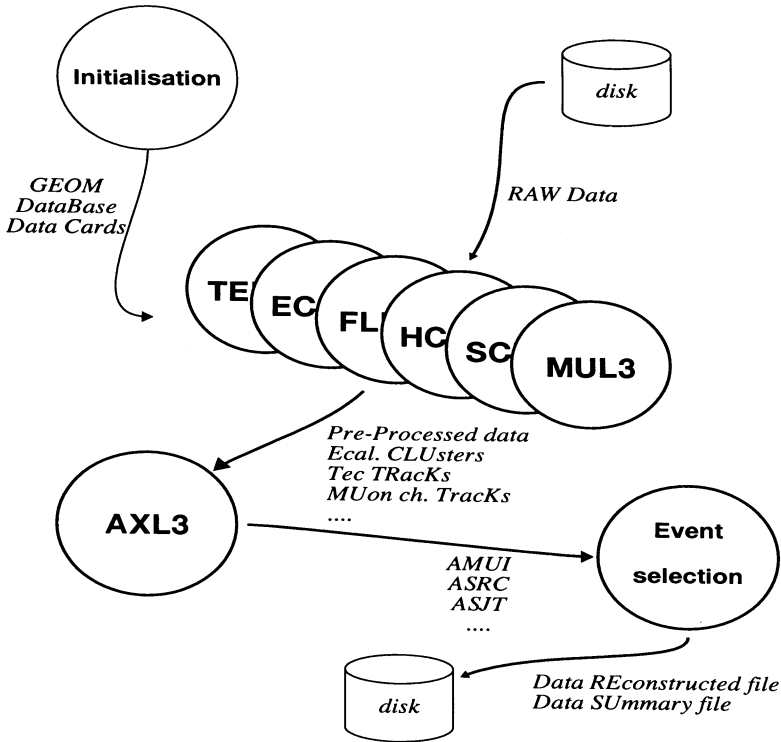


Figure 2.14: Flow diagram of the  $L_3$  reconstruction program, Regel3.

Shown in figure 2.14 is the structure of Regel3. The input is read from disk and the subdetector reconstruction units (TEL3, ECL3, ...) start to analyse the digits as read by the respective subdetector components. At this stage the subdetector packages do not use information from one another. Their outputs are separate objects, like TEC tracks, muon chamber tracks and the energy contained in a cluster of BGO crystals.

The combination of these reconstructed objects across the  $L_3$  detector is done by the package AXL3, a program that reads all the output of the lower level subdetector packages. AXL3 then creates the final reconstructed objects that aim to represent as close as possible particles and groups of particles: "muons", "electrons", "photons", "jets" and "clusters of particles". However, AXL3 makes no physics assumptions and it does not perform any physics analysis; this is left to analysis groups as described in the next section.

AXL3 is partitioned into several distinct modules which produce the following objects:

- AMUI: muons reconstructed across the  $L_3$  detector giving the best estimate of their energy and direction at the vertex, see section 3.4.
- Asrc: smallest resolvable clusters made out of TEC tracks and calorimeter hits. The algorithm is optimised towards forming combinations of TEC tracks and clusters of BGO crystals, that could be electrons or photons.
- Asjt: jets using the Asrc's as fundamental building blocks, giving well separated objects. A geometrical algorithm is used to combine the Asrc's into jets [42]. An angular resolution of 30 mrad is reached. These jets are used to determine the initial quark direction in the forthcoming analyses chapters.

#### 2.10.4 Data flow and selection in $L_3$

Data from the  $L_3$  experiment is analysed by first filtering and reconstructing events in a series of production steps. The output of this production is a group of datasets which are ready for detailed physics analysis. Figure 2.15 shows the outline of the  $L_3$  analysis strategy.

During PASS 1 the raw data is checked for internal consistency (Validate), first order calibrations are applied (DBL3), obvious background is filtered out (Level 4) and the remaining events are fully reconstructed by REGEL3. The program splits the reconstructed candidate events into several output streams called "Physics Datasets", one for each major event candidate classification (e.g. multihadron events used for the analyses described in this thesis). The event will always be written to the Master Data Reconstruction (MDRE) file. PASS 1 takes place in 'pseudo-real-time', that is within a few hours of data taking, using 'first round' calibrations.

After several PASS 1 jobs have been run, the output physics datasets corresponding to each event candidate category are collected onto tapes. This results in a concentrated sample of events for each of several analysis topics. The events are also written in a so-called data summary format (DSU), a compressed version of the MDRE format, which can easily be handled by the analysis groups. The physics analysis may include reconstructing selected samples of events with improved calibrations and software.

The PASS 2 reconstruction is run after a full recalibration of the detector has been completed. The number of events processed by PASS 2 is about one tenth of those processed in PASS 1, if luminosity events are excluded.

## 2.11 LEP

The energy of the LEP electron and positron beams in 1990 and 1991 ranged from 88.2 GeV up to 94.2 GeV divided into two times seven scan points around the mass of the  $Z^0$ . The absolute error for 1990 on the centre of mass energy was found to be 20 MeV, obtained from a calibration of the accelerator with protons [47]. For the 1991 runs this error was reduced to 5.3 MeV using the resonant depolarisation technique [48]. The luminosity of the LEP machine in 1990 was typically 0.4 to 0.6  $10^{31} \text{ cm}^{-2}\text{s}^{-1}$  and in 1991 it was

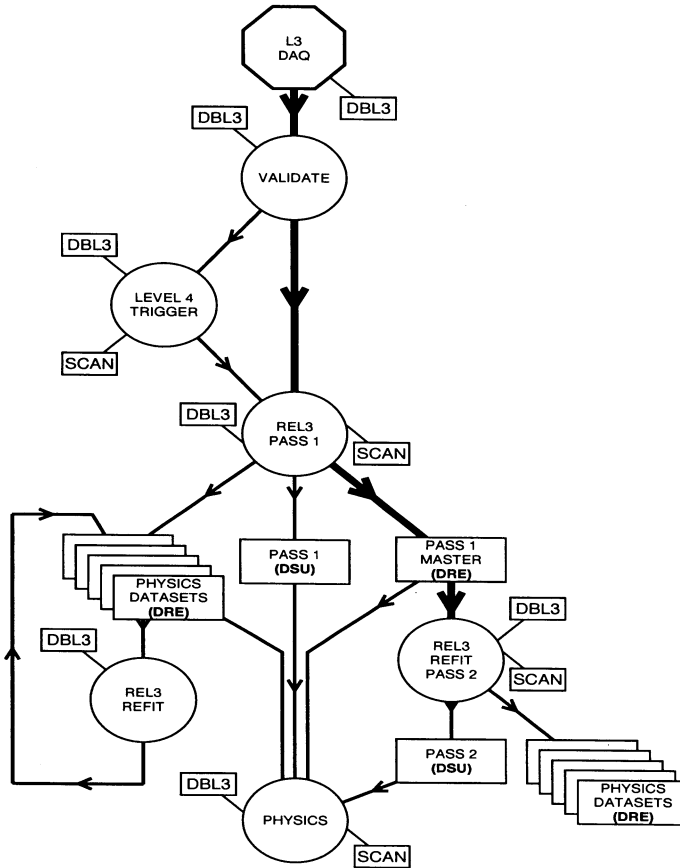


Figure 2.15: *The  $L_3$  data analysis strategy.*

approximately a factor 1.5 higher. This has yielded a total hadronic data sample of 428,006 events, corresponding to  $17.6 \text{ pb}^{-1}$ .

## Box 2.2 The subdetector parameters

### MUCH:

Angular acceptance:  $44^\circ \leq \theta \leq 136^\circ$  for three layers

Angular acceptance:  $36^\circ \leq \theta \leq 144^\circ$  for two layers

$\Delta p/p = 2.5\%$  for  $p = 45$  GeV and three layers

$\Delta p/p = 20.0\%$  for  $p = 45$  GeV and two layers

Average radial distance: MI: 2.53 m

MM: 4.01 m

MO: 5.43 m

### HCAL:

Angular acceptance:  $35^\circ \leq \theta \leq 145^\circ$  for the barrel

Angular acceptance:  $5.5^\circ \leq \theta \leq 174.5^\circ$  with endcaps

Absorption length:  $\lambda_I = 5.9 - 7.2$

### SCIN:

Angular acceptance:  $34^\circ \leq \theta \leq 146^\circ$

Angular acceptance: 93 % of the solid  $\phi$  angle

Time resolution: 0.46 ns

### ECAL:

Angular acceptance:  $42^\circ \leq \theta \leq 138^\circ$  for the barrel

Angular acceptance:  $10^\circ \leq \theta \leq 35^\circ$  for the endcaps

Energy resolution:  $\approx 6\%$  at 100 MeV

$\approx 1.5\%$  for energies above 2 GeV

Spatial resolution: better than 1 mm above 2 GeV

Radiation length:  $21X_0$

### Combining HCAL and ECAL (two-jet events):

Energy resolution:  $\sigma/E = (55/\sqrt{E} + 5)\%$

Energy resolution: 10.2% at 91 GeV

Spatial resolution: 1.7° (30 mrad)

**Box 2.2 (continued):****TEC:**

$r\phi$ resolution (SW):	58 $\mu\text{m}$
$z$ coordinate resolution (CD) :	63 mm
Two track resolution:	640 $\mu\text{m}$

**LUMI:**

Angular acceptance:	$30.92 \text{ mrad} \leq \theta \leq 64.41 \text{ mrad}$
Angular acceptance:	$ \phi - 90^\circ  > 11.25^\circ$ and $ \phi - 270^\circ  > 11.25^\circ$
Total error on luminosity:	0.6% (1990) 0.6% (1991)

**TRIGGER (1991):**

Beam crossing rate:	45 kHz
Level-1 trigger rate:	$\leq 8.0 \text{ Hz}$
Level-2 trigger rate:	$\leq 6 \text{ Hz}$
Level-3 trigger rate:	2 – 3 Hz

# Chapter 3

## The $L_3$ muon reconstruction

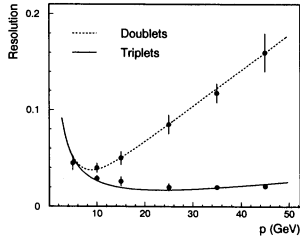


Figure 3.22: Momentum dependence of resolution for triplets and doublets in the Monte Carlo before smearing.

$$\begin{aligned}
 & + N_{22M} 2(1 - \eta)^2 \epsilon_2 (1 - \epsilon_2) \\
 & + N_{31M} 3\eta(1 - \eta)^2 (1 - \epsilon_1) \\
 & + N_{32M} 6\eta(1 - \eta)^2 \epsilon_2 (1 - \epsilon_2) \\
 N_{22MP} &= N_{22M} (1 - \eta)^2 (1 - \epsilon_2)^2 \\
 & + N_{32M} 3\eta(1 - \eta)^2 (1 - \epsilon_2)^2 \\
 N_{30MP} &= N_{30M} (1 - \eta)^3 \\
 & + N_{31M} (1 - \eta)^3 \epsilon_1 \\
 & + N_{32M} (1 - \eta)^3 \epsilon_2^2 \\
 N_{31MP} &= N_{31M} (1 - \eta)^3 (1 - \epsilon_1) \\
 & + N_{32M} 2(1 - \eta)^2 \epsilon_2 (1 - \epsilon_2) \\
 N_{32MP} &= N_{32M} (1 - \eta)^3 (1 - \epsilon_2)^2
 \end{aligned} \tag{3.32}$$

The six fractions from the data are compared with the six fractions from the adjusted Monte Carlo ( $M/P$ ) and a  $\chi^2$  fit to yield  $\eta$ ,  $\epsilon_1$  and  $\epsilon_2$  is performed. The inefficiencies are calculated using the following equations:

$$\begin{aligned}
 \mu_{\text{ineff}} &= N_{21M} (1 - (1 - \eta)^2) \\
 & + N_{22M} (1 - (1 - \eta)^2) \\
 & + N_{31M} (1 - (1 - \eta)^3 - 3\eta(1 - \eta)^2) \\
 & + N_{32M} (1 - (1 - \eta)^3 - 3\eta(1 - \eta)^2)
 \end{aligned}$$

### 3.1 Introduction

As described in the previous chapter, section 2.2, the  $L_3$  muon detector consists of three layers of drift chambers that measure position in the bending plane, and two layers that measure positions in the non-bending plane. Since this configuration differs fundamentally from other (LEP) detectors like ALEPH, OPAL and DELPHI [49, 50, 51], the algorithm for reconstructing muon tracks is different as well. Where  $L_3$  has the muon chambers inside its magnet, causing the muons to bend in the muon detector, the other LEP experiments have their muon chambers outside their magnet.

Muon tracks in the  $L_3$  experiment are reconstructed in two detectors: the vertex detector (see 2.7) and the muon detector. The muon detector samples the track in a 0.5 T magnetic field over a distance of approximately 3 m ( $BL^2 \approx 4.5 \text{ Tm}^2$ ). Taking an average energy loss into account, the track is then back-tracked through the calorimeters to the vertex region where the muon chamber track is matched with the corresponding TEC track yielding an improved angular resolution at the vertex. Tracks that do not enter the TEC region are considered to be cosmic muons or punch through coming from hadronic showers in the hadron calorimeter.

The other three LEP experiments sample a muon track in their inner tracking detector(s) in a larger magnetic field (1.5 T for Aleph) but over a shorter distance ( $\approx 1.5 \text{ m}$  for Aleph giving  $BL^2 \approx 3.4 \text{ Tm}^2$ ). Since their muon detectors are situated outside the magnet, these detectors are only used to tag the corresponding inner detector track as belonging to a muon. In a high multiplicity event it will of course be difficult to combine the proper inner detector track with the hits found a few meters away in the muon detector. Also the power to reject tracks as being punch through in a high multiplicity event is reduced this way.

In this chapter the simulation and reconstruction of muons in the  $L_3$  detector are discussed. Emphasis is put on the algorithms used to project the measured drift time onto a point in space on the muon trajectory.

### 3.2 Simulation of muon tracks in the $L_3$ detector

The simulation of the muon chamber response to charged particles is based on the accurate simulation of the trajectory of this charged particle by Geant, on the accurate description of the position of the wires in three dimensions and on the precise knowledge of the real muon chamber's response to charged particles.

The simulation of the response of the muon chambers to charged particles starts with the hits that Geant produces in these volumes. The simulation of the drift times including time of flight from the vertex to the muon chamber area of interest, time of signal propagation along the wires and noise and resolution effects are steered by a routine which starts the digitisation routines for the P chambers and the Z chambers respectively. In the rest of this section only the part relevant to the P chambers will be described.

The digitisation algorithm starts by looping over all hits in the P chambers. This is done in pairs, resulting in a string of pairs per layer, see figure 3.1. The drift time depends on the pressure and temperature of the gas and on the magnetic field. Therefore, if the two hits are in the same chamber, the pressure, the temperature and the magnetic field are calculated



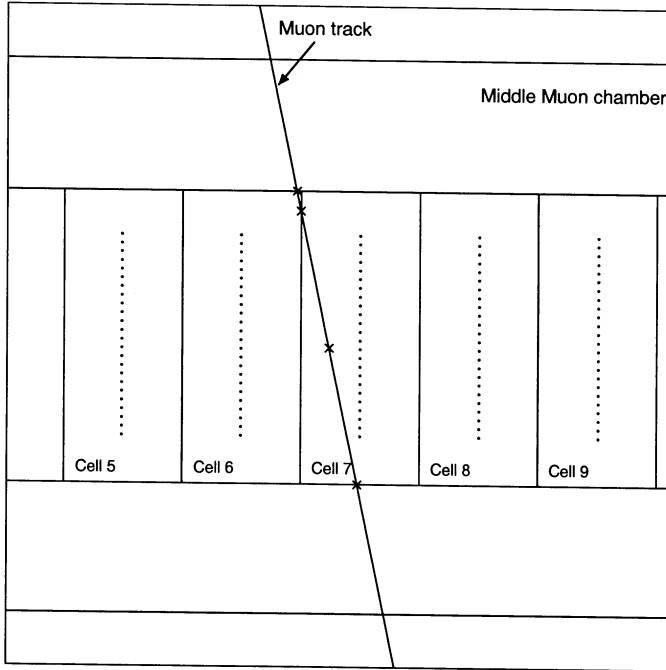


Figure 3.1: Hits (depicted as crosses) recorded during a GEANT simulation of a muon passing through two cells of a MM chamber.

midway between these two hits. This approximation is valid since the temperature and the magnetic field gradient are small inside the muon detector. Sigel3 uses the magnetic field map  $B(x, y, z)$ , which has been computed by applying a fit to the data of magnetic field sensors, mounted on the muon chamber system, see [52]. The temperature is assumed to be constant all over the  $L_3$  muon detector.

All wires in a chamber that should give a signal are identified and the corresponding drift times are calculated for each of them. The intercept of the particle trajectory (see box 3.1) and the so-called “standard drift path” (see paragraph 3.3.1) of these wires is calculated. With this information the drift time is calculated, using the “drift time drift distance” relationship which will be described in paragraph 3.3.1.

To be able to do this accurately, the exact position of the sense wires must be known. Due to gravity the wire positions are described by a chain curve and the deviation from a straight line is described by:

$$\Delta_g = 4A \frac{z}{\lambda} \left( \frac{z}{\lambda} - 1 \right)$$

in which  $A$  is the maximum deviation,  $96 \mu\text{m}$ ,  $z$  the coordinate along the wire and  $\lambda$  the total length of the wire, see figure 3.2.

Once the actual position in space and the drift time are known, the time of flight and the

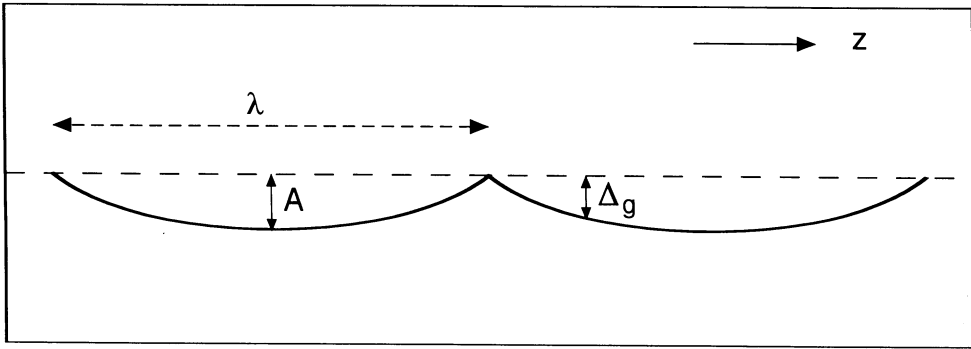


Figure 3.2: Schematic drawing of the shape of the sense wires in the muon detector.

time of propagation can be computed and they are added to the drift time. The resulting signal time is smeared by an approximated gaussian chamber resolution. The time obtained is digitised, taking the TDC resolution into account. It should be noted that only a distance dependent resolution is taken (see figure 3.3) whereas it is well known that the resolution also changes as a function of the slope of the track, see [37]. This deficiency of the Monte Carlo will be corrected for as explained in section 3.5.

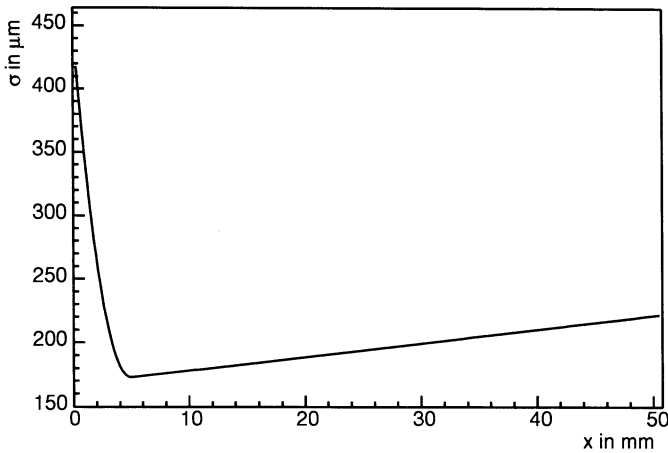


Figure 3.3: The single wire resolution function used by Sigel3.  $x$  is the distance from the sense wire.

### 3.3 The $L_3$ muon reconstruction

Tracks in the muon chambers are reconstructed in several steps. During the first step the reconstruction is limited to the individual P and Z chambers. Two dimensional pattern recognition is performed yielding candidate track segments: P segments in  $xy$  and Z segments in  $yz$ . For this purpose a drift time drift distance relationship is exploited. In the next step, these segments are associated with one another to form three dimensional track candidates.

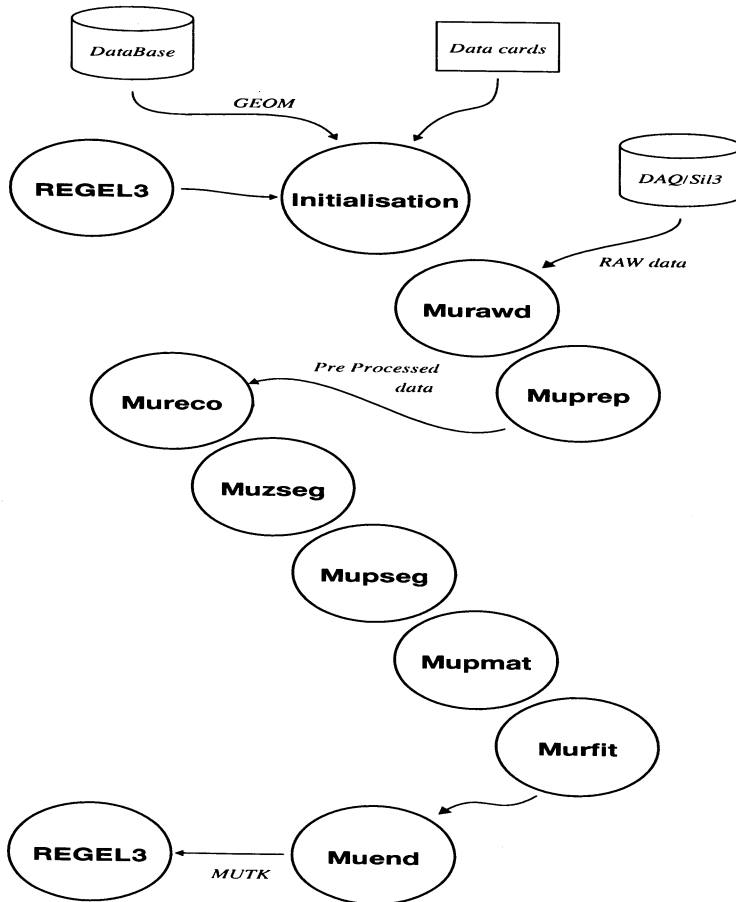


Figure 3.4: Flow diagram of the  $L_3$  muon reconstruction programme, Mu3.

Figure 3.4 shows the flow diagram for the  $L_3$  muon reconstruction package. Following the flow chart, the raw data is prepared before starting the pattern recognition (Murawd and Muprep). After it has been checked that the necessary database information is read, the

actual pattern recognition is started (Mureco). The data from the Z chambers is analyzed first and once the Z segments are found, the algorithm for the analysis of the P chambers is started. Mupseg, together with its subroutines, will be discussed in detail in section 3.3.2. Once the P segments are found, Z segments are matched into Z tracks: a combination of a MI and a MO Z segment.

The P segments and Z tracks are matched together to form muon tracks. At this stage the matching is limited to one octant only. Later on the inter octant matching is tried. The matching is based on a  $\chi^2$  test and the  $\chi^2$  of any combination should be below a certain threshold for the match to be accepted.

Once the three dimensional position of a segment is known, time of flight, and time of propagation corrections as well as alignment corrections are applied to the individual hits. The resulting parameters of the muon track, like position in space, momentum, curvature and sagitta, are recalculated and stored in a data bank called MUTK.

There are three types of muon tracks:

- Triplets: the P segments from MI, MM and MO are combined into one track.
- Doublets: only two of the three possible P segments are matched to form one track.
- Singlets: Only one P segment was found and it could not be matched with any other P segment in this octant.

This thesis will only describe the pattern recognition of P segments. For the equivalent Z segment description I refer the reader to [41].

### 3.3.1 The $L_3$ drift time drift distance relationship

Probably the most critical routine in Mul3 is the routine that derives from a drift time a point in space on the muon track. Because of its importance and because of its sophistication, the next paragraph is devoted to this routine.

A muon that crosses a  $L_3$  muon chamber creates about 100 ion-electron pairs per cm. All the created electrons start to drift towards the sense (anode) wires along different drift paths.

From the drift time recorded by the TDC connected to the wire one can calculate a point  $P$  with coordinates  $(X(t), Y(t))$  on the muon track. The muon track parameters are determined from a fit through a set of such points collected for all the wires (16 in a MI or MO chamber, and 24 in a MM chamber). In principle all the points  $P$  are points in three dimensional space, but since the  $z$  coordinate is measured independently by the Z chambers, the problem of finding the point  $P$  in the P chambers is treated in 2 dimensions. Corrections as wire sagging due to gravity and relative alignment of the chambers are treated later in the reconstruction program. The function  $(X(t), Y(t))$  is called the cellmap function. A more elaborate description of the first three paragraphs can be found in [37]. Here I will just give a brief introduction to these subjects in order to explain the paragraphs starting with the paragraph "Near-wire corrections" on page 58.

**Mucell: the cellmap function for small slopes ( $|S| \leq 0.5$ )**

The functions  $X(t)$  and  $Y(t)$  are taken to be the same for all the wires in a cell and for all cells. They depend on the magnetic field and the pressure, known quantities, and on the slope of the track, where the slope of the track is the tangent of the angle between the track and the wire plane. The drift time recorded by the TDC, after correction for the zero-time offset and the time of flight differences, is represented by  $t$ . The aim is to find the relations  $(X(t), Y(t))$ , given the pressure and the magnetic field. The different effects to be taken into account are discussed in the following sections: for simplicity, the cellmap function is first explained for zero magnetic field.

**Cellmap for  $B = 0$** 

The cellmap function for zero magnetic field is given by:

$$\begin{aligned} X(t) &= v_x(p)t + c_2 \tilde{S}^2 \\ Y(t) &= y_{\text{wire}} \end{aligned} \quad (3.1)$$

where  $t$  is the corrected drift time,  $v_x(p)$  the drift velocity:

$$v_x(p) = v_{x,o} + p_1 \tilde{p} + p_2 \tilde{p}^2 \quad (3.2)$$

in which  $\tilde{p}$  is given by:

$$\tilde{p} = \frac{\frac{p}{T} - \frac{p_o}{T_o}}{\frac{p_o}{T_o}} = \left( p \frac{T_o}{T} - p_o \right) / p_o \quad (3.3)$$

and in which  $\tilde{S}$  is the reduced slope of the track defined as the tangent of angle  $\zeta$  between the track and wire plane normalised to the tangent of  $22.5^\circ$  (half the opening angle of an octant):

$$\tilde{S} = \tan(\zeta) / \tan(22.5^\circ) \quad (3.4)$$

and  $y_{\text{wire}}$  the  $y$  coordinate of the wire on which the signal arrived.

Figure 3.5 shows the different paths along which electrons drift towards the sense wire. The parabolic shaped lines, called isochrones, connect points of equal drift time on these paths. Point  $Q$  is the position along the track where the first few electrons originate from.

The point  $P = (X(t), Y(t))$  is defined as the point where the track crosses a "standard drift path". In the case of zero magnetic field the line  $y = y_{\text{wire}}$  is used. For a track parallel to the wire planes, the points  $P$  and  $Q$  are the same. If, on the other hand, the track is not parallel to the wire plane, the point  $Q$  does not correspond to  $P$  and the slope dependent correction term is needed.

**Cellmap function for  $B \neq 0$** 

If a magnetic field is present, the particles will drift under an angle  $\alpha$  with respect to the electric field, the so-called Lorentz angle, displayed in figure 3.5B. The first complication

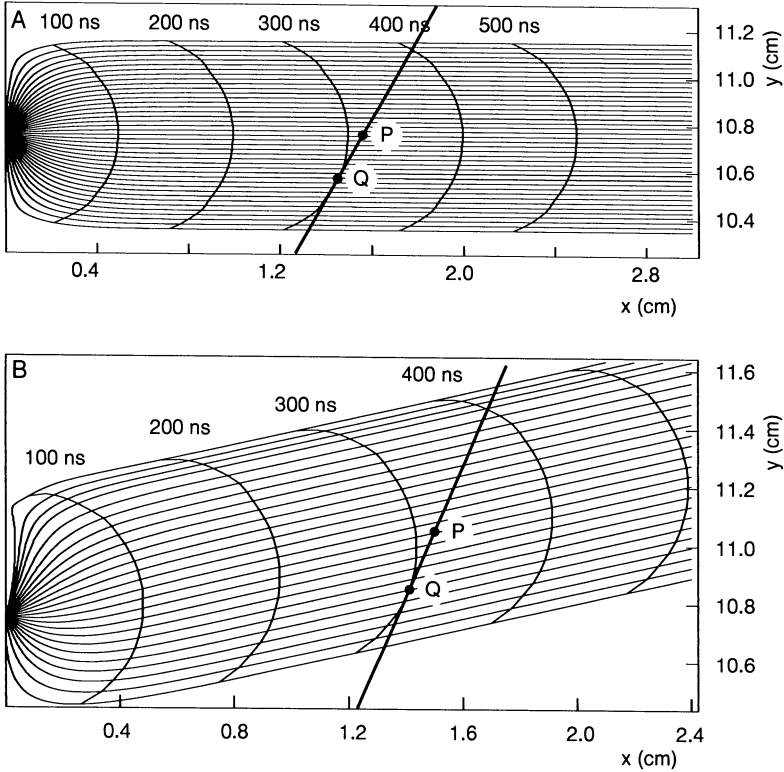


Figure 3.5: The drift paths of the electrons which all end on the sense wire and the isochrones (parabolic shaped lines) in the drift cell showing the position of point P and point Q in case of zero magnetic field (plot A) and in case of non zero magnetic field (plot B).

presented by a nonzero field is this drift angle  $\alpha$ , which varies as function of the electric and magnetic fields and is parametrised as follows:

$$\tan \alpha = c \frac{B}{E/p} = \alpha_o B + \alpha_1 \tilde{p} \approx \tan(18.5^\circ) \quad (3.5)$$

The standard drift path is given by (see figure 3.6):

$$Y(t) = \begin{cases} y_{\text{wire}} & (X(t) \leq d_r) \\ y_{\text{wire}} + I_b \tan(\alpha)(X(t) - d_r) & (X(t) > d_r) \end{cases} \quad (3.6)$$

The shape of this line roughly corresponds to the drift line of the earliest arriving electrons. Very close to the sense wire the electric field increases. Since the drift angle is proportional to  $B/E$  (see equation 3.5), the particles start to drift parallel to the field lines, which are

more or less radial with respect to the sense wire. From extensive Monte Carlo studies the distance  $d_r$ , over which the drift paths are radial, was estimated to be 3.5 mm. The number  $I_b$  is 1 or  $-1$ , depending on the side of the sense plane the particle passed through the cell and on the sign of the magnetic field.

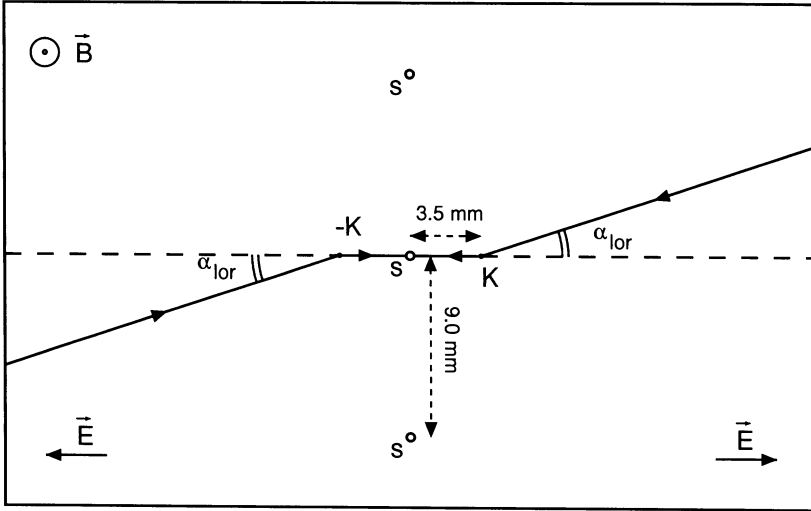


Figure 3.6: Standard drift path (solid line) in a nonzero magnetic field. At small distances from the sense plane ( $d_r < 3.5$  mm), the standard drift path is perpendicular to the sense wire plane.

The geometrical effects in a magnetic field are not symmetric with respect to  $\tilde{S}$ , requiring a correction to  $X(t)$  which is odd in  $\tilde{S}$ . Higher order terms in  $\tilde{S}$  are included to compensate for deviations of the isochrones from a parabola; these terms are only important for large slopes (i.e.  $\tilde{S} \approx 1$ ).

The magnetic field in the vicinity of the  $L_3$  muon chambers varies as function of position. In the middle region the field is approximately 0.51 T, but closer to the doors the field goes up to 0.58 T. This influences the drift velocity and so equation 3.2 is changed to:

$$v_x(\tilde{B}, \tilde{p}) = v_{x,o} + p_1\tilde{p} + p_2\tilde{p}^2 + b_1\tilde{B} \quad (3.7)$$

where the variable  $\tilde{B}$  is introduced, which corresponds to the normalised deviation of the magnetic field from the nominal value of  $B_o = 0.51$  T:

$$\tilde{B} = \frac{(B - B_o)}{B_o} \quad (3.8)$$

The final expression for  $X(t)$ , used in this method is:

$$X(t) = v_x(\tilde{B}, \tilde{p})t + c_o + b_o\tilde{B} + c_1\tilde{S} + c_2\tilde{S}^2 + c_3\tilde{S}^3 + c_4\tilde{S}^4 \quad (3.9)$$

in which the coefficients all have been obtained from test beam data [37].

### Near-wire corrections

Closer than 10 mm to the sense and mesh wires, the electric field starts to deviate strongly from the homogeneous field in the middle region of the cell, see figure 3.5. An attempt was made to include several corrections to  $X(t)$  for these regions. As mentioned before, we need a cellmap function of the following form:

$$x_1 = v_x(\tilde{B}, \tilde{p})t + x_0(\tilde{B}, \tilde{p}, \tilde{S}) \quad (3.10)$$

where  $v_x$  and  $x_0$  are known functions. This map can however not be used near the wires and we need to correct  $x_1$  for near wire effects. This correction takes the form:

$$x_2 = x_1 + F_d(\tilde{S}) \left( \frac{x_d - x_1}{x_d - x_{\text{wire}}} \right)^2 \quad (3.11)$$

where  $x_d$  is the border of the region near the sense or mesh wire plane. Generalising this approach, six areas (three at each wire plane) are distinguished: a border at 10, 6, and 3 mm (near sense) and at 45, 48 and 50 mm (near mesh) from the sense plane respectively. If  $x_1$  is in the smallest near sense area, say  $x_1 = 2$  mm, then  $F_{10}$ ,  $F_6$  (if  $x_2 \leq 6$  mm) and  $F_3$  (if  $x_3 \leq 3$  mm,  $x_1$  is replaced by  $x_2$  in equation 3.11) are applied in succession, giving corrections on corrections. The functions  $F_i(\tilde{S})$  are of the following form (and are not necessarily positive):

$$\begin{aligned} F_{10}(\tilde{S}) &= w_0 + w_1\tilde{S} + w_2\tilde{S}^2 + w_3\tilde{S}^3 \\ F_6(\tilde{S}) &= w_4 + w_5\tilde{S} + w_6\tilde{S}^2 + w_7\tilde{S}^3 \\ F_3(\tilde{S}) &= w_8 + w_9\tilde{S} + w_{10}\tilde{S}^2 + w_{11}\tilde{S}^3 \\ F_{45}(\tilde{S}) &= w_{12} + w_{13}\tilde{S}^2 \\ F_{48}(\tilde{S}) &= w_{14} \\ F_{50}(\tilde{S}) &= w_{15} \end{aligned} \quad (3.12)$$

The constants  $w_0, w_1, \dots, w_{15}$  have been determined from test beam data and are listed in table 3.1.

After setting up this cellmap for the reconstruction, the inverse function is needed to calculate the drift time  $t$  from a known drift distance  $x$  in order to produce events in the Monte Carlo simulation. A problem occurs because the algorithm described above cannot easily be inverted. One way out is to modify the cellmap function slightly and to iterate the correction of equation 3.11 a few times (note that  $x_1$ , the first variable on the right hand side of 3.13, does not change in the iteration):

$$x_3 = x_1 + F_d(\tilde{S}) \left( \frac{x_d - x_2}{x_d - x_{\text{wire}}} \right)^2 \quad (3.13)$$

$\vdots$   
 $\vdots$   
 $\vdots$

$$x_n = x_1 + F_d(\tilde{S}) \left( \frac{x_d - x_{n-1}}{x_d - x_{\text{wire}}} \right)^2 \quad (3.14)$$



This iteration converges rapidly such that  $x_n \rightarrow \tilde{x} = x_\infty$  for  $n$  relatively small. Now the inverse function can be calculated directly from equation 3.10 and 3.13 with  $x_n$  and  $x_{n-1}$  replaced by a given  $\tilde{x}$  as:

$$x_1 = \tilde{x} - F_d(\tilde{S}) \left( \frac{x_d - \tilde{x}}{x_d - x_{\text{wire}}} \right)^2 \quad (3.15)$$

$$\tilde{t} = (x_1 - x_o(\tilde{B}, \tilde{p}, \tilde{S})) / v_x(\tilde{B}, \tilde{p}) \quad (3.16)$$

The number of iterations required depends mainly on  $\tilde{S}$ . Five iterations are enough for  $|\tilde{S}| \leq 1.0$  to guarantee that  $|\tilde{x} - X(\tilde{t})| < 1.2 \mu\text{m}$ . The mathematical details of this problem are described in reference [53].

### Muclbs: cellmap function for big slopes ( $|S| \geq 0.5$ )

The cellmap function, as described in the previous sections, will diverge if the slope becomes too large ( $|S| \geq 0.5$ ). In all cases where the muon has a momentum larger than 7 GeV and originates from the interaction vertex the standard cellmap function will be adequate. But for low momentum inclusive muons, relevant for the analysis presented in this thesis, P segments with slopes larger than 0.5 are possible and they should be reconstructed as well. For that purpose an additional routine to the standard cellmap function, called Muclbs, has been constructed.

### The construction of Muclbs

The parameters of the standard cellmap function were fitted to test beam data. In contrast to this, the parameters used for this cellmap function are partly taken from simulations [54] and partly adapted to real data from the  $L_3$  detector.

The idea is as follows. Instead of taking point  $P$ , see figure 3.5, point  $Q$  is taken to describe a point on the muon track. This has the advantage that the coordinates of this point will always stay inside the cell coordinates whereas the coordinates of  $P$  can get much bigger than the cell coordinates if the muon travels about parallel to the standard drift path, as can be seen in figure 3.5. In order to calculate point  $Q$  a mathematical description to approximate the isochrones is needed.

$w_0 = 0.062$	$w_1 = -0.25$	$w_2 = -0.63$	$w_3 = -0.027$
$w_4 = -0.14$	$w_5 = 0.29$	$w_6 = 0.27$	$w_7 = -0.060$
$w_8 = 0.0037$	$w_9 = -0.050$	$w_{10} = -0.15$	$w_{11} = 0.060$
$w_{12} = -0.050$	$w_{13} = 0.18$	$w_{14} = -0.020$	$w_{15} = -0.74$

Table 3.1: The constants  $w_i$  (in mm) which define the cellmap near wire corrections.

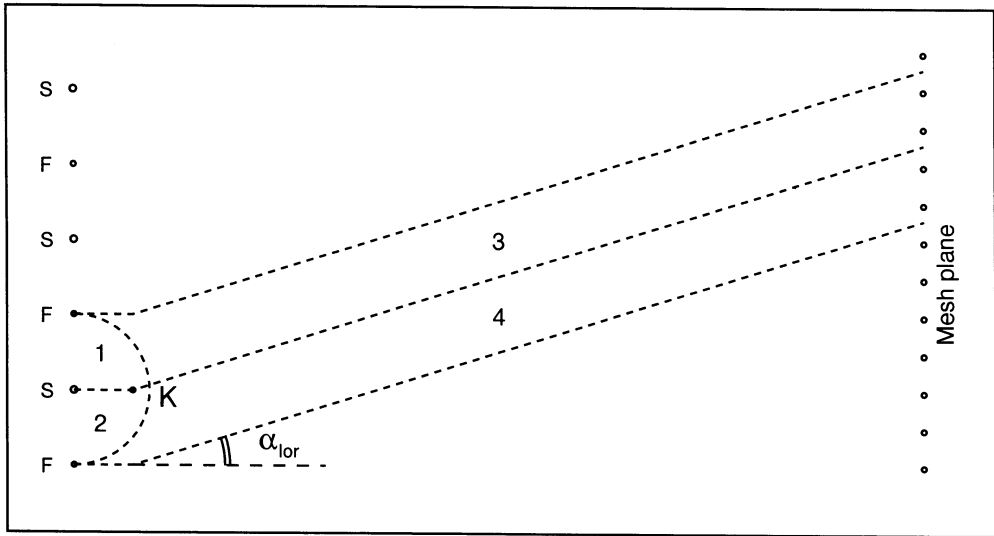


Figure 3.7: The four regions dividing up the drift cell for Muclbs.

Figure 3.7 defines four regions in the drift cell. In region 1 and 2 circular isochrones are assumed, with the sense wire in the origin:

$$x^2 + \left(y - \frac{r}{a}\right)^2 = r^2 \quad \text{for region 1} \quad (3.17)$$

$$x^2 + y^2 = r^2 \quad \text{for region 2} \quad (3.18)$$

The difference between equations 3.17 and 3.18 will be explained later on in this paragraph. Region 3 and 4 are more complicated. The function describing those regions should stay well inside the drift cell and have an approximate parabolic shape. Having these conditions in mind, the following function was taken:

$$x = \frac{by^2}{y^2 - c^2} + d \quad (3.19)$$

From this function only the part inside the asymptotes, see figure 3.8, is taken. This parabolic part is rotated and shifted, in order to get the  $x$  axis of figure 3.8 along the standard drift path to match figure 3.5. Having chosen the function by which the isochrones will be described, the parameters ( $b$ ,  $c$  and  $d$ ) have to be chosen in such a way that three conditions are satisfied:

1. The cellmap for ( $|S| \geq 0.5$ ) has to be continuous with the one for ( $|S| \leq 0.5$ );
2. It has to be continuous between the four different regions;
3. It has to reconstruct real data as well as possible.

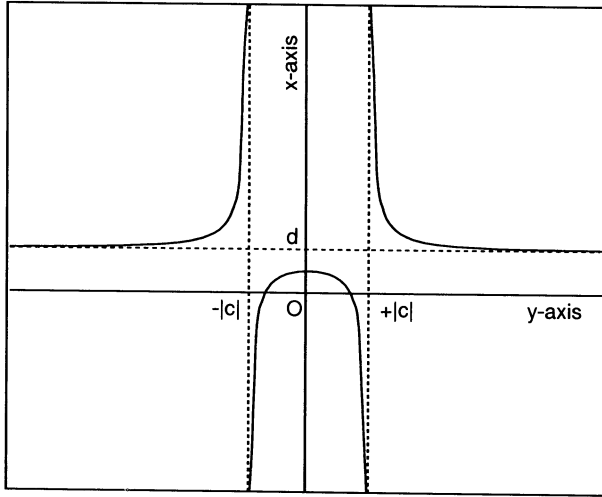


Figure 3.8: The graph of function  $x = \frac{by^2}{y^2 - c^2} + d$  which has been used to construct the cellmap function for large slopes.

The first condition simply implies that  $X(t)$  for  $|S| \leq 0.5$  equals  $X(t)$  for  $|S| \geq 0.5$  in the case that  $|S| = 0.5$  for all  $t$ . This is achieved in the following way.

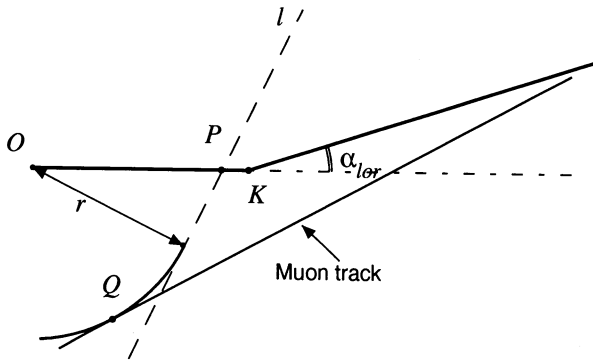


Figure 3.9: Picture to illustrate the algorithm of Muclbs in region 1 and 2.

- Region 1 and 2 (see figure 3.9): point  $P$  on the standard drift path is calculated with given drift time  $t$  and slope  $S = \pm 0.5$ , depending on the region (1 or 2) by using MuCell. Then the distance from the origin of the circle to the line  $l$  going through  $P$  with slope  $S = \pm 0.5$  is determined. This distance will be the radius  $r$  of the circle.

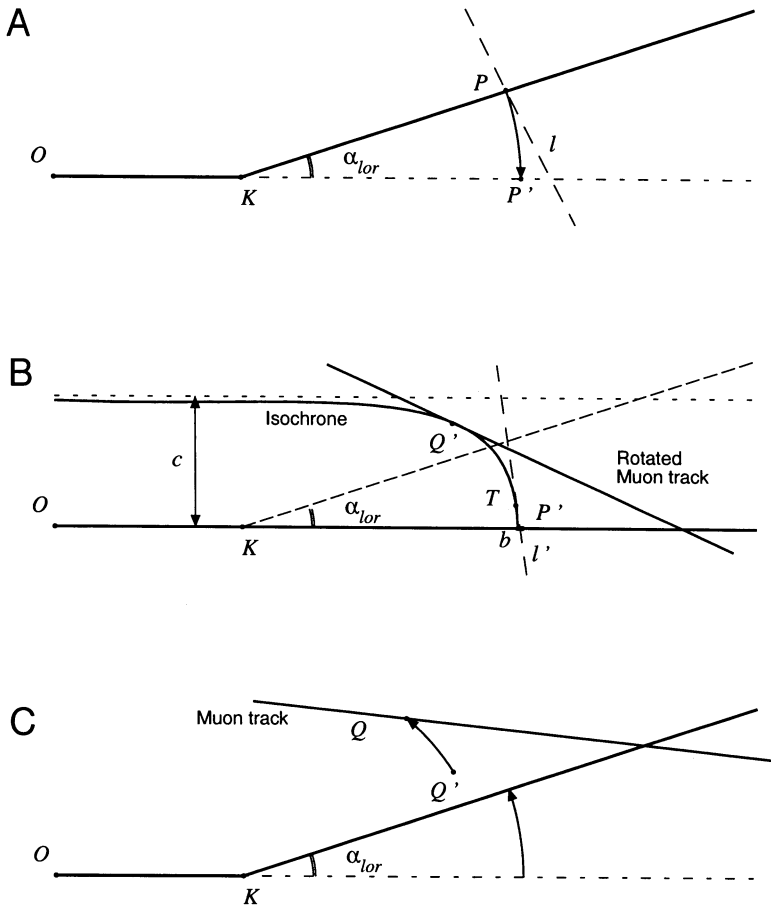


Figure 3.10: Three pictures to illustrate the algorithm of Muclbs in region 3 and 4.

- Region 3 and 4 (see figure 3.10): line  $l$  with slope  $\pm 0.5$  and point  $P$  on the standard drift path, calculated with given drift time  $t$  and slope  $S$ , are turned over the Lorentz angle around point  $(3.5, 0)$ , the point where the standard drift path changes direction:  $P'$ ,  $l'$  and  $S'$  see figure A and B.

In figure B, the position of the asymptotes and point  $T$ , the point on line  $l'$  through  $P'$  and on the isochrone, are imposed. Then the parameters  $b$ ,  $c$  and  $d$  are known. After this the position of point  $Q'$  is calculated by parallel shifting a line with slope  $S'$  until it touches the isochrone. The point where they touch is  $Q'$ .

Finally, in figure C,  $Q'$  is turned back over the Lorentz angle to get  $Q$  and the point on the track is reconstructed.

The second condition means that in between the regions 1 and 3 and in between 2 and 4, there should not be a region of points through which no isochrone or two isochrones can go. This is, however, inevitable and the best that could be done (so far) is to introduce the  $\frac{\tau}{a}$  term in equation 3.17 to make the region between 1 and 3 as small as possible, see figure 3.11. The value for parameter  $a$  is chosen to be 2.0.

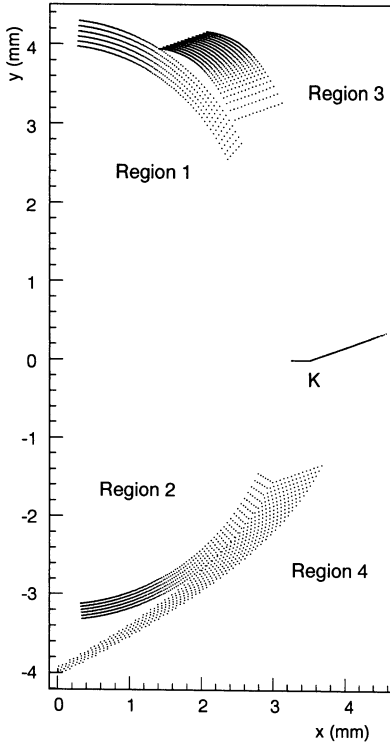


Figure 3.11: *Isochrones showing, the discontinuity between the regions 1, 2 and 3, 4. The drift time ranges from 81 ns to 101 ns with steps of 1 ns. For slopes in between  $-0.5$  and  $0.5$  point  $Q$  is projected on the standard drift path which gives the solid line in the area of  $y \approx 0$ .*

Finally figure 3.12 shows the result of this algorithm. The isochrones are drawn discontinuously because in the region  $|S| \leq 0.5$  the cellmap for small slopes is used which maps everything onto the standard drift path.

### The construction of the inverse Smpths

In the Monte Carlo package SIGEL3 a muon will give a track through a drift cell. This track will cross the standard drift path in point  $P$  which is calculated. At this point, only the coordinates of this point  $P$  and the local slope  $S$  are known. With these two quantities the drift time  $t$  has to be constructed. First the region (1, 2, 3 or 4) for point  $Q$  is determined and then the parameters of the isochrone that will touch this muon track are calculated. Knowing the isochrone the drift time can be calculated by extrapolating the isochrone to the standard drift path for  $|S| = 0.5$ . The drift distance drift time relationship for small slopes will give the drift time  $t$ .

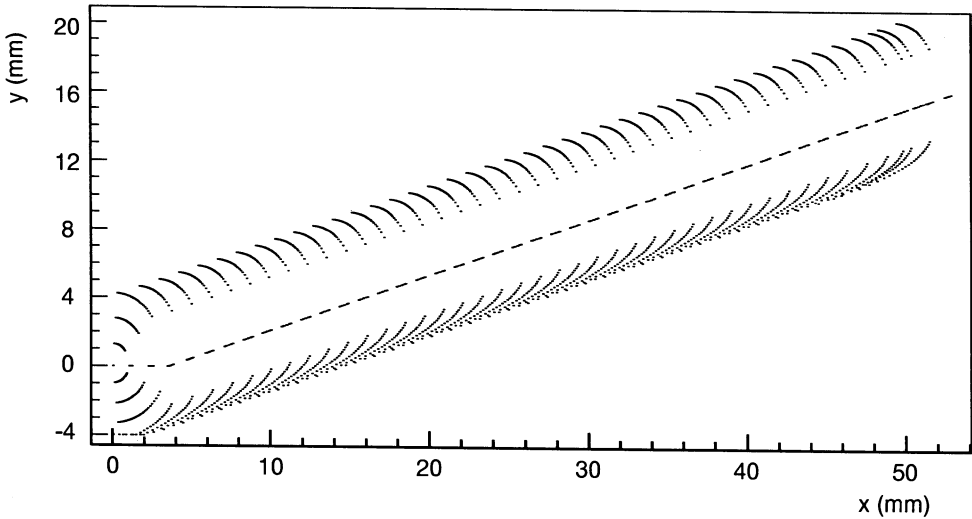


Figure 3.12: The isochrones as produced by *Muclbs* and the projection of the isochrones on the standard drift path by *Mucell*.  $\Delta t = 10$  ns.

Figure 3.13 shows the maximum difference,  $M(S)$ , as a function of the slope  $S$ , with  $M(S)$  defined as

$$M(S) = \max |x - C(I(x, S), S)| \quad \text{for} \quad x \in [0.0 \text{ mm}, 50.7 \text{ mm}] \quad (3.20)$$

in which  $C(t, S)$  represents the cellmap function,  $I(x, S)$  its inverse and  $x$  the distance from the sense plane. Figure 3.13 A displays the region for small slopes and figure 3.13 B shows the complete slope domain. From plot A it can be concluded that the error stays well below  $1.2 \mu\text{m}$  which should be small compared with real data. Plot B shows a discontinuous behaviour in the areas where the absolute value of the slope is around 2.0, which is explained by the existence of the discontinuous areas in the cellmap for big slopes. Despite this deficiency of the cellmap the error stays well below  $100 \mu\text{m}$  which is much better than in the case of real data.

From tuning the parameters to real data it was found that the displacement in the  $xy$  plane is less than 3 mm even for very big slopes.

### 3.3.2 The $L_3$ muon P pattern recognition

The starting point of the pattern recognition of tracks in the muon P chambers is the investigation of the drift times from three neighbouring cells. Using a first order approximation of the drift time drift distance relation (see section 3.3.1), each drift time yields two ambiguous points in the  $xy$  plane: a left and a right one, since the drift time does not carry

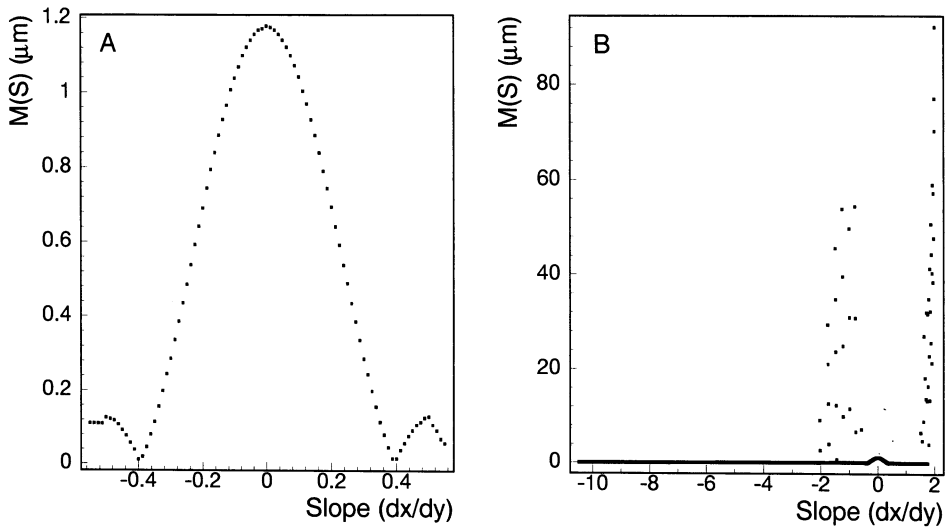


Figure 3.13: Maximum difference  $M(S)$  as a function of the slope (see text). Plot A shows the region for  $|S| < 0.55$  and plot B displays the region from  $-10.5$  to  $2.0$ .

any information on whether the particle's trajectory is situated on the left or on the right side of the sense wire.

Each pair of consecutive wires gives four points which form two ambiguous vectors in  $xy$  space by combining the two left points and the two right points. The slope and the intercept with a horizontal of all vectors in the three cells are put in a two dimensional histogram. The bin with most entries gives a straight line, the first approximation for a track segment candidate. All points closer to this straight line than a certain threshold, are used to fit a parabola. At this stage in the reconstruction a parabola is a good approximation to a circle. Through all ambiguous points a parabola is fit as well to avoid losing a valid segment candidate too early.

A "drop-and-pick" algorithm is used to improve these segment candidates. The ones that remain are called P segments and the procedure for finding tracks is repeated with the drift times that have not been used so far.

Figure 3.14 shows the flowchart of the P chamber pattern recognition part. Mupseg is the driving routine that loops over all muon cells that are "hit", i.e. sense wires in those cells received a signal.

Starting from octant 0, going from MI via MM to MO, all eight<sup>1</sup> octants are looped over. As seen in figure 3.14, the first routine called in this loop is Mupmap, the routine that creates a local map of the cell with a hit and (if possible) its two neighbouring cells.

<sup>1</sup>At this moment there is no  $z$  information yet, so there is no differentiation between Master and Slave Ferris wheel.

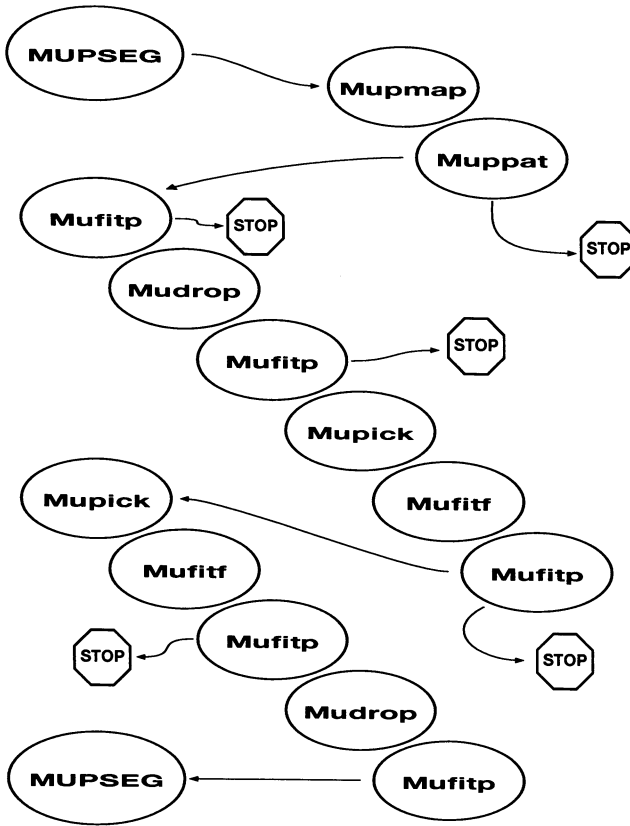


Figure 3.14: Flow diagram of one loop over a cell in the muon pattern recognition programme, Mupseg. If a "stop" sign is encountered the pattern recognition in this cell is aborted and the next cell with a hit is investigated.

This means that for these three<sup>2</sup> cells the identifiers of the wires with hits are stored along with the number of (consecutive) hits on that wire.

The next routine being called is the most important one. Muppat performs the actual pattern recognition as sketched above and patterns not found at this stage are lost. Muppat uses a so-called histogram method to recognise patterns in the local map of the three cells. First of all Muppat checks if the hits are distributed uniformly over the three cells: if the number of hits in the left cell is below two and the number of hits in the right cell is above two the pattern recognition will stop and it shifts one cell to the right. An average time of flight correction is calculated for all hits in these cells by assuming the average  $z$  coordinate

<sup>2</sup>For the rest of this description I will assume that the primary cell is not an edge cell and has therefore two neighbours.



of  $0.4y$ . This correction is applied to all drift times found in these three cells. In the next step all drift distances, are estimated by using a first order approximation of the cellmap:

$$X(t) = (t - t_{\text{cor}})v_{x,o} + c_1 \quad (3.21)$$

$$Y(t) = \begin{cases} y_{\text{wire}} & (X(t) \leq 3.5 \text{ mm}) \\ y_{\text{wire}} + I_b \cdot \tan(\alpha) \cdot (X(t) - 3.5 \text{ mm}) & (X(t) > 3.5 \text{ mm}) \end{cases} \quad (3.22)$$

In this way, each wire is associated with two coordinate pairs, viz. a left and a right side solution, see figure 3.15. These coordinates are grouped two by two (left by left and right

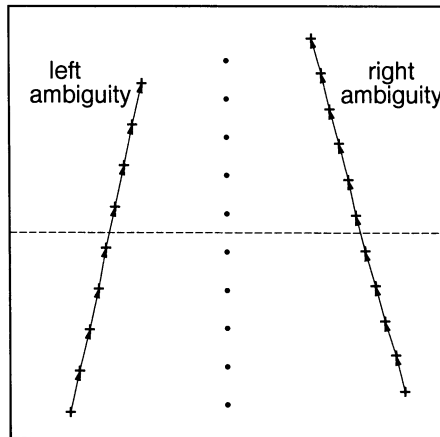


Figure 3.15: This plot shows the result of the first step of the pattern recognition. For each pair of neighbouring wires two vectors are created.

by right) to form two vectors in a two dimensional space.

The two properties of the vectors, the slope and the intercept with the horizontal line perpendicular through the middle of the sense plane (see figure 3.15), are stored in a two dimensional histogram. In this way the histogram gets about twice as many entries as hits in the three cells. Figure 3.16 shows this histogram for a complicated real situation. The two spikes in this histogram stand for the two left right ambiguities<sup>3</sup> of which the larger one belongs to the segment that was finally chosen by Mupseg and which is drawn in the three cells. All hits in the first cell are accepted, 4 hits in the second cell are dropped and 3 hits in cell 3 were never considered. This relatively low efficiency is due to the fact that the slope is very large (see section 3.3.1).

Once the histogram is created, it is scanned for the highest population in a 2 bins by 2 bins square. The average slope  $b$  and intercept  $c$  are calculated and a first approximated P segment candidate is found:

$$x = by + c \quad (3.23)$$

<sup>3</sup>The term "ambiguity" will also be used for "one of the ambiguous solutions".

Having found this straight line, the pattern recognition starts all over again only this time with the knowledge of the segment candidate: Muppat loops over all wires and calculates the distance of each drift point  $P$  to this segment. If this distance is smaller than a certain threshold the hit is accepted as belonging to this  $P$  segment. At the end the number of accepted hits,  $N_{\text{hits}}$  and the parameters  $b$  and  $c$  are stored for further use.

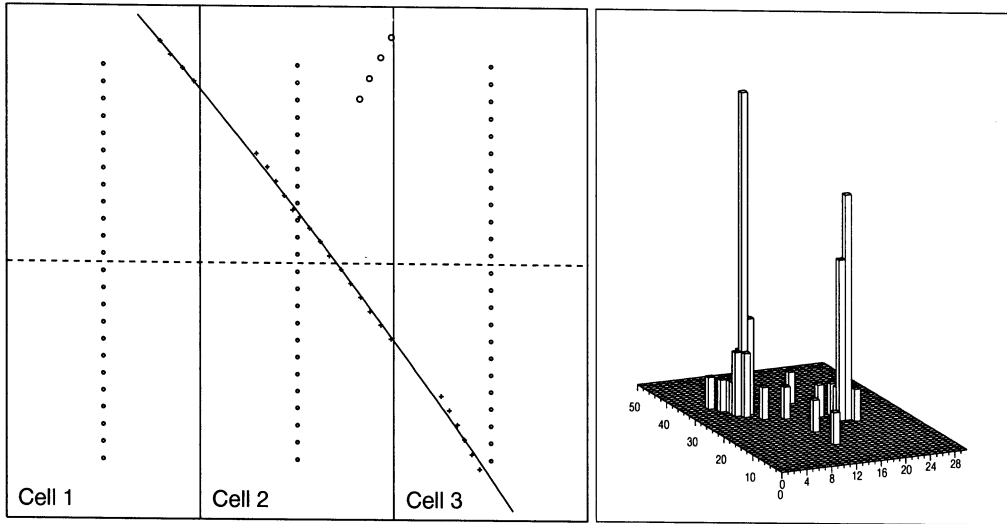


Figure 3.16: The left picture shows three cells in a MM muon chamber in which a charged particle created 32 hits. The small closed circles are the sense wires, the plusses are the hits that are accepted by Mupseg and the open circles stand for hits that were accepted but dropped later on. With these 32 hits the two dimensional histogram, shown on the right side, was filled.

If  $N_{\text{hits}}$  is too small, less than 6 for MI or MO and less than 9 for MM, pattern recognition in this cell is stopped and the next cell is tried. This check is performed after every step in the pattern recognition. If on the other hand,  $N_{\text{hits}}$  is large enough a parabola will be fit to the accepted hits using a  $\chi^2$  fit. Using the corrected drift time, the slope  $b$ ,  $x_{\text{wire}}$  and  $y_{\text{wire}}$  as input, Mucell will now calculate precisely point  $P$  in  $(x,y)$  space. With these coordinates the three parameters of the parabola are calculated and stored for later use. Monte Carlo simulations have shown that the pattern recognition is 100% efficient for muon tracks that pass through a muon chamber by crossing three or less cells.

Now a "drop-and-pick" algorithm is started. This algorithm is tuned to the Monte Carlo to maximise its efficiency. Addition of more "drop-and-pick" loops in the algorithm is shown to be unnecessary. Hits that contribute most to the  $\chi^2$  will be dropped. This deactivation occurs if there is a hit that has a distance in  $x$  from the fitted parabola larger than 1 mm. The parabola is recalculated and the drop procedure starts all over again until finally the maximum deviation is smaller than 1 mm. With this new situation of used hits, the parabola is refitted and a routine to recover (lost or never used before) hits, is started.

So far, the pattern recognition has only found one ambiguity of the, in principle, two possible P segments, see figure 3.17. At this stage in the muon reconstruction, the rejection of one of the two ambiguities is only possible if it is certain that a P segment crosses a cell boundary and has hits in two adjacent cells, see figure 3.16. The segment chosen so far

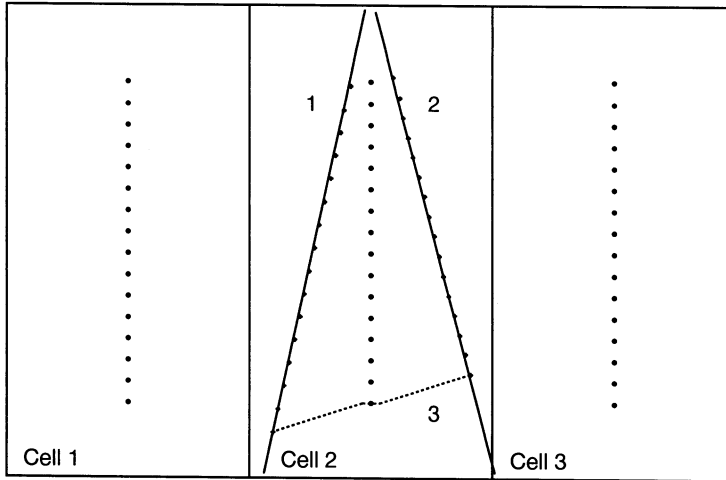


Figure 3.17: *This picture shows the fundamental problem in solving left-right ambiguities if no cell boundaries are crossed: solution 1 can be just as valid as solution 2. Only if one of the two does not match with another P segment while the other one does, this can be solved. The dashed line (3) in the picture is the standard drift path.*

was picked by the histogram method of Muppat assuming a straight line P segment. Since, at this point, the knowledge about the P segment is certainly not sufficient to decide that the segment chosen is the only one possible, the ambiguous segment is created as well.

The three parameters of the parabola of the flipped P segment are calculated by taking the "mirror image" of the parabola in the sense plane, taking the Lorentz angle into account, as shown in figure 3.17. Starting from these parameters a parabola to the hits on the other side of the sense wire plane is fit. From now on the pattern recognition has to loop over two segment candidates.

By looping over all wires in the three cells additional hits are picked up. For every wire, the hit closest to the parabola is tested to see if it is closer than 5 mm and if so it is accepted. During the loop over one ambiguity the number of hits picked up in each of the three neighbouring cells is counted and the middle value is saved. The number of wires without picked up hits, no hits at all or too far off (i.e. more than 6 mm), while they should have been picked up are counted as well.

A first attempt is made to solve the left right ambiguity problem. An ambiguity is thrown away if one of the following conditions is satisfied:

- 1: The ambiguity has too few hits, i.e. less than 3, accepted.
- 2: One of the two ambiguities crosses a cell boundary and picks up at least six hits more in the neighbouring cell than the other, see for instance figure 3.16.
- 3: One ambiguity misses at least 8 hits more than the other.
- 4: The ambiguities have more than 50% of the hits in common which can occur if the track is very close to the sense wire plane and one solution crosses the plane while the other is parallel to it. In this rare case the solution that was found first is kept.

A parabola is fitted to the new situation of picked up hits. This is applied in parallel on both versions if the second ambiguity is still present. The pick algorithm is applied again after which the drop algorithm is used, only this time with a threshold of 2 mm in stead of 1 mm and it may have to loop over two ambiguous segment candidates.

If, after this series of picking and dropping hits, the number of accepted hits is still large enough the parabola is converted into a circle with the parametrisation explained in box 3.1.

All hits that are used for a P segment are marked and Mupseg returns to see if in the same cell another P segment can be found. This is done until the number of accepted hits is below the limit ( $< 6$  for MI or MO and  $< 9$  for MM) and the loop in Mupseg continues to the next cell until the last one is reached. All important properties of the P segment(s) are stored to be used by the matching algorithm discussed next.

### 3.3.3 The segment matching algorithm

The combination of the independently reconstructed P segments and Z tracks is done octant by octant. In each octant all possible combinations of reconstructed Z tracks and one, two or three P segments are investigated, where only combinations of P segments from different chamber layers, MI, MM or MO, are considered. The P segments are refitted using the time of flight and time of propagation corrections corresponding to the  $yz$  information of the associated Z track. Depending on how many P segments (three or two) are matched with one Z track, a specific  $\chi^2$  test is performed on this candidate muon track. All resulting tracks in one octant are tested for consistency with one and other: tracks that share P segments are considered inconsistent. If two tracks are inconsistent, the track with fewer P segments is rejected.

All the hits on the resulting tracks are recalculated taking into account all chamber alignment and wire sag corrections. Through these recalculated hits a "swim" fit is performed taking the deviations from the nominal magnetic field, the energy loss and the multiple scattering into account.

Tracks found in different octants are investigated to see if they could be combined in one track. All the tracks are then back-tracked from the muon chambers through the calorimeters to the interaction region, giving a first approximation of the momentum and direction of the track at the vertex.

The  $\chi^2$  test used for combinations of three P segments, triplets, is defined as follows. For every P segment a set  $(x, y, S, C)$  is known with  $(x, y)$  the coordinates in the middle of the cell on the circle,  $S$  the local slope at  $(x, y)$  and  $C$  the curvature of the circle. Through

### Box 3.1 Muon trajectory representations in $L_3$

A muon trajectory is represented by a helix, which corresponds to a particle moving circularly in one direction and along a straight line in the perpendicular direction. A helix can be represented by a circle and a sine going through a reference point  $P$  which for simplicity is taken to be  $(0, 0)$ .

For  $P$  segments a parabola is a good enough approximation for a circle and has the advantage that it can easily be fit through any number of points. Subsequently, the parabola is converted to a circle.

The circle is represented by its curvature  $C_0$  which is the inverse of the radius  $R$  and by a normalised vector  $(\alpha, \beta)$ ,  $(\alpha^2 + \beta^2 = 1)$ , pointing to the centre of the circle from the reference point:

$$C_0(x^2 + y^2) - 2\alpha x - 2\beta y = 0$$

This representation was chosen because of the following advantages:

- $C_0 = 0$  is equivalent with a straight line.
- It involves no subtractions of large numbers in contrast to the 'normal' circle representation, which makes this form more reliable on accuracy limited computers.
- It is very easy to recompute  $(\alpha, \beta)$  if the reference point on the circle is changed.

The sine can be represented by one parameter,  $\gamma$ :

$$\sin\left(\frac{zC_0}{\gamma} - \arcsin(\beta)\right) + C_0(\beta - y) = 0$$

with  $\gamma/\alpha = \tan(\theta)$ ,  $\theta$  the (pitch) angle between the plane  $z = 0$  and the direction of the sine in the reference point  $P$ .

A muon track is completely represented by :  $P, C_0, \alpha, \beta$  and  $\gamma$ .

the three sets of  $(x, y)_i$  a circle is computed and of this circle the slopes,  $S'_i$ , at the three points  $(x, y)_i$  are calculated. With these quantities the  $\chi^2$  is defined as:

$$\chi^2 = \frac{\Sigma(S_i - S'_i)^2}{\sigma_S^2} + \frac{\Sigma(C_i - C')^2}{\sigma_C^2} \quad (3.24)$$

The  $\sigma$ 's used in this formula are chosen such that good triplets are not lost due to P segments with a bad fit at this stage of the reconstruction.

If the  $\chi^2$  is less than a certain threshold the combination of P segments in question is accepted as a "good" triplet. If no "good" triplets in this octant are found the  $\chi^2$  value is compared with ten times this threshold and if smaller the combination is accepted as a "bad" triplet.

Due to the angular acceptance of the muon chambers in the  $xy$  plane (gaps between octants) and, more importantly, in the  $yz$  plane (see figure 2.3) and due to wire cells that are not operational, tracks may consist of only two or even one P segment. The  $\chi^2$  test used for matching two P segments, doublets, is defined as follows. From the two P segments two sets,  $A$  and  $B$ ,  $(x, y, S, C)$  are known just as for triplets. From  $(x, y, S)_A$  and  $(x, y)_B$  a circle curvature is calculated:  $C_1$ . From  $(x, y)_A$  and  $(x, y, S)_B$  the same is done:  $C_2$ . Then the average is taken:  $C = \frac{1}{2}(C_1 + C_2)$  and the  $\chi^2$  is defined as follows:

$$\chi^2 = \frac{(C_A - C)^2 + (C_B - C)^2}{\sigma_{AB}^2} + \frac{(C_1 - C)^2 + (C_2 - C)^2}{\sigma_{12}^2} \quad (3.25)$$

Again the  $\sigma$ 's are chosen such that the matching is 100% efficient. Remaining singlets might later on be matched with tracks in the other octants.

After finishing all combinations quality checks are performed to reject "bad" triplets if they use a P segment that is also used by a "good" triplet and to reject tracks that use P segments that are also used by other larger tracks. Equally long tracks that share one or two P segments are kept. In order to reach the resolution aimed for as described in section 3.3 the three dimensional position of each wire has to be known with an accuracy as good as 30  $\mu\text{m}$ . For this purpose, all hits are calculated once again, only this time using all alignment and sagging corrections of that particular wire with respect to the global experiment coordinates. This information is present in the muon database, described in section 2.10.

Now the best approximation of hits on the muon track are known and a swim fit through all these hits is performed to find the best solution of the muon track. This fit is done by using the average tracking and error propagation package GEANE [55]. This package makes use of the accurate description of the geometry of the muon detector and uses the predictions given by GEANT about the interaction of the muon with the detector materials. In this way the best average muon track in the muon detector itself is found.

So far, all muon tracks are limited within the geometry of one octant. Tracks from different octants are tested to see if they can be fit on one trajectory covering more than one octant. Rare muon tracks with more than three P segments can be formed in this way. All the muon tracks are then back-tracked through the calorimeters to the interaction region using GEANE to give a first approximation of the momentum and position of the

muon at the vertex. Energy losses and multiple scattering, especially in the calorimeters, are calculated by GEANT. The muons obtained this way will be used by AXL3 to create the final reconstructed muon tracks: the so-called Amui's.

### 3.4 AMUI: combining all information

All the subdetector packages have finished their local reconstruction and now AXL3 will try to link all these building blocks together to form the earlier mentioned final reconstructed objects. For the part of AXL3, that tries to find the best reconstructed muon track parameters, four subdetectors, besides the muon chambers themselves, are important: TEC, ECAL, HCAL and MFLT. The flow diagram of the part of AXL3 that is specific for muon tracks is shown in figure 3.18.

As stated before, at the end of MUL3, all muon tracks found were back-tracked to the vertex region, i.e. the TEC area. During this back-tracking all errors on the track parameters are propagated to this region as well. A very first attempt to solve possible ambiguities is performed by crudely matching the muon track with the calorimeter hits. The ambiguity that clearly misses calorimeter hits while the other matches them, is rejected. Muon tracks, not originating from the inner detector region, are not further investigated by AXL3.

An attempt is made for the remaining muons to find a match with a TEC track. To describe the quality of this match, for each combination a  $\chi^2$  is calculated:

$$\chi^2 = (\vec{x} - \vec{\xi}) V (\vec{x} - \vec{\xi}) \quad (3.26)$$

with  $\vec{x}$  and  $\vec{\xi}$  are defined as:

$$\begin{aligned} \vec{x} &= \left( \frac{Q}{p}, \phi, x \right)_{\text{TEC}} \\ \vec{\xi} &= \left( \frac{Q}{p}, \phi, x \right)_{\text{MUTK}} \end{aligned} \quad (3.27)$$

where  $V$  is the inverse of the covariance matrix (weight matrix) of the measured  $\vec{x}$  and  $\vec{\xi}$ :  $V = (\sigma_{\text{MUTK}}^2 + \sigma_{\text{TEC}}^2)^{-1}$ . Figure 3.19 shows an event before and after performing the TEC matching algorithm.

With this new constraint on the muon track an improved trajectory through the calorimeters is computed as described in reference [56]. Energy depositions in ECAL, HCAL and MFLT are picked up if they are consistent with a minimum ionising particle and if so the track parameters are adapted to these calorimeter hits.

Finally a global fit is performed to obtain the best information of the muon track at the interaction vertex. For this purpose the following variables are used: all parameters measured in the muon chambers,  $Q/p$ , the  $x$  and  $\phi$  of the matching TEC track, the  $z$  of the fill vertex, the  $z$  of the HCAL hits, the  $x, y, z$  of the ECAL hits and the  $x, y$  of the MFLT hits.

Using all information from the other subdetectors, AXL3 will try to solve the ambiguities, setting a flag for the best one. Those muons not originating from the primary vertices are

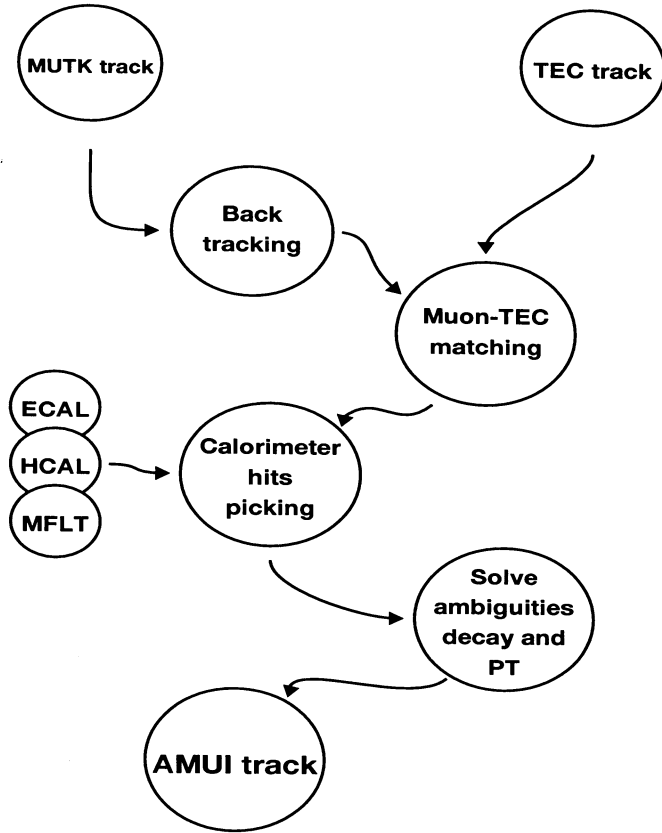


Figure 3.18: Flow diagram of the muon part of the package AXL3. The finally created object is called an AMUI track.

given a special tag as well. This can help the analysis groups to decide whether an AMUI could originate from a prompt  $b \rightarrow \mu$  decay at the vertex or from a  $\pi \rightarrow \mu$  decay somewhere in the middle of a jet in HCAL.

### 3.5 The resolution of the muon chamber system

Figure 3.20 shows the momentum spectrum for  $Z^0 \rightarrow \mu^+ \mu^- (\gamma)$  events. A Gaussian fit to the data gives a momentum resolution,  $\rho = \sigma_{1/p}/(1/p)$ , of 3.1% (2.1%) for triplets and 21% (14%) for doublets at 45 GeV where the numbers in parenthesis are for Monte Carlo.

In contrast to what was mentioned in 2.10, the Monte Carlo used for the analyses described in this thesis, has not been corrected for malfunctioning wires or other non-constant effects affecting the performance of the muon chambers. In order to eliminate the



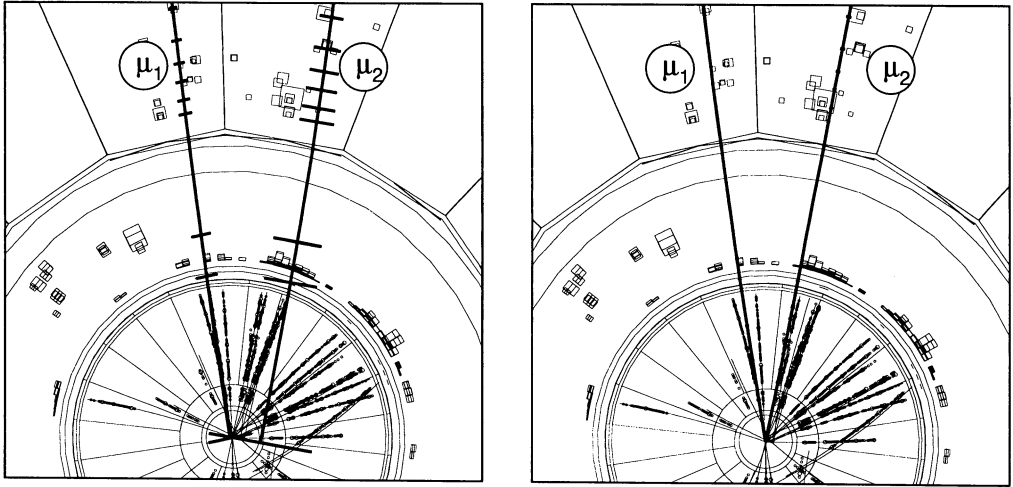


Figure 3.19: An event before (left) and after (right) performing the TEC matching algorithm.

differences between data and Monte Carlo, the Monte Carlo momenta are smeared with a Gaussian distribution until the two spectra are the same, see figure 3.21. This procedure guarantees that the Monte Carlo predicts the same fraction of events above and below a certain cut in this spectrum.

Since the momentum resolution is momentum dependent a Monte Carlo study is made to investigate this behaviour. Figure 3.22 shows the result of this procedure. Also shown in this figure is the parametrisation of this momentum dependence:

$$\rho^2 = \left[ \frac{\sigma_{1/p}}{1/p} \right]^2 = \alpha^2(p - 2.5)^2 + \beta^2 + \frac{\gamma^2}{p^2} \quad (3.28)$$

with the Amui muon momentum,  $p$ , in GeV. The term 2.5 (GeV) in the above expression is the average energy loss of the muon in the calorimeters. The parameters  $\alpha$ ,  $\beta$  and  $\gamma$  in equation 3.28 represent the following three contributions:

- $\alpha$ : the intrinsic resolution of the muon chamber system;
- $\beta$ : the multiple scattering in the muon chambers;
- $\gamma$ : the energy loss in the inner detectors.

Assuming that the multiple scattering ( $\beta$ ) and the energy loss ( $\gamma$ ) are well simulated, the Monte Carlo resolution has to be changed by:

$$\rho_{\text{smear}}^2 = \rho_{\text{data}}^2 - \rho_{\text{Monte Carlo}}^2 = (\alpha_{\text{data}}^2 - \alpha_{\text{Monte Carlo}}^2)(p - 2.5)^2 \quad (3.29)$$

or

$$\rho_{\text{smear}} = \sqrt{(\alpha_{\text{data}}^2 - \alpha_{\text{Monte Carlo}}^2)(p - 2.5)} = \Delta_{\alpha}(p - 2.5) \quad (3.30)$$

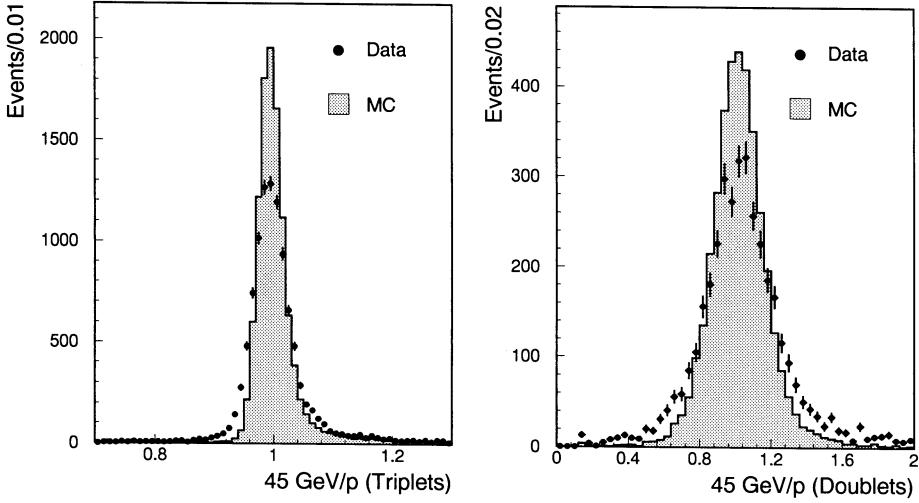


Figure 3.20: Momentum,  $p$ , distributions for  $Z^0 \rightarrow \mu^+ \mu^- (\gamma)$  events. The dots are data and the histograms are Monte Carlo. Left plot: triplets, right plot: doublets.

Taking  $\rho_{\text{Monte Carlo}}^2$  and  $\rho_{\text{data}}^2$  from figure 3.20 for the  $Z^0 \rightarrow \mu^+ \mu^- (\gamma)$  events, equation 3.30 can be used to adapt the multi hadron Monte Carlo, making sure that it describes the lower momentum inclusive muon tracks accurately as well. The values used for  $\Delta_\alpha$  are:

$$\Delta_\alpha = \begin{cases} (0.054 \pm 0.001)\% & \text{for triplets} \\ (0.37 \pm 0.01)\% & \text{for doublets} \end{cases} \quad (3.31)$$

For the systematic error analysis in the forthcoming analysis chapters the error on  $\Delta_\alpha$  will be estimated to be 30% to take into account possible deviations at lower momenta.

### 3.6 Inefficiencies of reconstructed data muons with respect to Monte Carlo

Since the multi hadron Monte Carlo describes the response of a perfect detector and does not take into account malfunctioning wires, noise and other unexpected or non constant effects, the Monte Carlo predicts not only better resolutions, but more muons as well.

Several methods are used to estimate this inefficiency which are described in references [57, 58]. For estimating this inefficiency, muons with at least two P segments and at least one Z segment are required. Here only one of the methods will be explained and the results are compared with the other methods.

By counting the number of muon tracks with  $p$  P segments and  $z$  Z segments in the data sample as well as in the Monte Carlo, a global inefficiency is calculated. This method takes

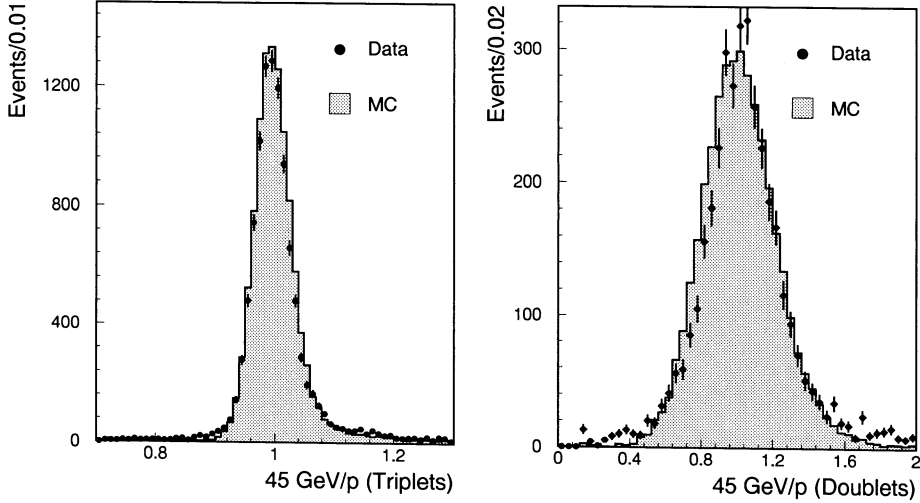


Figure 3.21: Momentum,  $p$ , distributions for  $Z^0 \rightarrow \mu^+ \mu^- (\gamma)$  events. The dots are data and the histograms are smeared Monte Carlo. Left plot: triplets, right plot: doublets.

the number of the muon tracks with 3 P and 2 Z segments,  $N_{32}$ , 3 P and 1 Z segments,  $N_{31}$ , 3 P and 0 Z segments,  $N_{30}$ , 2 P and 2 Z segments,  $N_{22}$ , 2 P and 1 Z segments,  $N_{21}$  and 2 P and 0 Z segments,  $N_{20}$  from the data and the Monte Carlo sample. The addition of the subscript  $M$  means Monte Carlo and the subscripts  $MP$  stand for adjusted Monte Carlo (Monte Carlo prime). To avoid dependence on normalisation, partial widths or branching ratio differences between data and Monte Carlo, all these numbers are divided by the sum of the six numbers. Thus two sets of six fractions are obtained.

It is assumed that the probability to lose a P segment due to a malfunctioning cell or due to data reconstruction problems is  $\eta$  whereas the probability to lose a Z segment when it is a 2 Z segment track is  $\epsilon_2$  and the probability to lose a Z segment when it is a 1 Z segment track is  $\epsilon_1$ . Then the adapted number of muon tracks with  $p$  P and  $z$  Z segments can be calculated:

$$\begin{aligned}
 N_{20MP} &= N_{20M}(1-\eta)^2 \\
 &\quad + N_{21M}(1-\eta)^2\epsilon_1 \\
 &\quad + N_{22M}(1-\eta)^2\epsilon_2^2 \\
 &\quad + N_{30M}3\eta(1-\eta)^2 \\
 &\quad + N_{31M}3\eta(1-\eta)^2\epsilon_1 \\
 &\quad + N_{32M}3\eta(1-\eta)^2\epsilon_2^2 \\
 N_{21MP} &= N_{21M}(1-\eta)^2(1-\epsilon_1)
 \end{aligned}$$

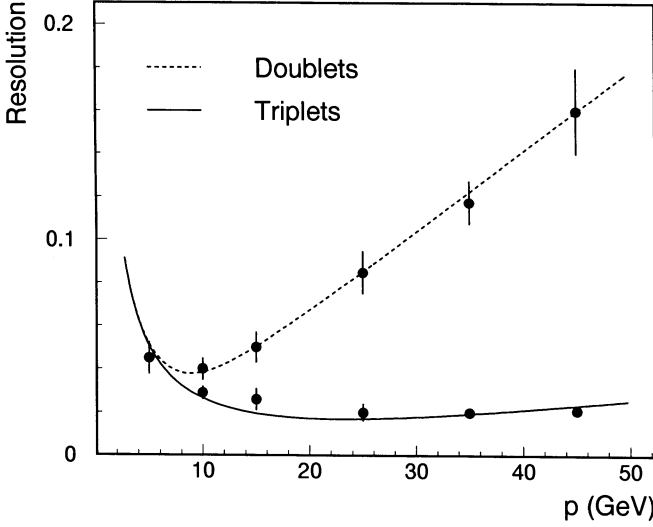


Figure 3.22: Momentum dependence of resolution for triplets and doublets in the Monte Carlo before smearing.

$$\begin{aligned}
 & +N_{22M}2(1-\eta)^2\epsilon_2(1-\epsilon_2) \\
 & +N_{31M}3\eta(1-\eta)^2(1-\epsilon_1) \\
 & +N_{32M}6\eta(1-\eta)^2\epsilon_2(1-\epsilon_2) \\
 N_{22MP} = & N_{22M}(1-\eta)^2(1-\epsilon_2)^2 \\
 & +N_{32M}3\eta(1-\eta)^2(1-\epsilon_2)^2 \\
 N_{30MP} = & N_{30M}(1-\eta)^3 \\
 & +N_{31M}(1-\eta)^3\epsilon_1 \\
 & +N_{32M}(1-\eta)^3\epsilon_2^2 \\
 N_{31MP} = & N_{31M}(1-\eta)^3(1-\epsilon_1) \\
 & +N_{32M}2(1-\eta)^3\epsilon_2(1-\epsilon_2) \\
 N_{32MP} = & N_{32M}(1-\eta)^3(1-\epsilon_2)^2
 \end{aligned} \tag{3.32}$$

The six fractions from the data are compared with the six fractions from the adjusted Monte Carlo ( $MP$ ) and a  $\chi^2$  fit to yield  $\eta$ ,  $\epsilon_1$  and  $\epsilon_2$  is performed. The inefficiencies are calculated using the following equations:

$$\begin{aligned}
 p_{ineff} = & N_{21M}(1 - (1 - \eta)^2) \\
 & +N_{22M}(1 - (1 - \eta)^2) \\
 & +N_{31M}(1 - (1 - \eta)^3 - 3\eta(1 - \eta)^2) \\
 & +N_{32M}(1 - (1 - \eta)^3 - 3\eta(1 - \eta)^2)
 \end{aligned}$$

$$\begin{aligned}
P_{\text{ineff}} &= p_{\text{ineff}}/(N_{21M} + N_{22M} + N_{31M} + N_{32M}) \\
z_{\text{ineff}} &= N_{21M}(1 - (1 - \epsilon_1)) \\
&\quad + N_{22M}(1 - (1 - \epsilon_2)^2 - 2\epsilon_2(1 - \epsilon_2)) \\
&\quad + N_{31M}(1 - (1 - \epsilon_1)) \\
&\quad + N_{32M}(1 - (1 - \epsilon_2)^2 - 2\epsilon_2(1 - \epsilon_2)) \\
Z_{\text{ineff}} &= z_{\text{ineff}}/(N_{21M} + N_{22M} + N_{31M} + N_{32M}) \\
t_{\text{ineff}} &= N_{21M}(1 - (1 - \eta)^2(1 - \epsilon_1)) \\
&\quad + N_{22M}(1 - (1 - \eta)^2(1 - \epsilon_2)^2 - 2(1 - \eta)^2\epsilon_2(1 - \epsilon_2)) \\
&\quad + N_{31M}(1 - (1 - \eta)^3(1 - \epsilon_1) - 3\eta(1 - \eta)^2(1 - \epsilon_1)) \\
&\quad + N_{32M}(1 - (1 - \eta)^3(1 - \epsilon_2)^2 - 6\eta(1 - \eta)^2\epsilon_2(1 - \epsilon_2) \\
&\quad\quad - 3\eta(1 - \eta)^2(1 - \epsilon_2)^2 - 2(1 - \eta)^3\epsilon_2(1 - \epsilon_2)) \\
T_{\text{ineff}} &= t_{\text{ineff}}/(N_{21M} + N_{22M} + N_{31M} + N_{32M}) \tag{3.33}
\end{aligned}$$

By using the method as described above, the total and partial inefficiencies for 1990, 1991 and 1992 are tabulated in table 3.2. As the momentum decreases the fraction of

	1990	1991	1992
$P_{\text{ineff}}$	$3.7 \pm 0.3 \%$	$2.3 \pm 0.2 \%$	$4.0 \pm 0.2 \%$
$Z_{\text{ineff}}$	$2.1 \pm 0.2 \%$	$1.9 \pm 0.1 \%$	$2.6 \pm 0.1 \%$
$T_{\text{ineff}}$	$5.7 \pm 0.3 \%$	$4.1 \pm 0.2 \%$	$6.4 \pm 0.2 \%$

Table 3.2: *Estimating the inefficiency of the 1990, 1991 and 1992 inclusive muon sample with a 3 GeV lower momentum cut.*

doublets and the fraction of 1 Z segment tracks rise. This is due to the fact that a low momentum triplet can become a doublet because the track will curve outside the sensitive volume. Therefore, the inefficiencies, higher for doublets and 1 Z tracks, rise as well with decreasing momentum. Table 3.3 shows the momentum dependence of the inefficiencies for 1990, 1991 and 1992 data taking period. In order to check the momentum dependence prediction of this method, it is also applied to the  $Z^0 \rightarrow \mu^+\mu^-(\gamma)$  data sample. This result is in perfect agreement with the lower momentum muons, as can be seen in table 3.3, and with results obtained by other methods on this sample [41]. Comparing these results, when possible, with the other methods mentioned yields a good agreement. The sum of the statistical and systematic error is estimated to be 1.0%.

The numbers obtained in this and the previous section will be used in the systematic error studies of the forthcoming analysis chapters.

Total Inefficiency (%)					
	3 – 4 GeV	4 – 8 GeV	8 – 12 GeV	> 12 GeV	45 GeV
1990	$8.1 \pm 1.0$	$5.4 \pm 0.6$	$4.3 \pm 0.8$	$4.4 \pm 0.8$	$4.2 \pm 0.2$
1991	$5.5 \pm 0.6$	$4.1 \pm 0.3$	$3.5 \pm 0.5$	$3.0 \pm 0.4$	$3.2 \pm 0.2$
1992	$8.2 \pm 0.6$	$6.8 \pm 0.3$	$5.1 \pm 0.4$	$4.9 \pm 0.4$	$4.9 \pm 0.1$

Table 3.3: The total inefficiency of the 1990, 1991 and 1992 inclusive muon sample as a function of the muon momentum. For comparison, the last column lists the inefficiencies found using the  $Z^0 \rightarrow \mu^+ \mu^- (\gamma)$  data sample.

# Chapter 4

## Heavy flavour production

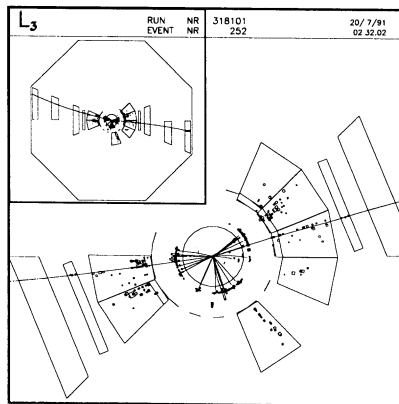


Figure 4.13: An example of an atypical inclusive muon event.

## 4.1 Motivation

The main motivation to study heavy flavour production at the  $Z^0$  resonance is to investigate the Standard Model of electroweak interactions. In figure 4.1 the Feynman diagrams for the first order electroweak processes  $e^+e^- \rightarrow c\bar{c}$  and  $e^+e^- \rightarrow b\bar{b}$  are shown. As the

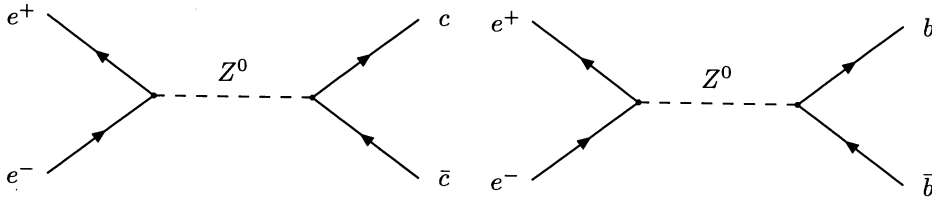


Figure 4.1: First order Feynman diagrams corresponding to the reactions  $e^+e^- \rightarrow c\bar{c}$  and  $e^+e^- \rightarrow b\bar{b}$ .

physical parameters obtained from heavy flavour physics should be the same as the ones obtained from other physics channels, e.g.  $Z^0 \rightarrow \ell^+\ell^- (\gamma)$ , this results in a consistency test of the Standard Model of electroweak interactions.

At LEP energies the huge increase in the cross sections for  $e^+e^- \rightarrow q\bar{q}$ , displayed in the left plot of figure 4.2, opens the possibility to perform detailed high statistics research.

As described in chapter 1, the physics related to the  $b$  quark is potentially interesting and therefore emphasis is put on the study of the bottom quark. As will be explained in section 4.2, the main background of  $e^+e^- \rightarrow b\bar{b}$  events are  $e^+e^- \rightarrow c\bar{c}$  events and at LEP energies the signal to background ratio is relatively large. Let  $R$  be the ratio of the cross sections of these two channels:

$$R = \frac{\sigma(e^+e^- \rightarrow b\bar{b})}{\sigma(e^+e^- \rightarrow c\bar{c})}$$

The Standard Model gives the following prediction if the centre of mass energy is below the  $Z^0$  resonance, where the photon exchange dominates (see equation 1.4):

$$\sigma(e^+e^- \rightarrow q\bar{q}) \sim Q_q^2$$

and so, together with table 1.1, one gets:

$$R \approx \frac{Q_b^2}{Q_c^2} = 0.25$$

On the  $Z^0$  resonance the cross sections change dramatically (see figure 4.2) and become proportional to the sum of the squared vector and axial vector coupling constants (see equation 1.7):

$$\sigma(e^+e^- \rightarrow q\bar{q}) \sim v_q^2 + a_q^2$$



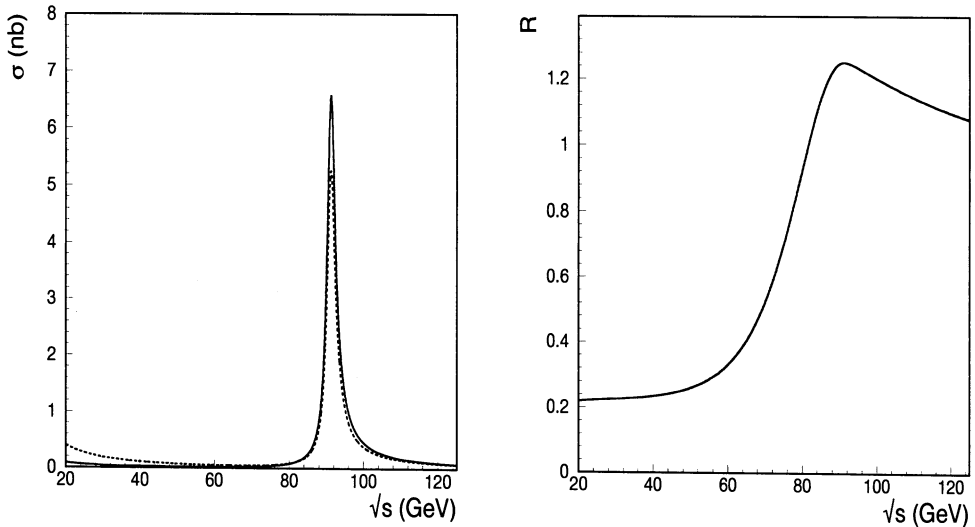


Figure 4.2: The left plot shows the cross section for  $e^+e^- \rightarrow b\bar{b}$  (solid line) and for  $e^+e^- \rightarrow c\bar{c}$  (dashed line) as a function of the centre of mass energy  $\sqrt{s}$ . The right plot shows the ratio  $R$  of the two cross sections as a function of the centre of mass energy  $\sqrt{s}$ .

From equation 1.2 and table 1.1 one gets:

$$v_b^2 \approx 0.50 \quad a_b^2 = 1$$

$$v_c^2 \approx 0.17 \quad a_c^2 = 1$$

with  $v_q$  the neutral current vector coupling constant and  $a_q$  the neutral current axial vector coupling constant between the  $Z^0$  and quark  $q$ . This implies:

$$R = \frac{\sigma(e^+e^- \rightarrow b\bar{b})}{\sigma(e^+e^- \rightarrow c\bar{c})} \approx 1.3$$

and now a much more favourable situation occurs.

Another motivation to study heavy flavour physics is the following one. The forward backward asymmetry at the  $Z^0$  resonance is described by the Standard Model as (see equation 1.19):

$$A_{f\bar{f}} = \frac{3}{4} A_e A_f \quad (4.1)$$

Figure 4.3 shows the quantities  $A_f$  (left) and  $A_{f\bar{f}}$  (right) for muons,  $c$  and  $b$  quarks. From equation 4.1 and figure 4.3 we can see that  $A_{b\bar{b}}$  is more sensitive to  $\sin^2 \theta_W$ , a fundamental parameter of the Standard Model (see equation 1.3), than  $A_{\mu\mu}$ . This implies that with the same error on the forward backward asymmetry it is possible to extract a more accurate measurement of  $\sin^2 \theta_W$  from  $B$  physics than from lepton physics.

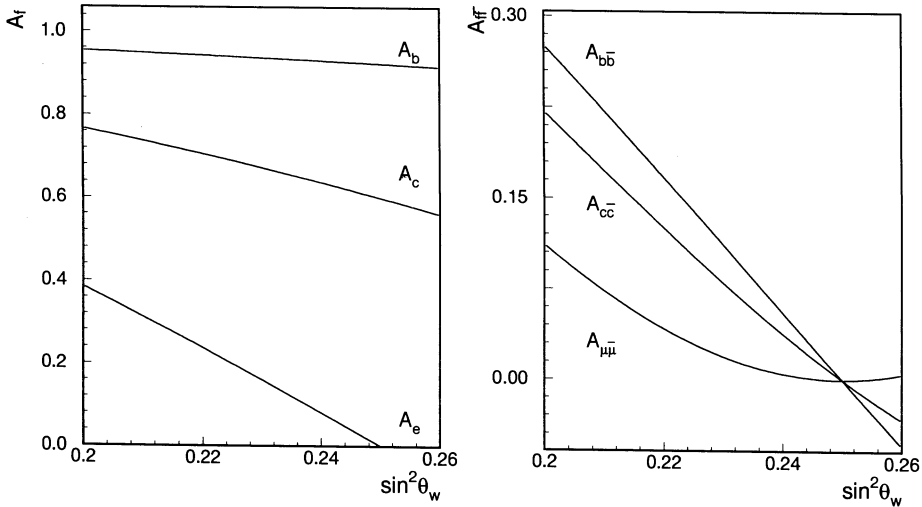


Figure 4.3: The quantities  $A_f$  (left) and  $A_{f\bar{f}}$  (right) for quarks and leptons as a function of the weak mixing angle  $\sin^2 \theta_w$ .

## 4.2 Selection of $b\bar{b}$ events

In order to select one particular type of event, in this case  $Z^0 \rightarrow b\bar{b}$ , specific properties of these events have to be known. First of all, it can be seen as a special case of the more general hadron sample,  $Z^0 \rightarrow q\bar{q}$ , with quark type  $q = b$ . Therefore it is only natural to start the  $b\bar{b}$  selection from this hadron sample. To discriminate the  $b$  quark from the lighter quarks, specific properties of this quark have to be exploited.

It is possible to tag a  $b$  quark through its semileptonic decay into a muon (see figure 4.4). Since about 12% of all  $b$  quarks decay into a muon, 23% of all  $b\bar{b}$  events contain at least one  $b$  quark that decays into a muon. Unfortunately, the  $c$  quark can decay semileptonically as well and kaons and pions, produced in a jet, can also decay into a muon. Finally, hadrons sometimes penetrate into the muon chambers and can therefore be mistaken for a muon, the so-called punch-through. As a consequence, by simply selecting all hadronic events that contain at least one muon, a very contaminated  $b\bar{b}$  sample (see table 4.3) is obtained. Fortunately, the fact that the  $b$  quark is relatively heavy ( $\approx 5$  GeV), makes discrimination between the  $b$  quark and the lighter quarks possible for the following reasons.

1. The mass difference between the  $B$  and the  $D$  meson is large and as a consequence the muon that is created semileptonically will have on average a high momentum in the rest frame of the  $B$  meson. In the laboratory system this gives a large momentum component perpendicular to the  $b$  quark direction (approximated by the jet axis),  $p_t$ , as is shown schematically in figure 4.5.

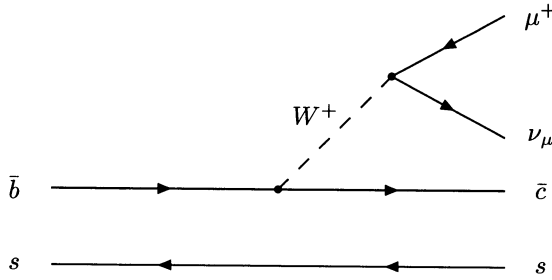


Figure 4.4: The Feynman diagram corresponding to the Spectator Model semileptonic decay of a  $B_s^0$  meson into a  $D_s^-$  meson. The  $s$  quark is the so-called spectator (see chapter 1).

- The  $b$  quark has a hard fragmentation, which means that the  $B$ -hadron formed during the fragmentation process (see section 1.6), will get most of the energy of the  $b$  quark. This implies that the muon originating from this  $B$ -hadron will have a relatively high momentum.

Based on these two properties, an enriched  $b\bar{b}$  sample can be obtained by requiring high  $p$ ,  $p_t$  muons. The  $c$  quark, with its lower mass ( $\approx 1.8$  GeV) and softer fragmentation, produces muons with lower  $p$  and  $p_t$  but nevertheless still higher than those of muons from the decays of hadrons containing only lighter quarks.

The  $p_t$  of the muon is calculated with respect to the nearest jet within a cone of  $90^\circ$  half opening angle around the muon. The jets are reconstructed using the Asjt algorithm, see section 2.10.3. The muon is excluded from the jet and the jet should at least contain 6 GeV. A more elaborate study on this definition of  $p_t$  can be found in reference [59].

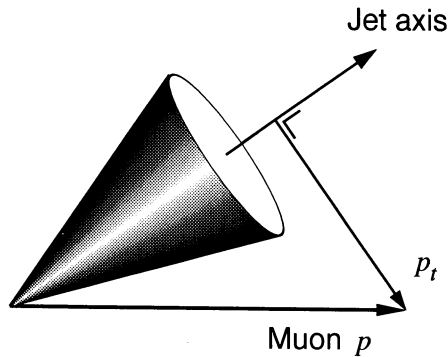


Figure 4.5: Definition of the transverse momentum,  $p_t$ , the momentum component perpendicular to the jet axis.

### 4.3 Trigger efficiency and data handling

Inclusive muon events are triggered by several independent triggers. The primary trigger is the energy trigger which requires at least 15 GeV in the electromagnetic and hadron calorimeters. A second trigger, the single muon trigger, requires one of sixteen barrel scintillator counters in coincidence with a track in the muon chambers. These triggers, combined with an independent charged track trigger and a barrel scintillator counter trigger, give a trigger efficiency larger than 99.99% for hadronic events containing one or more muons. The efficiency of each of the four triggers is calculated by comparing the coincidence rates with the other three triggers. The result of this exercise is shown in table 4.1. As

Trigger	Combined with	Efficiency
Energy	Scintillator	$99.90 \pm 0.02\%$
	TEC	$99.96 \pm 0.01\%$
	Muon	$99.59 \pm 0.05\%$
Scintillator	Energy	$95.11 \pm 0.15\%$
	TEC	$95.14 \pm 0.15\%$
	Muon	$94.54 \pm 0.17\%$
TEC	Energy	$96.03 \pm 0.13\%$
	Scintillator	$96.05 \pm 0.14\%$
	Muon	$95.64 \pm 0.15\%$
Muon	Energy	$84.82 \pm 0.26\%$
	Scintillator	$84.62 \pm 0.27\%$
	Tec	$84.78 \pm 0.27\%$

Table 4.1: *Trigger efficiencies for inclusive muon events.*

the numbers between different combinations agree well, the triggers can be assumed to be independent. The inclusive muon trigger inefficiency is then estimated by taking the product of the four largest trigger inefficiencies, which results in  $(0 \pm 4)10^{-5}$ . The trigger efficiency, one minus this number, is then larger than 99.99%. For more details on these triggers, see chapter 2 section 2.9.

The data for this analysis is obtained in the following way. The events are selected by the PASS 1 hadronic selection criteria (see figure 2.15). This PASS1 selection is an OR combination of relaxed versions of the selection criteria described in section 4.5. All events that survive these cuts are written on disk in DSU format. These DSU files are then analysed and all events that contain either an inclusive electron candidate or an inclusive muon candidate are written on special inclusive lepton DSU files, called LXDSU files.

The Monte Carlo events are selected in a slightly different fashion. Only five flavour

quark production is simulated and all events that contain either an inclusive electron or muon candidate, are selected and written to LXDSU files. All events that contain a generated inclusive lepton, which has not been reconstructed, are saved as well, to be able to calculate the inclusive lepton acceptances. The analysis is performed on these LXDSU files.

## 4.4 Monte Carlo simulation and classification

A Monte Carlo study is performed to predict the  $b\bar{b}$  contents as a function of the applied selection criteria. Approximately one million events were generated by the Lund parton shower programme JETSET 7.2 [60] which is tuned to represent the  $L_3$  hadronic data [26]. Colour string fragmentation is used and the fragmentation of the heavy quarks is described by the Peterson fragmentation function (see section 1.6). The  $b$ -quark and  $c$ -quark fragmentation were adjusted to match the  $L_3$  inclusive muon 1989 and 1990 data [61, 62] in agreement with the extrapolations from lower centre of mass  $e^+e^-$  experiments [31]. The Monte Carlo used does not include  $B^0\bar{B}^0$  mixing. The generated events were fully simulated with SIGEL3 and reconstructed by REGEL3. Average semileptonic branching ratios, measured by  $L_3$ [62] and other experiments [63], are used:

- $\text{Br}(b \rightarrow \mu + X) = (11.7 \pm 0.6)\%$
- $\text{Br}(c \rightarrow \mu + X) = (9.6 \pm 0.6)\%$

The branching ratios of the cascades  $b \rightarrow c \rightarrow \mu$  and  $b \rightarrow \bar{c} \rightarrow \mu$  are factorised as  $\text{Br}(b \rightarrow c/\bar{c}) \cdot \text{Br}(c \rightarrow \mu)$ . Therefore, for the systematic error studies in the forthcoming chapters, the  $c \rightarrow \mu$  branching ratio error has been increased to 1.2% to allow for uncertainties in the  $b \rightarrow \bar{c} \rightarrow \mu$  branching ratio (see figure 4.6), as well as for a possible different mixture of  $D^\pm$  and  $D^0$  mesons in  $b$  quark decays.

The lepton spectra, coming from the  $\Upsilon(4S)$  data obtained by ARGUS and CLEO, show that approximately 20 to 30% of all  $B$  hadrons, decaying semileptonically into a  $D$  meson, produce a high mass  $D$  state, called  $D^{**}$ :  $B \rightarrow D^{**}\ell\nu$ .  $D^{**}$  is the generic name for resonances with  $J^{PC} = \{0^{-+}, 1^{--}, 1^{+-}, 1^{++}, 2^{++}\}$ . The recent ARGUS measurement [64] of  $\text{Br}(\bar{B} \rightarrow D^{**}\ell^-\bar{\nu})$  of  $(2.3 \pm 0.6 \pm 0.4)\%$  or  $(2.7 \pm 0.5 \pm 0.5)\%$ , depending on the Monte Carlo model used, indicates a  $D^{**}$  abundance of  $(20 \pm 6)\%$  and  $(23 \pm 6)\%$  respectively. Other studies [65, 66] seem to indicate an abundance of about 32%, whereas the theoretical prediction using the ISGW model is about 11%[67]. Due to the large mass difference between the  $D^{**}$  and the lower mass  $D$  states ( $\approx 400 - 600$  MeV) its presence yields a softer inclusive lepton spectrum. Hence, the uncertainty of this abundance gives an uncertainty on the inclusive muon spectrum and is therefore a possible source of systematic error. From the above numbers, a  $D^{**}$  abundance of  $(22 \pm 7)\%$  is estimated and used in the Monte Carlo.

Monte Carlo events with inclusive muons are classified into eight categories<sup>1</sup>:

- 1: prompt  $b \rightarrow \mu$

<sup>1</sup>The notation  $b \rightarrow \mu$  means the decay of a hadron containing a  $b$  quark into a muon plus its neutrino and anything else. Similarly for  $c \rightarrow \mu$ , etc. Charge conjugate processes are also implied. The notation  $b \not\rightarrow \mu$  means the decay into anything but a muon.

- 2: the cascade  $b \rightarrow c \rightarrow \mu$
- 3: the cascade  $b \rightarrow \tau \rightarrow \mu$
- 4: the cascade  $b \rightarrow \bar{c} \rightarrow \mu$ , explained in figure 4.6
- 5:  $b \rightarrow$  background, containing also  $b \rightarrow J/\psi \rightarrow \mu$
- 6: prompt  $c \rightarrow \mu$
- 7: background muons: e.g. from pions, kaons and muons coming from gluon splitting ( $g \rightarrow b\bar{b}$  with  $b \rightarrow \mu$ )
- 8: background non-muons: punch through.

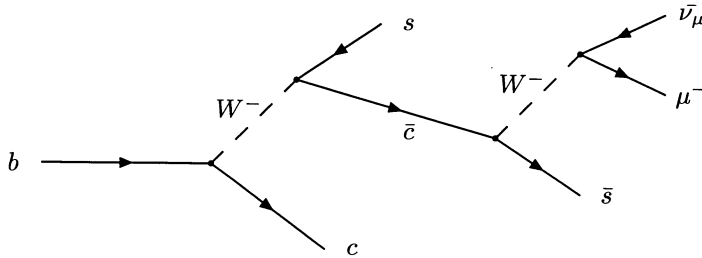


Figure 4.6: The diagram corresponding to cascade decay  $b \rightarrow \bar{c} \rightarrow \mu$ .

This classification will be used frequently in the analyses in the forthcoming chapters.

In order to correct for the effect of the differing resolutions in the data and the Monte Carlo, the resolution of the momentum of the simulated muon and the angle between this muon track and the simulated jet (or thrust) axis are changed by smearing them. The amount by which the momentum and the angle have to be smeared have been obtained in section 3.5 and section 2.4 respectively. The uncertainty of this procedure for the angular smearing is estimated to be 50%. In doing so, the  $p_t$  of the muon is automatically smeared as well.

## 4.5 Selection criteria

Before continuing with the selection of the  $b\bar{b}$  events the selection criteria of the  $Z^0 \rightarrow q\bar{q}$  sample are described (see also [15]). The signature of these events is characterised by an average energy deposition in the detector of about the centre of mass energy of the two beams, a low energy imbalance in three dimensions and a high multiplicity of particles produced in the interaction. An example of such an event is shown in figure 4.13. These properties are therefore used to select  $Z^0 \rightarrow q\bar{q}$  events. After describing the hadron selection, the inclusive muon selection is given, followed by the  $b\bar{b}$  event selection.

### 4.5.1 Hadron selection

#### Energy cut

$0.42\sqrt{s} < E_{\text{vis}} < 1.5\sqrt{s}$ , i.e. the total visible energy has to be in between 0.42 and 1.5 times the centre of mass energy. The total visible energy is defined as the sum of the measured energy deposited in the calorimeters and the energy of the muons as detected by the muon chambers. The lower limit is chosen somewhat lower than the one used for the standard  $Z^0 \rightarrow q\bar{q}$  selection (0.5) to avoid losing events containing high momentum neutrinos. Figure 4.7 shows the visible energy fraction for all selected events. All other

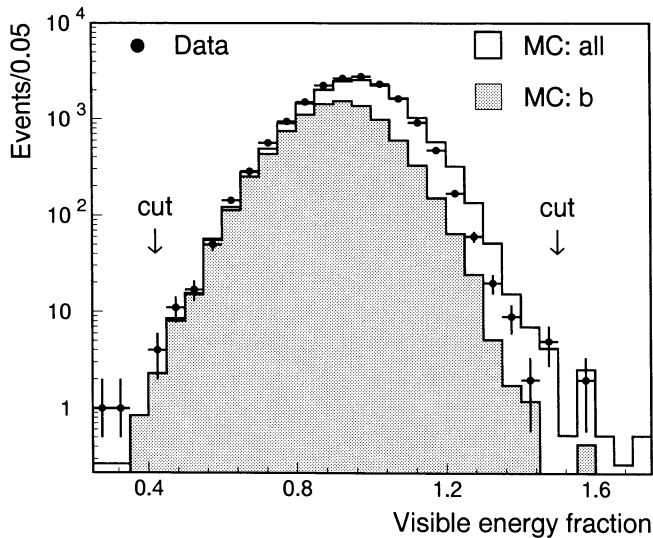


Figure 4.7: Visible energy fraction for selected events. All other cuts have been applied. The hatched area indicates the  $b\bar{b}$  events. The cuts are indicated.

cuts (to be discussed below) have already been applied. The hatched area in the figure indicates contents of  $Z^0 \rightarrow b\bar{b}$  events. The normalisation of the Monte Carlo distributions, as in all plots to come, is done by normalising to the number of selected hadron events. There is good agreement of data and Monte Carlo.

#### Imbalance cut (1)

$|E_{\parallel}| < 0.5E_{\text{vis}}$ , i.e. the missing energy parallel to the beam has to be smaller than 0.5 times the visible energy. The left plot in figure 4.8 shows the distribution for the longitudinal energy imbalance fraction. Again all other cuts have been applied and the cut is indicated. The small excess of data in the tail is due to two photon events [45] and will not cause any systematic error.

**Imbalance cut (2)**

$E_{\perp} < 0.5E_{vis}$ , i.e. a missing energy fraction transverse to the beam smaller than 0.5. The distribution can be seen in the right plot of figure 4.8. The good agreement in the signal region is evident.

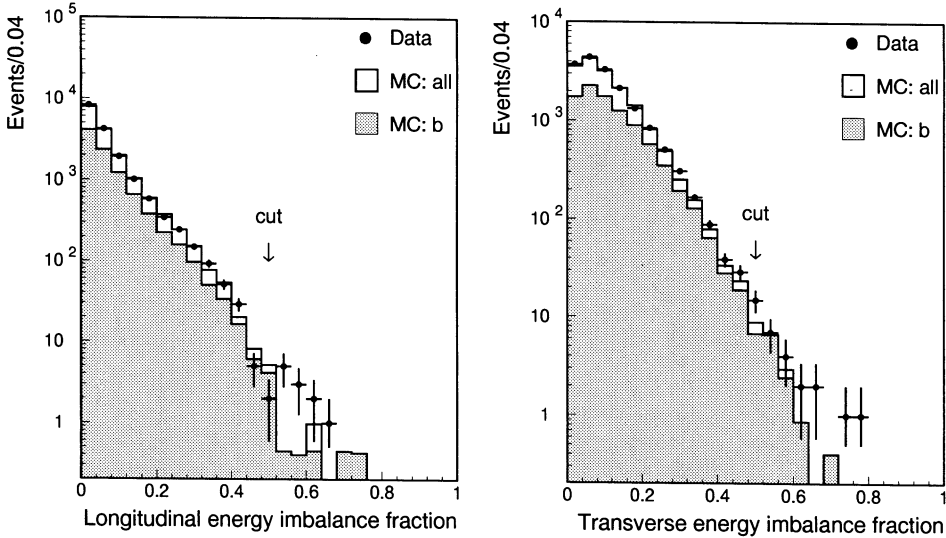


Figure 4.8: Energy imbalance fraction for selected events. All other cuts have been applied. The hatched area indicates the  $b\bar{b}$  events. The cuts are indicated.

**Multiplicity cut:**

The number of ASRC's, the smallest resolvable clusters of energy deposits in the calorimeters (see 2.10.3), has to be large enough to ensure a high multiplicity event, thus removing almost all  $\tau^+\tau^-(\gamma)$  events. The thrust axis is defined as the direction that maximises the projected energy flow. Quantitatively, the direction  $\vec{n}$ , which is called the thrust axis, is chosen to maximise the following expression:

$$\frac{\sum_a |\vec{p}_a \cdot \vec{n}|}{\sum_a |\vec{p}_a|} \tag{4.2}$$

where  $\vec{p}_a$  is the momentum vector of particle  $a$  and the sum runs over all final state particles. The multiplicity cut is then defined as:

Year	Thrust axis in barrel region	Thrust axis in endcap region
1990	$\geq 13$	$\geq 9$
1991	$\geq 14$	$\geq 18$



Due to the fact that the BGO calorimeter endcaps were only installed from the beginning of 1991 these numbers are different for the two data taking periods. Figure 4.9 shows the number of ASRC's in the barrel region (left) and the endcap region (right). All other cuts have been applied. The hatched area indicates the  $Z^0 \rightarrow b\bar{b}$  events. The small peaks left of the cuts are due to  $\tau^+\tau^-(\gamma)$  events. The excess of data on the right side of the distributions is not yet understood. It will, however, not contribute to the systematic error since the cut is not sensitive to this effect.

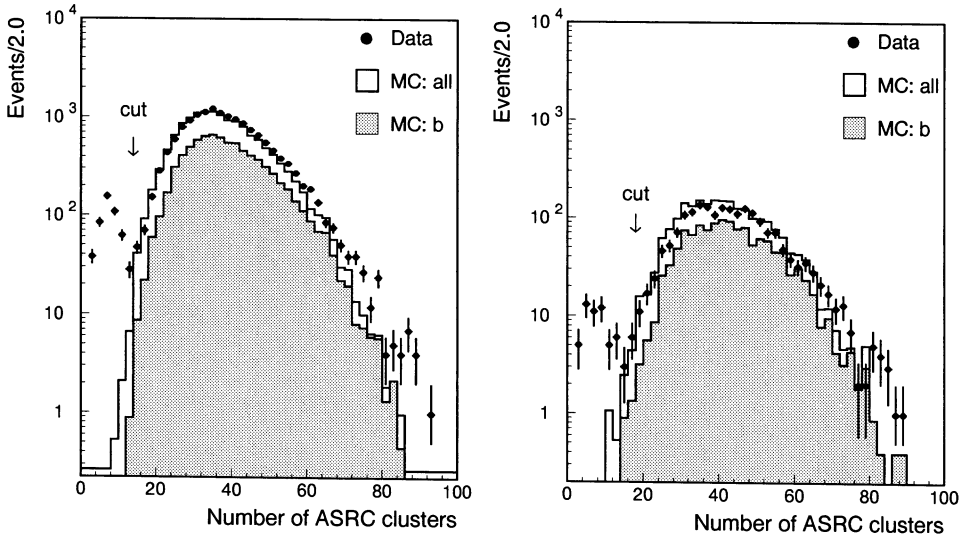


Figure 4.9: The number of ASRC's in the barrel region (left) and the endcap region (right). All other cuts have been applied. The hatched area indicates the  $b\bar{b}$  events. The cuts are indicated. The small peaks left of the cuts are due to  $\tau^+\tau^-(\gamma)$  events.

### 4.5.2 Inclusive muon selection

A particle is identified as a muon if it satisfies all the following conditions.

#### P segment cut

The track has at least 2 (out of 3) segments in the muon P chambers to eliminate spurious tracks and to get a good momentum resolution.

## Z segment cut

The track has at least 1 (out of 2) segments in the muon Z chambers in order to obtain a good angular resolution with respect to the nearest jet.

## Vertex cut

The track has to point to the intersection region in order to reject muons that clearly do not originate from the interaction vertex:

- in the  $(x,y)$  plane the distance to the interaction vertex should be less than  $4\sigma_{xy}$  with a maximum of 200 mm, where  $\sigma_{xy}$  is the error on the position of the track at the interaction region in the  $(x,y)$  plane. The corresponding distribution is plotted in figure 4.10. The inconsistency for small distances is not yet understood but causes no systematic errors.

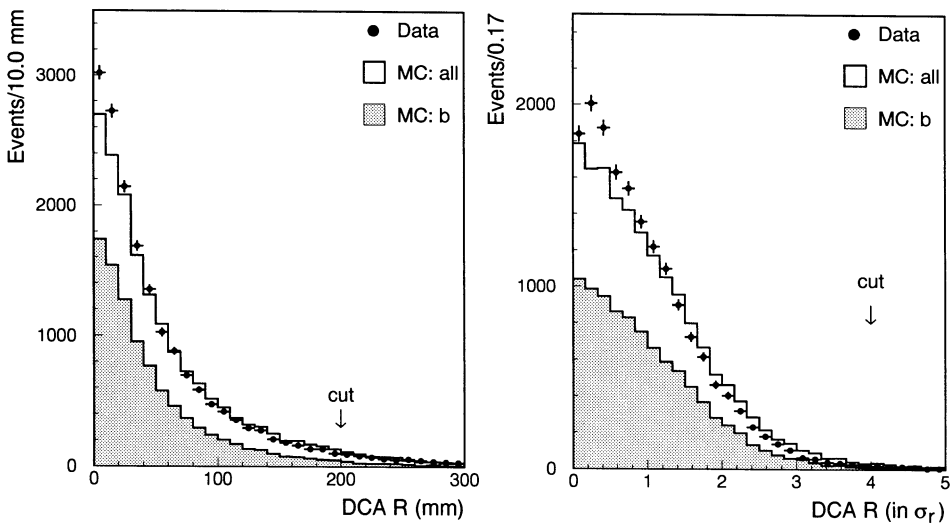


Figure 4.10: The muon vertex distributions in the  $(x,y)$  plane for inclusive muon events compared to the Monte Carlo simulation. The hatched area indicates the  $b\bar{b}$  events.

- in the  $(y,z)$  plane the distance to the interaction vertex should be less than  $4\sigma_{yz}$  with a maximum of 300 mm. The corresponding distribution is plotted in figure 4.11. The inconsistency for small distances is not yet understood but causes no systematic errors.

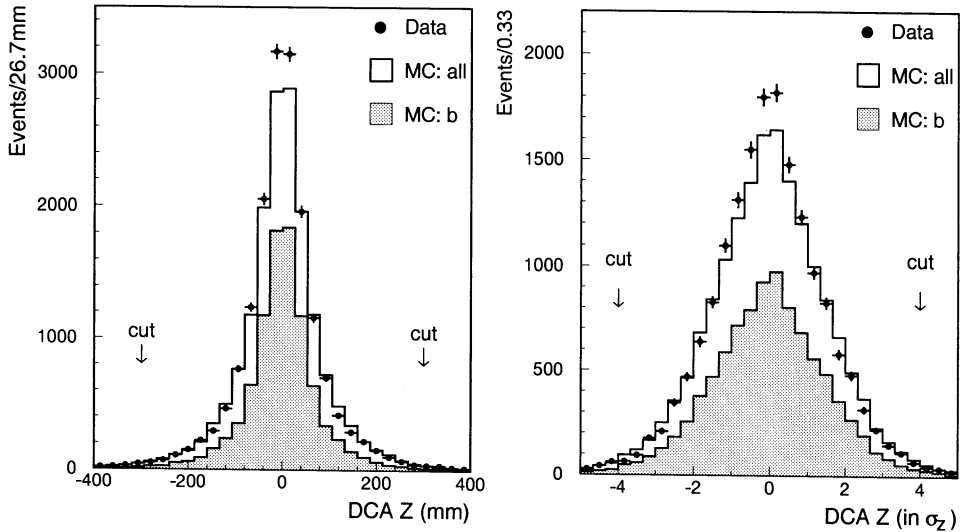


Figure 4.11: The muon vertex distributions in the  $(y,z)$  plane for inclusive muon events compared to the Monte Carlo simulation. The hatched area indicates the  $b\bar{b}$  events.

### 4.5.3 $b\bar{b}$ selection

#### Momentum cut

The track is required to have a momentum between 4 GeV and 30 GeV to reduce background from  $\mu^+\mu^-(\gamma)$  events, cosmic muons and to avoid any reconstruction error. The left plot in figure 4.12 displays the muon momentum distribution for inclusive muon events compared to the Monte Carlo simulation. The hatched area indicates the  $b\bar{b}$  events.

#### Transverse momentum cut

The track has to have a transverse momentum,  $p_t$ , less than 6 GeV to avoid any reconstruction error. The right plot in figure 4.12 shows transverse momentum distribution for inclusive muon events compared to the Monte Carlo simulation. The hatched area indicates the  $b\bar{b}$  events. The inconsistency for the low  $p_t$  is not yet understood.

## 4.6 Background

The contamination from  $e^+e^- \rightarrow \ell^+\ell^-(\gamma)$  processes, with  $\ell = e, \mu$  or  $\tau$ , is estimated by analysing the main background process, i.e.  $\ell = \tau$ . Out of 20,000 simulated  $\tau$  events, generated by KORALZ (see box 2.1), 688 events passed the hadron selection criteria and

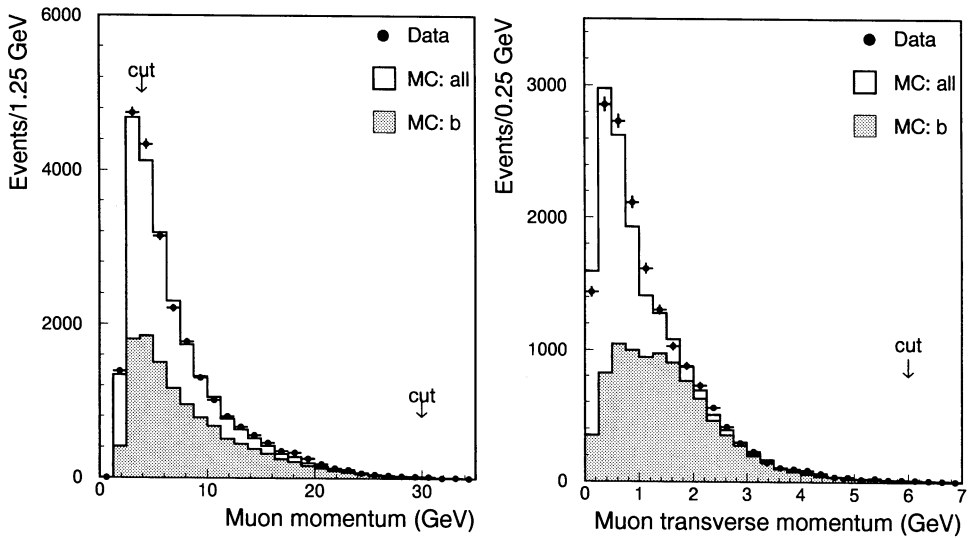


Figure 4.12: The muon momentum distribution (left) and transverse momentum distribution (right) for inclusive muon events compared to the Monte Carlo simulation. The hatched area indicates the  $b\bar{b}$  events.

out of those 6 events passed the inclusive muon selection cuts. Let  $\sigma_{\text{had}}$  and  $\sigma_{\ell\ell}$  be the cross sections for  $Z^0 \rightarrow \text{hadrons}$  and  $Z^0 \rightarrow \ell^+\ell^-(\gamma)$  respectively and let  $A_{\text{incmu}}$  be the acceptance for inclusive muon events and  $A_{\ell\ell}$  the acceptance for background events, then the fraction of background events,  $\rho$ , is calculated by:

$$\rho = \frac{A_{\ell\ell} \sigma_{\ell\ell}}{A_{\text{incmu}} \sigma_{\text{had}}} \quad (4.3)$$

Using this equation, the estimated background from  $e^+e^- \rightarrow \tau^+\tau^-(\gamma)$  equals  $(0.17 \pm 0.01)$  % for hadronic events and  $(0.025 \pm 0.011)$  % for inclusive muon events respectively. The background coming from cosmic ray showers and beam gas or beam wall events were found to be negligible by visually scanning [68] a number of events  $< 0.01\%$ . This implies that these backgrounds, not coming from  $Z^0 \rightarrow q\bar{q}$ , can be neglected.

## 4.7 Final event sample

After applying all the cuts, the total data event sample is known and shown in table 4.2. Table 4.3 shows the results of Monte Carlo studies giving the fraction of each source of muons and background for data samples with no cut on  $p_t$  and with a  $p_t$  cut at 1.00 GeV. From this table, it can clearly be seen that the purity of the  $b\bar{b}$  sample is increased if the muon is required to have a high transverse momentum. Displayed in figure 4.13 is a selected inclusive muon event.

Year	hadrons	$\mu$ + hadrons
1990	114,346	5,833
1991	313,600	16,777
Total	428,006	22,610

Table 4.2: *The data event sample as used for the analysis for the two running periods separately and for the total of these two periods.*

Category	$p_{t\mu} > 0.00$ GeV	$p_{t\mu} > 1.00$ GeV
1: $b \rightarrow \mu$	37.3 %	71.4 %
2: $b \rightarrow c \rightarrow \mu$	10.8 %	6.5 %
3: $b \rightarrow \tau \rightarrow \mu$	1.8 %	1.8 %
4: $b \rightarrow \bar{c} \rightarrow \mu$	1.3 %	0.5 %
5: $b \rightarrow$ background	4.9 %	3.1 %
6: $c \rightarrow \mu$	15.5 %	5.8 %
7: decay	8.5 %	3.2 %
8: punch through	19.9 %	7.7 %
Efficiency	43.0 %	34.6 %

Table 4.3: *Monte Carlo estimates of the fractions of each type of muon in the 1991 data sample and the efficiencies of selecting a prompt  $b \rightarrow \mu + X$  event with these cuts.*

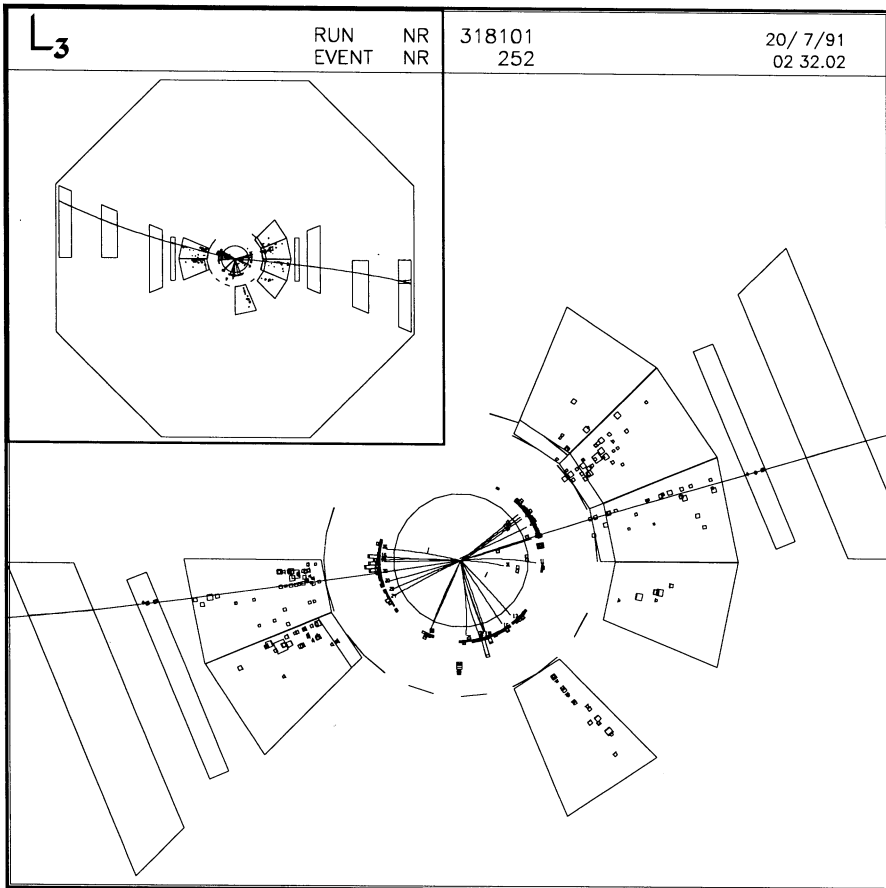


Figure 4.13: An example of an atypical inclusive muon event.

# Chapter 5

## $B^0 \bar{B}^0$ Mixing

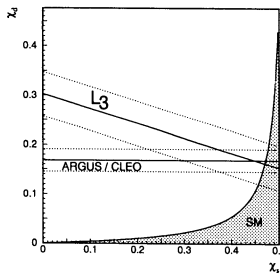


Figure 5.5: A comparison of  $L_3$ 's  $B^0 \bar{B}^0$  mixing result with those from ARGUS and CLEO. Also displayed is the Standard Model (SM) allowed (hatched) region.  $f_d = 0.40$  and  $f_s = 0.12$  is assumed, where  $\chi_B = f_d \chi_d + f_s \chi_s$ . The dashed lines correspond to  $1\sigma$  errors in both cases.

$$\Delta M_s > 3.5 \cdot 10^{-4} \text{ eV at } 90\% \text{ confidence level}$$

Equation 1.27 gives:

$$\left| \frac{V_{td}}{V_{ts}} \right|^2 = \frac{M_{B_d} B_{B_d} f_{B_d}^2 x_d}{M_{B_s} B_{B_s} f_{B_s}^2 x_s} \equiv \xi_d \frac{x_d}{x_s} \quad (5.17)$$

Since the ratio  $\xi_d$  is expected to be close to 1.0, it is assumed that  $\xi_d = 1.0$  and one gets:

$$\left| \frac{V_{td}}{V_{ts}} \right| = 0.57 \pm 0.26 \quad (5.18)$$

As a last item of this chapter, the CP violation in the  $B$  system is investigated. Let  $a_{ll}$  be defined by:

$$a_{ll} \equiv \frac{N^{++} - N^{--}}{N^{++} + N^{--}} \quad (5.19)$$

with  $N^{++}$  and  $N^{--}$  as in section 5.2. It can be shown that for leptons emanating from a  $B_d \bar{B}_d$  or  $B_s \bar{B}_s$  system [73]:

$$a_{ll} \equiv \frac{N_{db}^{++} - N_{db}^{--}}{N_{db}^{++} + N_{db}^{--}} = \frac{|p_d|^2 - |q_d|^2}{|p_d|^2 + |q_d|^2} \quad (5.20)$$

## 5.1 Introduction

An event with two like charge inclusive muons is a signature for  $B^0\bar{B}^0$  mixing since the promptly produced muons propagate the sign of the  $b$  quark contained in the  $B$  meson. Therefore, two high  $p_t$ ,  $p_t$  opposite side same charge muons are a candidate for an event in which a  $B^0\bar{B}^0$  transition took place.

Two methods are used to measure the mixing parameter  $\chi_B$  defined in 1.5. One is based on counting the number of high  $p_t$  dimuon events with the same charge as compared to the number with opposite charge and serves as a cross check for the second method. The second method is based on a four dimensional fit to the complete  $p$  and  $p_t$  spectra of the dimuons which uses the full information of the event. It requires large Monte Carlo statistics to accurately determine the probability functions used by this method.

## 5.2 Selection of dimuon events

By requiring (at least) two muons with an opening angle  $\zeta$  larger than  $60^\circ$  in a hadronic event the data sample, as tabulated in table 5.1, is obtained. Here the superscripts of the capital  $N$  stand for the charges of the two muons.

$p_{t\mu\min}$	$N^{++}$	$N^{--}$	$N^{\pm\pm}$	$N^{\pm\mp}$	Total
0.00 GeV	174	114	288	487	775
1.00 GeV	37	32	69	169	238

Table 5.1: *The dimuon data sample containing the 1990 and 1991 data. The superscripts of the capital  $N$  stand for the charges of the two muons.*

The inclusive dimuon Monte Carlo sample can be divided into eight categories. Table 5.2 shows the Monte Carlo estimates of the fractions of these eight categories of dimuon events in the data sample. The cascade decays  $b \rightarrow \tau \rightarrow \mu$  and  $b \rightarrow \bar{c} \rightarrow \mu$  are contained in the prompt  $b \rightarrow \mu$  defined as category 21 in table 5.2.

Figure 5.1 shows the momentum distribution of the least energetic muon for like sign dimuons (left) and for unlike sign dimuons (right) with  $p_t > 1.0$  GeV. The Monte Carlo sample is normalised to the total number of dimuon events in the data. Since the Monte Carlo contains no  $B^0\bar{B}^0$  mixing, the excess of data dimuon events in the left plot and the lack of them in the right plot is a clear signal for  $B^0\bar{B}^0$  mixing. Figure 5.2 shows the minimum transverse momentum distribution of the two muons for like sign dimuons (left) and for unlike sign dimuons (right) with  $p_t > 1.0$  GeV. Again, the excess of data dimuon events in the left plot and the lack in the right plot is a clear signal for mixing. Figure 5.3 shows a like sign dimuon event in the  $L_3$  detector (left) and an unlike sign dimuon event (right).



Muon Pair Category	$p_{t\mu} > 0.0 \text{ GeV}$	$p_{t\mu} > 1.0 \text{ GeV}$
21: $b \rightarrow \mu, b \rightarrow \mu$	37.7 %	72.8 %
22: $b \rightarrow c \rightarrow \mu, b \rightarrow c \rightarrow \mu$	3.6 %	0.6 %
23: $b \rightarrow \mu, b \rightarrow c \rightarrow \mu$	21.7 %	15.1 %
24: $b \rightarrow \mu, b \rightarrow \text{background}$	11.1 %	6.7 %
25: $b \rightarrow c \rightarrow \mu, b \rightarrow \text{background}$	2.9 %	0.9 %
26: $b \rightarrow \text{background}, b \rightarrow \text{background}$	0.7 %	0.2 %
27: $c \rightarrow \mu, c \rightarrow \mu$	7.3 %	0.7 %
28: others	15.0 %	3.0 %

Table 5.2: Monte Carlo estimates of the fractions of various categories of dimuon events in the 1991 data sample. Since, in the presence of mixing, all charge combinations are possible, the  $\pm$  superscripts on the muons are omitted.

### 5.3 The counting method

In the absence of mixing, as is the case in the Monte Carlo used, like sign dimuon events can in principle only come from category 23 or categories where background is involved. Other categories can only contribute to the true mixing by confusing the charge of one of the muons in the muon detector. From table 5.2 it can be seen that, in the absence of mixing, the fraction of events giving like sign dimuon events is small at high  $p_t$ . Since the charge confusion probability is small as well ( $< 0.5\%$ ), a large fraction of like sign dimuon events in the data is a clear signal for  $B^0\bar{B}^0$  mixing:

$$\frac{N^{\pm\pm}}{N_{\text{tot}}} (\text{Data}) = 0.290 \pm 0.029, \quad \frac{N^{\pm\pm}}{N_{\text{tot}}} (\text{MC}) = 0.198 \pm 0.017 \quad (5.1)$$

If a muon event is of type 21, there is a probability  $\chi_B$  for each muon to flip sign due to the oscillation of its  $B$  meson parent. This means that the probability to end up with two like sign muons is the product of the probabilities of one muon flipping sign while the other does not and vice versa:  $2\chi_B(1 - \chi_B)$ . For each category the same reasoning is applied. Equation 5.2 shows how the mixing parameter,  $\chi_B$ , can be obtained from the fraction of like sign dimuon events.

$$\begin{aligned} \frac{N^{\pm\pm}}{N_{\text{tot}}} = & (f_{21} + f_{22}) \cdot 2\chi_B(1 - \chi_B) \\ & + f_{23} \cdot [(1 - \chi_B)^2 + \chi_B^2] \\ & + f_{24} \cdot [\chi_B(1 - \chi_5) + \chi_5(1 - \chi_B)] \\ & + f_{25} \cdot [(1 - \chi_B)(1 - \chi_5) + \chi_B\chi_5] \\ & + f_{26} \cdot 2\chi_5(1 - \chi_5) \\ & + f_{28} \cdot P^{\pm\pm} \end{aligned} \quad (5.2)$$

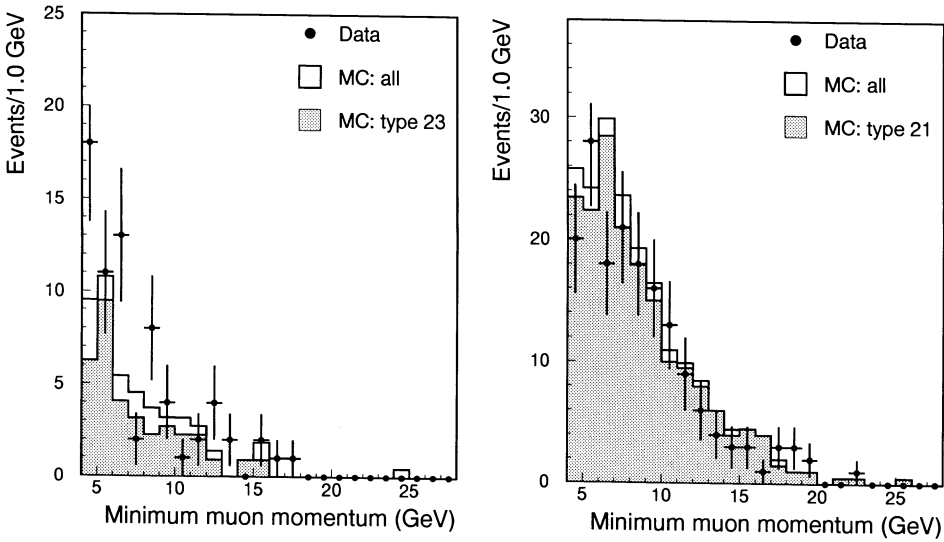


Figure 5.1: The distribution of the minimum of the two momenta for like sign muons (left) and for unlike sign dimuons (right) compared to the Monte Carlo distribution without mixing and with  $p_t > 1.0$  GeV.

In this equation  $\chi_5$ , the effective mixing parameter for events of type 5, see table 4.3, is defined as follows:

$$\chi_5 = (1 - \chi_B)(1 - c) + \chi_B c \quad (5.3)$$

in which  $c$  is the probability that a  $b(\bar{b})$  quark will decay via some cascade (not  $b \rightarrow c \rightarrow \mu$ ,  $b \rightarrow \bar{c} \rightarrow \mu$  or  $b \rightarrow \tau \rightarrow \mu$ ) into a negative (positive) particle which is detected as a muon by the muon chambers. This implies that if  $c$  does not equal 0.5 information about the oscillation of the  $B$  meson is contained in the charge of the particle detected by the muon chambers.  $P^{\pm\pm}$  is the probability to detect two like sign background particles in the muon chamber, which do not originate from a  $b$  quark (category 28). From the Monte Carlo analysis we derive:

$$c = 0.63 \pm 0.02 \quad (5.4)$$

and

$$P^{\pm\pm} = 0.54 \pm 0.02 \quad (5.5)$$

Solving equation 5.2 for  $\chi_B$ , using table 5.2 the following result has been obtained for  $p_{t\mu} \geq 1.0$  GeV:

$$\chi_B = 0.090 \pm 0.029 \quad (5.6)$$

where the error is statistical only.

By varying all known quantities that could contribute to the systematic error in the measurement of  $\chi_B$  by their measured or estimated error, the systematic error on  $\chi_B$  is estimated.

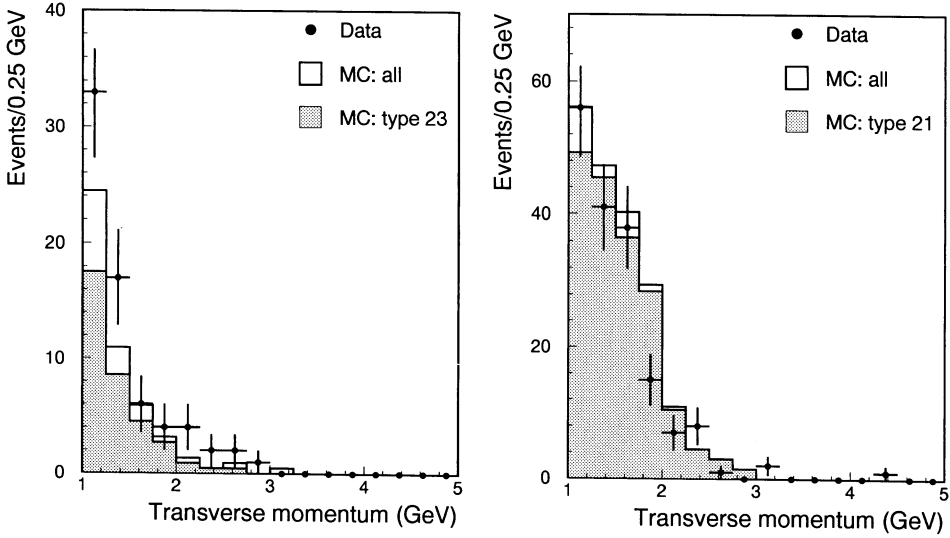


Figure 5.2: The distribution of the minimum of the two transverse momenta for like sign muons (left) and for unlike sign dimuons (right) compared to the Monte Carlo distribution without mixing and with  $p_t > 1.0$  GeV.

First, all known quantities that have a measured error are varied by this error (or in case of  $\text{Br}(c \rightarrow \mu + X)$  by two times this error as explained in section 4.4). Next, the influence of the minimum  $p_t$  cut is investigated. Figure 5.4 shows  $\chi_B/\chi_B^0$  as a function of the minimum  $p_t$  with  $\chi_B^0$  the nominal value for a minimum  $p_t$  of 1.0 GeV:  $\chi_B^0 = 0.090$ . This plot takes the relative change in statistics into account: for each  $p_t$  cut other than 1.0 GeV, the relative change in  $N^{\pm\pm}$  and  $N_{\text{tot}}$  is calculated:  $\Delta N^{\pm\pm}$  and  $\Delta N_{\text{tot}}$ . Using the same Monte Carlo fractions  $f_i$  and  $N_{\text{tot}}$  but  $N^{\pm\pm} \pm \sigma(\Delta N^{\pm\pm})$  instead of  $N^{\pm\pm}$ , with

$$\sigma(\Delta N^{\pm\pm}) = \sqrt{\Delta N_{\text{tot}} t(1-t)} \quad (5.7)$$

with

$$t = \frac{\Delta N^{\pm\pm}}{\Delta N_{\text{tot}}} \quad (5.8)$$

the change in  $\chi_B$  is calculated. Applying this procedure to all points and normalising them to  $\chi_B^0$  results in the plot. As all variations in  $\chi_B/\chi_B^0$  are statistically consistent, no systematic error due to this minimum  $p_t$  cut is assigned.

Changing the definition of opening angle  $\zeta$  also changes the number of accepted events and therefore this requirement has to be studied in a similar way as is done for the minimum  $p_t$  cut. While the number of data events hardly changes by redefining  $\zeta$ , the Monte Carlo fractions  $f_i$  do change slightly, causing a small variation in  $\chi_B$  which cannot be statistically accounted for by the change in the number of data events. Therefore, a systematic error is estimated of  $\pm 0.002$ .

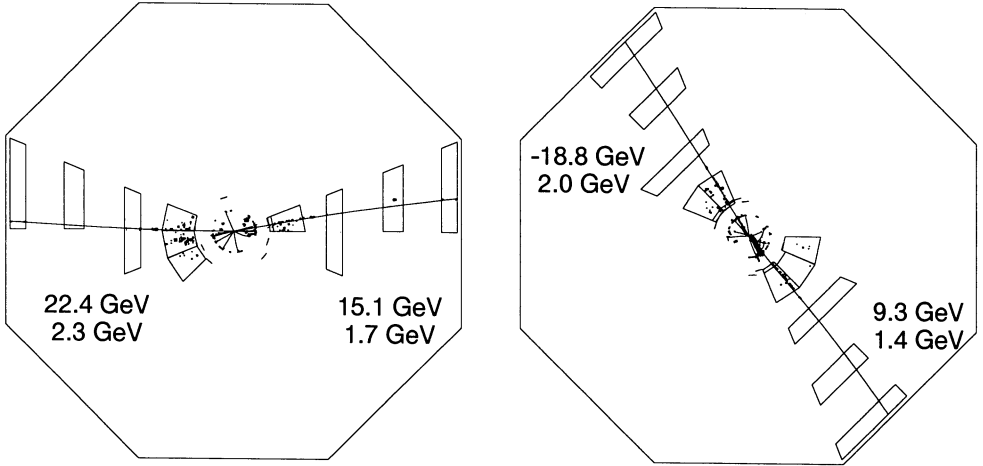


Figure 5.3: Two inclusive dimuon events in the  $L_3$  detector; like sign (left) and unlike sign (right). The two numbers assigned to each muon are  $Q_\mu p_\mu$  and  $p_{t\mu}$  respectively.

The uncertainty on the background fraction predicted by the Monte Carlo is estimated by varying this fraction in the  $p_t$  spectrum of single muons with 85% and 115% of the Monte Carlo background. This covers the allowed variation of the background fraction and the change in  $\chi_B$  due to this uncertainty is  $\pm 0.002$ .

As explained in section 4.4, the difference in muon momentum resolution and jet angular resolution between data and Monte Carlo causes a difference in the muon  $p_t$  resolution between data and Monte Carlo. In order to study the systematic influence on  $\chi_B$  of this effect, the Monte Carlo muon momentum and angle between muon and accompanying jet are smeared. The change in  $\chi_B$  is  $\pm 0.001$ .

The charge confusion for muons is estimated to be  $(0.2 \pm 0.2)\%$  from a study of the  $Z^0 \rightarrow \tau^+\tau^-$  events [58] where a  $\tau$  decays into a muon. As the average muon momentum for muons coming from  $\tau$  decay is higher than the average muon momentum for inclusive muons, this is a conservative estimate. This value is also consistent with the study of  $Z^0 \rightarrow \mu^+\mu^-$  events, yielding 0.3%[41]. The measurement of  $\chi_B$  is corrected for this effect and its error corresponds to changes in  $\chi_B$  by  $\pm 0.002$ .

The effect on  $\chi_B$  of the uncertainty in the  $D^{**}$  abundance (see section 4.4) is studied by varying this abundance in the range  $(22 \pm 7)\%$ . The measurement of  $\chi_B$  changes less than 0.001 and therefore no systematic error has been assigned.

Finally the influence of the limited number of Monte Carlo events on the knowledge of the fractions  $f_i$  is calculated to give an additional uncertainty of  $\pm 0.008$  on  $\chi_B$ . Table 5.3 summarises this systematic error study. The biggest contribution to the total systematic error, being the Monte Carlo statistics, can only be reduced by producing even more Monte Carlo events in the future. Although the errors arising from the two branching ratios  $\text{Br}(b \rightarrow$

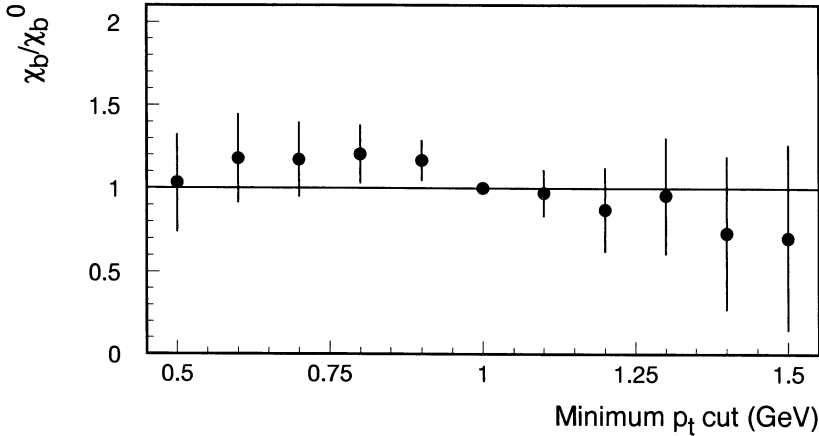


Figure 5.4: The variation in  $\chi_B/\chi_B^0$  as a function of the minimum  $p_t$ .

$\mu + X$ ) and  $\text{Br}(c \rightarrow \mu + X)$  are among the three largest contributions, no effort has been put in reducing them since the value for  $\chi_B$  obtained in this section is only to be used as a cross check for the method described in the following section.

## 5.4 The four dimensional unbinned likelihood fit

In stead of the straight forward calculation of the mixing parameter  $\chi_B$  as demonstrated above, an event by event unbinned maximum likelihood method is applied to the complete  $p$  and  $p_t$  spectra of the selected dimuon events. Unbinned indicates that a likelihood is calculated for each data event separately contrary to calculating one likelihood for several data events contained in one bin, i.e. a four dimensional box in  $(p_1, p_{t1}, p_2, p_{t2})$  space.

The likelihood function is defined as

$$\mathcal{L} = \prod_{i=1}^N f(i) \quad \text{with} \quad f(i) = \frac{1}{M \cdot V_{\text{box}}(i)} \sum_{k,l} N_{k,l}(i) W_{k,l}(i) \quad (5.9)$$

in which  $f(i)$  is the probability density and  $N_{k,l}$  is the number of Monte Carlo dimuon events of type  $(k,l)$  found in the volume of the four dimensional box  $V_{\text{box}}(i)$  around data point  $i$ .  $N(M)$  is the total number of data (Monte Carlo) events selected as dimuons.  $M$  is normalised by multiplying it with the ratio of the number of selected data hadron events and the number of selected Monte Carlo hadron events.  $W_{k,l}(i)$ , the weighting function, is defined as follows:

$$W_{k,l}(i) = \begin{cases} (1 - \chi_k)(1 - \chi_l) + \chi_k \chi_l & \text{for } (q_1 q_2)^{\text{Data}} = (q_1 q_2)^{\text{Monte Carlo}} \\ (1 - \chi_k) \chi_l + (1 - \chi_l) \chi_k & \text{for } (q_1 q_2)^{\text{Data}} \neq (q_1 q_2)^{\text{Monte Carlo}} \end{cases} \quad (5.10)$$

Contribution	$\Delta\chi_B$
$c = 0.63 \pm 0.02$	0.001
$P^{\pm\pm} = 0.54 \pm 0.05$	0.001
Changing the definition of opposite side from $45^\circ$ to $90^\circ$	0.002
$\text{Br}(b \rightarrow \mu + X) = 0.117 \pm 0.006$	0.005
$\text{Br}(c \rightarrow \mu + X) = 0.096 \pm 0.012$	0.005
Variation of the background fraction by $\pm 15\%$	0.002
Smearing of the muon momentum by $\Delta p/p = \Delta_\alpha \pm 30\%$ and smearing of the angle between the muon and the nearest jet by $(0.6 \pm 0.3)^\circ$	0.001
Changing the fragmentation parameter $\varepsilon_b = 0.050 \pm 0.006$ and changing the fragmentation parameter $\varepsilon_c = 0.5 \pm 0.1$	0.002
Charge confusion: $(0.2 \pm 0.2)\%$	0.002
Monte Carlo statistics	0.008
Total systematic error in $\chi_B$	0.012

Table 5.3: The various contributions to the systematic error of  $\chi_B$  as derived by the counting method.

Category $k$	$\chi_k$
1: $b \rightarrow \mu$	$\chi_B$
2: $b \rightarrow c \rightarrow \mu$	$\chi_B$
3: $b \rightarrow \tau \rightarrow \mu$	$\chi_B$
4: $b \rightarrow \bar{c} \rightarrow \mu$	$\chi_B$
5: $b \rightarrow$ background	$\chi_5$
6: $c \rightarrow \mu$	0
7: decay	0
8: punch through	0

Table 5.4: The amount of mixing used in the fit method for each category.

The amount of mixing,  $\chi_k$ , for category  $k$  is given in table 5.4 in which  $\chi_5$  is defined as before (equation 5.3). The two cases in the definition of  $W_{k,l}(i)$  reflect the two possibilities to match the product of the muon charges,  $(q_1 q_2)$ , of the data event with that of the Monte Carlo event found in the box: if the product of charges is the same then either both Monte Carlo muons flipped their sign due to the oscillation of their parent  $B$  meson or none of them did; if the product of charges is not the same then one of the muons changed its sign and the other did not.

By maximising this likelihood  $\mathcal{L}$  as a function of  $\chi_B$ , or as is done in practice, by minimising  $-\log \mathcal{L}$ , a value of  $\chi_B$  is found that gives the most probable Monte Carlo description of the data. For the minimisation procedure MINUIT [69] is used.

The size of the four dimensional box is an unphysical parameter and has to be chosen a priori in unbinned fit methods and, as a consequence, has a systematic effect on the measurement. The box size is initially chosen to be  $(0.5 \times 0.5 \times 0.1 \times 0.1)$  GeV<sup>4</sup> but is allowed to increase with a factor 1.2 in both  $p_i$  and  $p_{ti}$  until it contains at least 40 dimuon Monte Carlo events. The box size is limited to  $(7.7 \times 7.7 \times 1.54 \times 1.54)$  GeV<sup>4</sup>, which corresponds to 15 steps in  $p$  and  $p_t$ . A few events do not satisfy this requirement and are no longer considered in the analysis since their calculated likelihood is considered to be unreliable. The minimum number of events in the box is varied in order to estimate the systematic error arising from this procedure. For this purpose special Monte Carlo files were used in which at least one  $b$  quark decayed semileptonically.

The main difference between the counting method and the likelihood fit is that the counting method is more sensitive to variations in the background (punch through etc.) which makes it necessary to apply a minimum  $p_t$  cut. This restriction can be released in the likelihood fit method thus providing more selected events and thus reducing the statistical error on  $\chi_B$ . Also the systematic effect when changing the branching ratios  $\text{Br}(b \rightarrow \mu + X)$  and  $\text{Br}(c \rightarrow \mu + X)$  is reduced in the unbinned likelihood fit method.

The following result has been obtained from the fit:

$$\chi_B = 0.118 \pm 0.027 \quad (5.11)$$

where the error is statistical only.

The same systematic error study as for the counting method is performed. One new possible cause is investigated, namely the minimum number of Monte Carlo events sampled. By requiring a minimum of 30 and 50 in stead of 40 events in each box,  $\chi_B$  changes by  $\pm 0.006$ . Again, as in the counting method, the uncertainty in the  $D^{**}$  abundance is of no influence on  $\chi_B$ . The result is summarised in table 5.5. The biggest contribution to the systematic error comes again from the limited number of Monte Carlo events. The use of the additional special Monte Carlo files helped to get the uncertainty down to 0.006 but even more Monte Carlo events are needed in the future to reduce this number.

Comparing this result with that obtained with the simple counting method it can be concluded that both methods give consistent results. The  $L_3$  measurement of  $\chi_B$ , which includes the inclusive electron analysis as well, is  $0.121 \pm 0.017(\text{stat}) \pm 0.006(\text{syst})$  [70], in good agreement with this analysis.

## 5.5 Determination of $\chi_s$ and CKM matrix elements

In figure 5.5 the  $L_3$  mixing result is shown in the  $\chi_s - \chi_d$  plane together with the Standard Model constraint on these two parameters [17]. Also shown in this plot is the combined result from the recent ARGUS and CLEO measurement on  $B_d^0 \bar{B}_d^0$  mixing on the  $\Upsilon(4S)$  resonance [71]:

$$\chi_d = 0.177 \pm 0.021 \quad (5.12)$$

Contribution	$\Delta\chi_B$
$c = 0.63 \pm 0.02$	$<0.001$
Changing the definition of opposite side from $45^\circ$ to $90^\circ$	0.001
$\text{Br}(b \rightarrow \mu + X) = 0.117 \pm 0.006$	0.003
$\text{Br}(c \rightarrow \mu + X) = 0.096 \pm 0.012$	0.002
Variation of the background fraction by $\pm 15\%$	0.001
Smearing of the muon momentum by $\Delta p/p = \Delta_\alpha \pm 30\%$ and smearing of the angle between the muon and the nearest jet by $(0.6 \pm 0.3)^\circ$	0.003
Changing the fragmentation parameter $\varepsilon_b = 0.050 \pm 0.006$ and changing the fragmentation parameter $\varepsilon_c = 0.5 \pm 0.1$	0.002
Charge confusion: $(0.2 \pm 0.2)\%$	0.002
Minimum number of Monte Carlo events sampled: 30 to 50	0.006
Total systematic error in $\chi_B$	0.008

Table 5.5: The various contributions to the systematic error of  $\chi_B$  as derived by the likelihood fit method.

$\chi_s$  can be calculated using these two measurements and  $\chi_B = f_d\chi_d + f_s\chi_s$  (1.31). It is assumed that all  $B$  mesons have the same semileptonic branching ratio and values for  $f_s$  and  $f_d$  are taken as described in the corresponding theory section in chapter 1. Not imposing the physical constraint  $0 < \chi_s < 0.5$ , yields:

$$\chi_s = 0.42 \pm 0.17 \quad (5.13)$$

Imposing this physical constraint, gives a one-dimensional limit of:

$$\chi_s > 0.18 \text{ at } 90\% \text{ confidence level.} \quad (5.14)$$

The measured value of  $\chi_s$  is sensitive to the relative production fractions of different  $b$ -hadrons. The dependence of  $\chi_s$  on  $f_s$  is shown in figure 5.6, under the assumption that  $f_u = f_d$ . The  $1\sigma$  errors include a 50% uncertainty on the value of  $f_B$ . The effect of this uncertainty is a factor 5 smaller than the statistical errors. The value of  $\chi_s$  is consistent with maximal mixing for any reasonable choice of  $f_d$ ,  $f_s$  and  $f_B$ .

Using equation 1.30,  $\chi_q = x_q^2 / (2(1 + x_q^2))$ , the quantities  $x_d$  and  $x_s$  can be calculated, giving:

$$\begin{aligned} x_d &= 0.74 \pm 0.07 \\ x_s &> 0.70 \text{ at } 90\% \text{ confidence level} \end{aligned} \quad (5.15)$$

Combining equation 5.15 with the  $L_3$  measurement for  $\tau_B = \Gamma_B^{-1} = 1.32 \pm 0.12$  ps [72], constraints on  $\Delta M_s$  and  $\Delta M_d$  are obtained, assuming  $\Gamma_s = \Gamma_d = \Gamma_B$ :

$$\Delta M_d = (3.7 \pm 0.5) 10^{-4} \text{ eV} \quad (5.16)$$



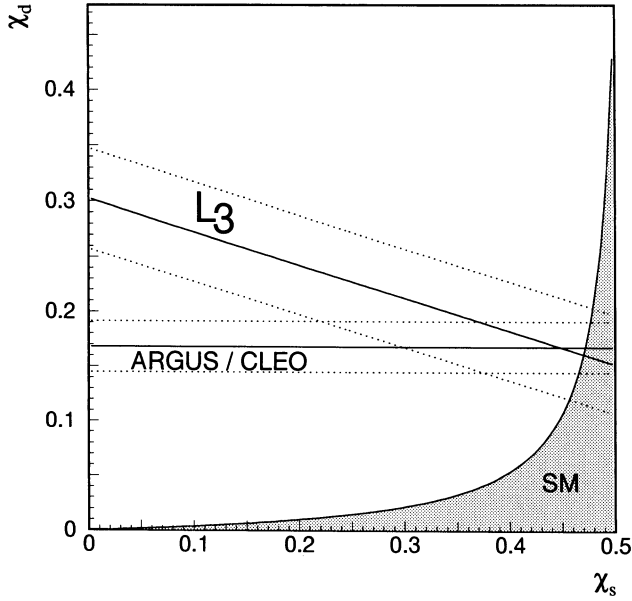


Figure 5.5: A comparison of  $L_3$ 's  $B^0 \bar{B}^0$  mixing result with those from ARGUS and CLEO. Also displayed is the Standard Model (SM) allowed (hatched) region.  $f_d = 0.40$  and  $f_s = 0.12$  is assumed, where  $\chi_B = f_d \chi_d + f_s \chi_s$ . The dashed lines correspond to  $1\sigma$  errors in both cases.

$$\Delta M_s > 3.5 \cdot 10^{-4} \text{ eV at } 90\% \text{ confidence level}$$

Equation 1.27 gives:

$$\left| \frac{V_{td}}{V_{ts}} \right|^2 = \frac{M_{B_s} B_{B_s} f_{B_s}^2 x_d}{M_{B_d} B_{B_d} f_{B_d}^2 x_s} \equiv \xi_{ds} \frac{x_d}{x_s} \quad (5.17)$$

Since the ratio  $\xi_{ds}$  is expected to be close to 1.0, it is assumed that  $\xi_{ds} = 1.0$  and one gets:

$$\left| \frac{V_{td}}{V_{ts}} \right| = 0.57 \pm 0.26 \quad (5.18)$$

As a last item of this chapter, the CP violation in the  $B$  system is investigated. Let  $a_{\ell\ell}$  be defined by:

$$a_{\ell\ell} \equiv \frac{N^{++} - N^{--}}{N^{++} + N^{--}} \quad (5.19)$$

with  $N^{++}$  and  $N^{--}$  as in section 5.2. It can be shown that for leptons emanating from a  $B_d \bar{B}_d$  or  $B_s \bar{B}_s$  system [73]:

$$a_q \equiv \frac{N_{bb}^{++} - N_{bb}^{--}}{N_{bb}^{++} + N_{bb}^{--}} = \frac{|p_q|^2 - |q_q|^2}{|p_q|^2 + |q_q|^2} \quad (5.20)$$

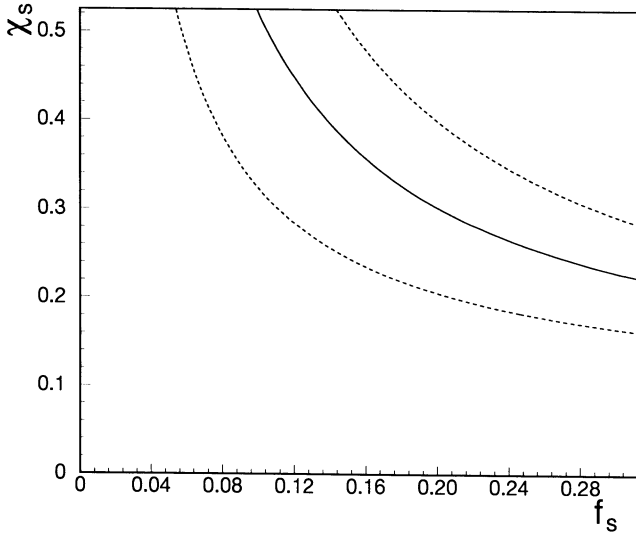


Figure 5.6:  $\chi_s$  as a function of  $f_s$ . The dashed lines are  $1\sigma$  errors and include a 50% uncertainty on the value of  $f_B$ , the fraction of  $B$  baryons produced.

with  $p_q$  and  $q_q$  as defined in equation 1.23. Using equation 1.24, we get:

$$a_q = \langle B_q^1 | B_q^2 \rangle \quad (5.21)$$

Since  $B_d$  and  $B_s$  mesons are both produced at LEP,  $a_{\ell\ell}$  is a weighted average of  $a_d$  and  $a_s$  [73]:

$$a_{\ell\ell} \approx 0.59a_d + 0.50a_s \quad (5.22)$$

In order to calculate  $a_{\ell\ell}$  the following equation is used, with  $f_i$  as in section 5.2:

$$a_{\ell\ell}(\text{data}) = \sum_{i=21}^{28} f_i a_{\ell\ell}(i) \quad (5.23)$$

in which  $a_{\ell\ell}(i)$  is the asymmetry for category  $i$ . Taking  $f_i$  from table 5.2,  $a_{\ell\ell}(\text{data})$  from table 5.1 and  $a_{\ell\ell}(i)$  for  $i = 23, \dots, 28$  from the Monte Carlo sample,  $a_{\ell\ell} = a_{\ell\ell}(21) = a_{\ell\ell}(22)$  can be calculated using equation 5.23:

$$a_{\ell\ell} = 0.10 \pm 0.16 \quad (5.24)$$

where the error is statistical only. This implies  $0.59\langle B_d^1 | B_d^2 \rangle + 0.50\langle B_s^1 | B_s^2 \rangle = 0.10 \pm 0.16$  which is consistent with  $10^{-3}$  to  $10^{-4}$  as estimated in the context of the Standard Model [12].

**Box 5.1**  $\chi_B, \chi_s$  and CKM constraints

$$\chi_B = 0.090 \pm 0.029 \text{ (stat)} \pm 0.012 \text{ (syst) from counting}$$

$$\chi_B = 0.118 \pm 0.027 \text{ (stat)} \pm 0.008 \text{ (syst) from fit}$$

$$\chi_B = 0.121 \pm 0.017 \text{ (stat)} \pm 0.006 \text{ (syst) from } L_3$$

$$\chi_s > 0.18 \text{ at 90\% confidence level}$$

$$\left| \frac{V_{td}}{V_{ts}} \right| = 0.57 \pm 0.26$$



# Chapter 6

## Forward backward asymmetry

Mean $\sqrt{s}$	$A_{fb}$
89.33 GeV	$0.044 \pm 0.007 \pm 0.008$
91.24 GeV	$0.086 \pm 0.022 \pm 0.008$
93.08 GeV	$0.102 \pm 0.053 \pm 0.008$

Table 6.5:  $A_{fb}$  for different center-of-mass energies. Note that the systematic error 0.008 is common to all points.

$L_3$  measurements of  $A_{fb}$  and  $A_{ce}$ , which includes inclusive electron analysis as well, are  $0.086 \pm 0.015(\text{stat}) \pm 0.007(\text{sys})$  and  $0.083 \pm 0.038(\text{stat}) \pm 0.027(\text{sys})$  respectively [74], in good agreement with this analysis.

To study the asymmetry as a function of the centre of mass energy, the data sample is divided in energies below, on, and above the  $Z^0$  resonance. The results for  $A_{fb}$  are shown in table 6.5. Because of limited statistics, this procedure has not been performed for the  $A_{ce}$  measurement.

### 6.5 Determination of $\sin^2 \bar{\theta}_W$

After including the  $L_3$  measurement of  $A_{fb}$  and  $A_{ce}$  with inclusive electrons, the results for  $A_{fb}$  and  $A_{ce}$  are [74]:

$$\begin{aligned} A_{fb} &= 0.086 \pm 0.015 \pm 0.007 \\ A_{ce} &= 0.083 \pm 0.038 \pm 0.027 \end{aligned} \quad (6.15)$$

The program ZFITTER [14] is used to perform the QED and QCD corrections and extract  $\sin^2 \bar{\theta}_W$ :

$$\sin^2 \bar{\theta}_W = 0.2336 \pm 0.0029 \quad (6.16)$$

Figure 6.5 shows the energy dependence of  $A_{fb}$  for the Standard Model expectation with  $\sin^2 \bar{\theta}_W = 0.2336$  compared with the data.

A comparison with the results from the  $L_3$  lepton asymmetry [45] and  $L_3$   $\tau$  polarisation measurement [75] is shown in figure 6.6. The measurement of  $\sin^2 \bar{\theta}_W$  from  $A_{fb}$  has the smallest error (see section 4.1). Averaging the three numbers gives:  $0.2315 \pm 0.0019$ .

The top quark has not yet been observed directly. However, from the Born approximations for  $\Gamma_{bb}$ , equation 1.11, and  $A_{fb}$ , equation 1.19, one can see that depending on the isospin quantum number  $I_3^t$  the following is obtained:

$$\begin{aligned} \Gamma_{bb}|_{I_3^t=+1/2} &\approx 380 \text{ MeV} & A_{fb}|_{I_3^t=+1/2} &\approx 0.08 \\ \Gamma_{bb}|_{I_3^t=0} &\approx 30 \text{ MeV} & A_{fb}|_{I_3^t=0} &\approx 0 \end{aligned} \quad (6.17)$$

Clearly, the case  $I_3^t = 0$  (isospin singlet) is ruled out, not only by the measurement of  $\Gamma_{bb} = 389 \pm 23 \text{ MeV}$ , as described in the next chapter, but by the  $A_{fb}$  measurement as

## 6.1 Introduction

In this analysis, the forward backward asymmetry,  $A_{FB}$ , defined in section 1.4, is calculated by tagging  $b$  and  $c$  quarks through their semileptonic decay into muons. With the charge of the muon,  $Q_\mu$ , the direction of the  $b$  quark is given by  $-Q_\mu \cos \theta_{\text{thrust}}$ .  $\theta_{\text{thrust}}$  is the angle between the thrust axis of the event, the best approximation of the quark direction, and the  $e^+e^-$  beam. The direction of the thrust axis, two possibilities, is chosen to be the one closest to the muon, see figure 6.1. For  $c$  quarks, since the semileptonically

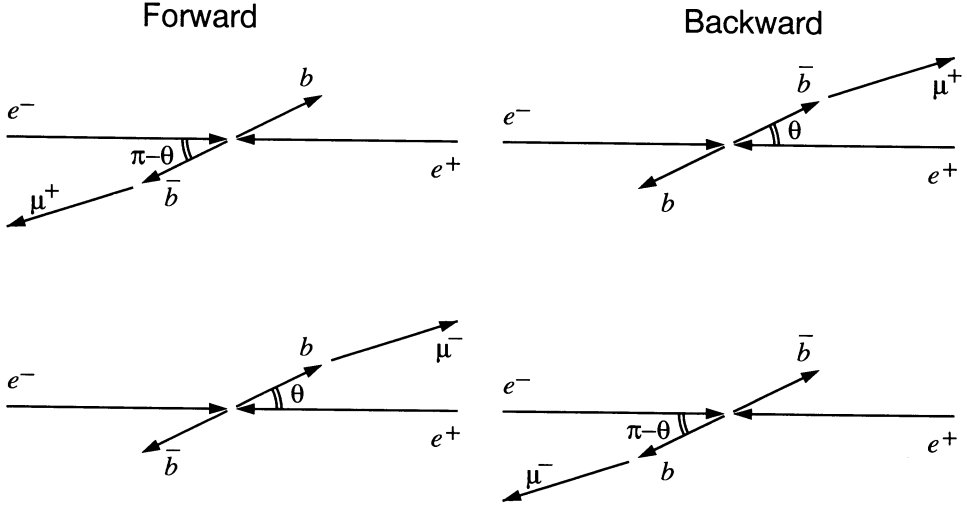


Figure 6.1: Definition of forward and backward through  $-Q_\mu \cos \theta_{\text{thrust}}$ .

produced muon has the opposite charge of a muon from a  $b$  decay, not  $A_{c\bar{c}}$  but  $-A_{c\bar{c}}$  is determined this way.

For the  $b$  quark asymmetry a complication occurs due to the  $B^0\bar{B}^0$  oscillations, described in the previous chapter. This effectively reduces the observed asymmetry by a factor  $(1 - 2\chi_B)$  because such an oscillation will change the event from being interpreted as forward to backward and vice versa:

$$A_{b\bar{b}}^{\text{obs}} = A_{b\bar{b}}(1 - 2\chi_B) \quad (6.1)$$

As there is no observable mixing in the  $D$  meson system,  $A_{c\bar{c}}$  is measured directly.

## 6.2 Event selection and angular distribution

Events with (at least) one muon are required and the data sample is described in table 6.1. The data sample is split into three energy bins:

1. below the  $Z^0$  peak:  $\sqrt{s} < 90.75$  GeV;
2. on the  $Z^0$  peak:  $90.75 \text{ GeV} \leq \sqrt{s} < 91.75$  GeV;
3. above the  $Z^0$  peak:  $\sqrt{s} \geq 91.75$  GeV.

$p_{t\mu\text{min}}$	below	on the peak	above	Total
0.00 GeV	1957	17,788	2865	22,610
1.00 GeV	825	7,706	1257	9,788

Table 6.1: *The single muon data sample containing the 1990 and 1991 data.*

Figure 6.2 shows the  $-Q_\mu \cos \theta_{\text{thrust}}$  distribution for all selected inclusive muon events with  $p_t > 1.0$  GeV. By counting the number of events in the forward and in the backward direction, a rough estimate of the observed asymmetry,  $A^{\text{obs}}$ , is calculated. Using only events with  $|\cos \theta_{\text{thrust}}| < 0.8$  and correcting the observed asymmetry for this angular acceptance, yields:

$$A^{\text{obs}} = \frac{N_F - N_B}{N_F + N_B} \frac{3 + \cos^2(0.8)}{4 \cos(0.8)} \approx 0.045 \pm 0.011 \quad (6.2)$$

This observed asymmetry is a net effect of all the different sources of inclusive muon production in the sample (see table 4.3). After requiring  $p_{t\mu} > 1.0$  GeV, the fraction of prompt  $b \rightarrow \mu$  events is almost doubled and the background fraction has become small enough to be subtracted without introducing a large systematic error. Applying geometrical acceptance corrections and sequentially subtracting all background processes results in figure 6.3. For this plot, the geometrical acceptance is estimated by adding to the data  $-Q_\mu \cos \theta_{\text{thrust}}$  histogram its mirror image  $Q_\mu \cos \theta_{\text{thrust}}$ . This should result in a  $(1 + \cos^2 \theta)$  distribution and each bin is, after normalisation, corrected to meet this  $(1 + \cos^2 \theta)$  distribution. Under the assumption that the detector is symmetric in  $Q_\mu \cos \theta_{\text{thrust}}$ , this procedure guarantees that the asymmetry will not be influenced by a discrepancy between data and Monte Carlo. This assumption is shown to be valid using the  $Z^0 \rightarrow \mu^+ \mu^-$  sample [15]. This fact will be exploited in the determination of  $A_{b\bar{b}}$  as described in the following section. The distribution in figure 6.3 is clearly asymmetric. The solid curve shows the distribution for  $A_{b\bar{b}}^{\text{obs}} = 0.067 \pm 0.015$  obtained in the following sections.

The  $b$  quark asymmetry is determined in two ways. The first, based on a simple method, will serve as a cross check to the second, more complicated, method.

### 6.3 Simple fit method

In this section a simple way to determine  $A_{b\bar{b}}$  from the data is described. It makes use of the fact that after requiring that all muons have a high  $p_{t\mu}$ , most of the events

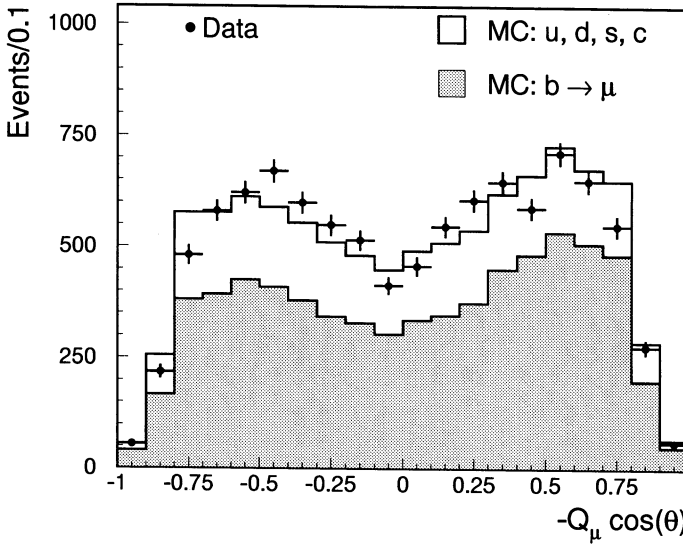


Figure 6.2: The distribution of the measured  $b$  quark direction (thrust axis) for the inclusive muon data with  $p_t > 1.0$  GeV.

will be prompt  $b \rightarrow \mu$  events, see table 4.3. Since all events are produced with the same  $1 + \cos^2 \theta + \frac{8}{3} A_i \cos \theta$  distribution, the observed asymmetry,  $A^{\text{obs}}$ , can be calculated as follows:

$$A^{\text{obs}} = (1 - 2\chi_B) A_{b\bar{b}} (f_1 - f_2 + f_3 + f_4) + A_5 f_5 - A_{c\bar{c}} f_6 + A_{\text{back}} (f_7 + f_8) \quad (6.3)$$

in which the  $f_i$  are the relative fractions of the various event types, (table 4.3). In this equation,  $A_{b\bar{b}}^{\text{obs}}$  is already replaced by  $(1 - 2\chi_B) A_{b\bar{b}}$  as explained in the introduction of this chapter. The negative sign for  $f_2$  is a consequence of the fact that in this cascade decay ( $b \rightarrow c \rightarrow \mu$ ) the sign of the muon is opposite to the sign of the muon coming directly from a  $b$  quark. The minus sign in front of  $A_{c\bar{c}}$  is needed because in the decay  $c \rightarrow \mu$  the muon has the opposite sign of a muon originating from a  $b \rightarrow \mu$  decay. The quantity  $A_5$  (strongly related to  $\chi_5$  of equation 5.3) is defined by

$$A_5 = (2c - 1) A_{b\bar{b}} (1 - 2\chi_B) \quad (6.4)$$

in which  $c$  is the probability that a  $b(\bar{b})$  quark will decay via some cascade (not  $b \rightarrow c \rightarrow \mu$ ,  $b \rightarrow \bar{c} \rightarrow \mu$  or  $b \rightarrow \tau \rightarrow \mu$ ) into a negative (positive) particle which is then detected by the muon chambers. This means that as long as  $c$  does not equal 0.5 information about the charge of the  $B$  meson is still available in the charge of the particle detected by the muon



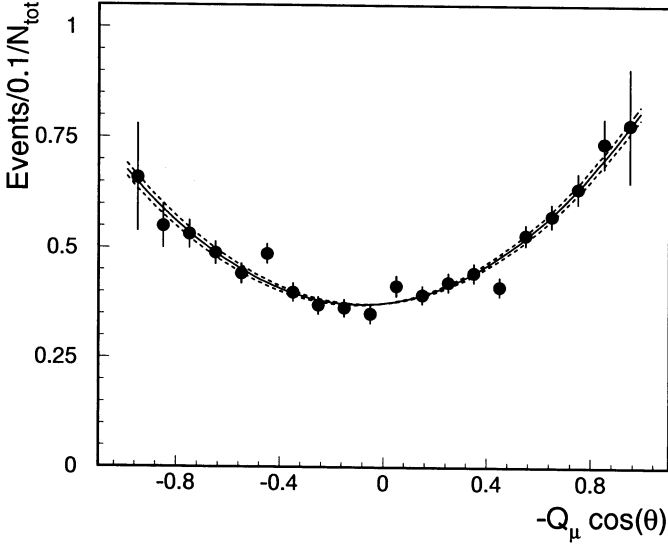


Figure 6.3: The acceptance corrected distribution of the measured  $b$  quark direction (thrust axis) for the inclusive muon data with  $p_{t\mu} > 1.0$  GeV. The solid curve shows the distribution for the fit result  $A_{b\bar{b}}^{\text{obs}} = 0.067 \pm 0.015$ . The dashed lines indicate the experimental statistical uncertainty.

chambers. From the Monte Carlo  $c$  is determined to be  $0.63 \pm 0.02$  (equation 5.4).  $A_{c\bar{c}}$  is removed from equation 6.4 by exploiting the fact that the Standard Model constrains  $A_{c\bar{c}}$  to approximately  $0.7A_{b\bar{b}}$  at  $\sqrt{s} \approx M_Z$ .  $A_{\text{back}}$  is taken from the Monte Carlo asymmetry for events of type 7 or 8, restricting the muons to  $p_{t\mu} > 1.0$  GeV.

$A^{\text{obs}}$  and  $A_{\text{back}}$  are derived, from the data sample and the Monte Carlo sample respectively, in the following way. The  $-Q_{\mu} \cos \theta_{\text{thrust}}$  distribution is divided into 20 bins and out of these 20 bins 10 pairs are taken by coupling each bin with its opposite bin in  $-Q_{\mu} \cos \theta_{\text{thrust}}$ . For each pair of bins at  $\pm \cos \theta_i$  the likelihood  $f(i)$  is constructed:

$$f(i) = p_i^{F_i} (1 - p_i)^{B_i} \quad \text{with} \quad p_i = \frac{1}{2} \left( \frac{\frac{8}{3} A^{\text{obs}} \cos \theta_i}{1 + \cos^2 \theta_i} + 1 \right) \quad (6.5)$$

in which  $F_i$  and  $B_i$  are the number of events counted as forward respectively backward in this  $\pm \cos \theta_i$  pair and  $p_i$  is the probability to be a forward event. By pairing opposite bins in  $\cos \theta$ , acceptance effects can be neglected under the assumption that the detector is symmetric in  $\cos \theta$  and symmetric for positive and negative muons. This then gives the

likelihood function  $\mathcal{L}$ :

$$\mathcal{L} = \prod_{i=1}^{10} f(i) \quad (6.6)$$

By optimising  $\mathcal{L}$  (as described in the previous chapter)  $A^{\text{obs}}$  and  $A_{\text{back}}$  are calculated:

$$A^{\text{obs}} = 0.040 \pm 0.011 \quad (6.7)$$

$$A_{\text{back}} = -0.010 \pm 0.022 \quad (6.8)$$

Now equation 6.4 can be solved for  $A_{b\bar{b}}$ , using  $\chi_B = 0.121 \pm 0.018$  (see previous chapter), giving:

$$A_{b\bar{b}} = 0.086 \pm 0.022 \quad (6.9)$$

where the error is statistical only.

By varying all known quantities that could contribute to the systematic error in the measurement of  $A_{b\bar{b}}$  by their measured or estimated error, the systematic error on  $A_{b\bar{b}}$  is estimated.

First, all known quantities that have a measured error are varied by this error (or in case of  $\text{Br}(c \rightarrow \mu + X)$  by two times this error as explained in section 4.4). Changing the number of bins from 20 to 14 did not change the measured values and so no systematic error has been assigned due to the bin size. The Standard Model constraint used to eliminate  $A_{c\bar{c}}$  from equation 6.4 is varied with  $(0.7 \pm 0.3)A_{b\bar{b}}$  giving a systematic error of 0.002 on  $A_{b\bar{b}}$ .

Next, the influence of the minimum  $p_t$  cut is investigated. Figure 6.4 shows  $A_{b\bar{b}}/A_{b\bar{b}}^0$  as a function of the minimum  $p_t$  with  $A_{b\bar{b}}^0$  the nominal value for a minimum  $p_t$  of 1.0 GeV:  $A_{b\bar{b}}^0 = 0.086$ . This plot takes the relative change in statistics into account: for each  $p_t$  cut other than 1.0 GeV, the relative change in  $N_F$  and  $N_{\text{tot}}$  is calculated:  $\Delta N_F$  and  $\Delta N_{\text{tot}}$ . Using the same Monte Carlo fractions  $f_i$  and  $N_{\text{tot}}$  but  $N_F \pm \sigma(\Delta N_F)$  in stead of  $N_F$ , with

$$\sigma(\Delta N_F) = \sqrt{\Delta N_{\text{tot}} t(1-t)} \quad (6.10)$$

with

$$t = \frac{\Delta N_F}{\Delta N_{\text{tot}}} \quad (6.11)$$

the change in  $A_{b\bar{b}}$  is calculated. Applying this procedure to all points and normalising them to  $A_{b\bar{b}}^0$ , results in the plot. As all variations in  $A_{b\bar{b}}/A_{b\bar{b}}^0$  are statistically consistent, no systematic error due to this minimum  $p_t$  cut is assigned.

The systematic error coming from the uncertainty on the background fraction predicted by the Monte Carlo is estimated as explained in the previous chapter. The change in  $A_{b\bar{b}}$  due to this uncertainty is  $\pm 0.002$ .

The difference in muon momentum resolution and jet angular resolution between data and Monte Carlo causes a difference in the muon  $p_t$  resolution between data and Monte Carlo (see section 4.4). In order to study the systematic influence on  $A_{b\bar{b}}$  of this effect, the Monte Carlo muon momentum and angle between muon and accompanying jet are smeared. The change in  $A_{b\bar{b}}$  is  $\pm 0.004$ .

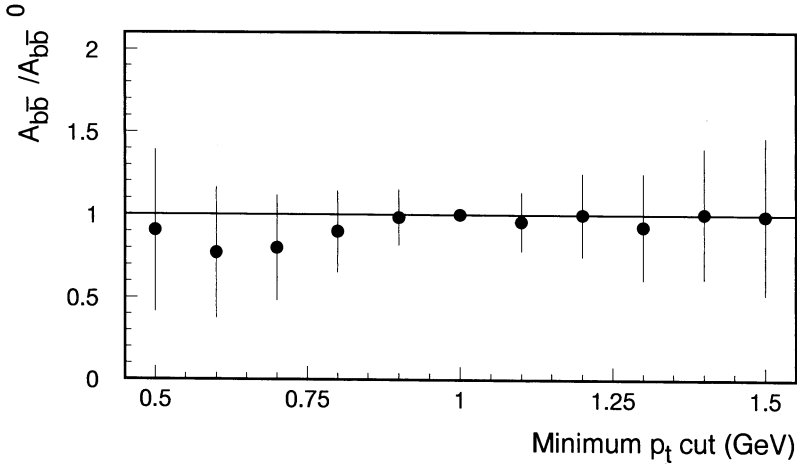


Figure 6.4: The variation of  $A_{b\bar{b}}^0/A_{b\bar{b}}^0$  as a function of the minimum  $p_t$ .

The effect on  $A_{b\bar{b}}$  of the uncertainty in the  $D^{**}$  abundance (see section 4.4) is studied by varying this abundance by  $(22 \pm 7)\%$ . The measurement of  $A_{b\bar{b}}$  changes less than 0.001 and therefore no systematic error has been assigned.

The charge confusion for muons is estimated to be  $(0.2 \pm 0.2)\%$  as described in section 5.3. The measurement of  $A_{b\bar{b}}$  is corrected for this effect and its error changes  $A_{b\bar{b}}$  by  $\pm 0.001$ .

Table 6.2 summarises this systematic error study. The poor knowledge of  $A_{\text{back}}$  provides the largest contribution to the systematic error. However, reducing this contribution will not decrease the total systematic error significantly and as the value for  $A_{b\bar{b}}$  obtained in this section is only to be used as a cross check for the method described in the following section, no effort has been put into reducing this error.

## 6.4 The two dimensional unbinned likelihood fit

As in the previous chapter, an event by event unbinned maximum likelihood fit is performed. Only this time the advantage over the simple method is twofold: more statistics can be used and the forward backward asymmetry for the  $c$  quark can be determined.

The likelihood function is defined as

$$\mathcal{L} = \prod_{i=1}^N f(i) \quad \text{with} \quad f(i) = \frac{1}{M \cdot V_{\text{box}}(i)} \sum_k N_k(i) W_k(i) \quad (6.12)$$

in which  $f(i)$  is the probability density and  $N_k$  is the number of Monte Carlo muon events of type  $k$  found in the volume of the two dimensional box  $V_{\text{box}}(i)$  around data point  $i$ , in  $(p, p_t)$  space.  $N(M)$  is the total number of data (Monte Carlo) events selected.  $M$  is

Contribution	$\Delta A_{b\bar{b}}$
$c = 0.63 \pm 0.02$	0.001
Changing $A_{c\bar{c}}$ from $0.4A_{b\bar{b}}$ to $A_{b\bar{b}}$	0.002
Changing $A_{\text{back}}$	0.005
$\text{Br}(b \rightarrow \mu + X) = 0.117 \pm 0.006$	0.002
$\text{Br}(c \rightarrow \mu + X) = 0.096 \pm 0.012$	0.004
Variation of the background fraction by $\pm 15\%$	0.002
Smearing of the muon momentum by $\Delta p/p = \Delta_\alpha \pm 30\%$ and smearing of the angle between the muon and the nearest jet by $(0.6 \pm 0.3)^\circ$	0.004
Changing the fragmentation parameter $\varepsilon_b = 0.050 \pm 0.006$ and changing the fragmentation parameter $\varepsilon_c = 0.5 \pm 0.1$	0.001
Charge confusion: $(0.2 \pm 0.2)\%$	0.001
$\chi_B = 0.121 \pm 0.018$	0.004
Total systematic error in $A_{b\bar{b}}$	0.009

Table 6.2: The various contributions to the systematic error as derived by the simple fit method.

normalised by multiplying it with the ratio of the number of selected data hadron events and the number of selected Monte Carlo hadron events.  $W_k(i)$ , the weighting function, is defined as follows:

$$W_k(i) = \frac{1}{2} \left[ 1 + \frac{8A_k \cos \theta_i}{3(1 + \cos^2 \theta_i)} \right] \quad (6.13)$$

The asymmetry for category  $k$ ,  $A_k$ , is given in table 6.3 in which  $A_5$  is defined as before (equation 6.4).

This likelihood  $\mathcal{L}$  is maximised as a function of  $A_{b\bar{b}}^{\text{obs}}$  and  $A_{c\bar{c}}$ . The correlation coefficient between  $A_{b\bar{b}}^{\text{obs}}$  and  $A_{c\bar{c}}$  is obtained from the fit procedure and equals  $+20\%$ .

By varying all known quantities that could contribute to the systematic error in the measurement of  $A_{b\bar{b}}$  and  $A_{c\bar{c}}$  by their measured or estimated error, the systematic errors on  $A_{b\bar{b}}$  and  $A_{c\bar{c}}$  are estimated. The summary is shown in table 6.4. No special attention was put in reducing the major contribution to the total systematic error on  $A_{b\bar{b}}^{\text{obs}}$ . The reason being that the contribution from  $\chi_B$  and the statistical error are still (much) larger. The uncertainty on  $A_{\text{back}}$  was determined by calculating  $A_{\text{back}}$  in the Monte Carlo. Due to the low statistics the error on  $A_{\text{back}}$  is as large as 0.018, yielding the largest contribution to the total error on  $A_{c\bar{c}}$ .

After correcting  $A_{b\bar{b}}^{\text{obs}}$  for the effect of mixing,  $A_{b\bar{b}} = A_{b\bar{b}}^{\text{obs}} / (1 - 2\chi_B)$ , with  $\chi_B = 0.121 \pm 0.018$ , one gets:

$$\begin{aligned} A_{b\bar{b}} &= 0.088 \pm 0.020 \text{ (stat)} \pm 0.008 \text{ (syst)} \\ A_{c\bar{c}} &= 0.095 \pm 0.039 \text{ (stat)} \pm 0.028 \text{ (syst)} \end{aligned} \quad (6.14)$$

This result for  $A_{b\bar{b}}$  is consistent with that obtained with the simple fit method. The

Category $k$	$A_k$
1: $b \rightarrow \mu$	$A_{b\bar{b}}^{\text{obs}}$
2: $b \rightarrow c \rightarrow \mu$	$-A_{b\bar{b}}^{\text{obs}}$
3: $b \rightarrow \tau \rightarrow \mu$	$A_{b\bar{b}}^{\text{obs}}$
4: $b \rightarrow \bar{c} \rightarrow \mu$	$A_{b\bar{b}}^{\text{obs}}$
5: $b \rightarrow \text{background}$	$A_5$
6: $c \rightarrow \mu$	$-A_{c\bar{c}}$
7: decay	$A_{\text{back}}$
8: punch through	$A_{\text{back}}$

Table 6.3: The asymmetry used in the fit method for each category.

Contribution	$\Delta A_{b\bar{b}}^{\text{obs}}$	$\Delta A_{c\bar{c}}$
$c = 0.63 \pm 0.02$	0.000	0.001
$A_{\text{back}} = 0.000 \pm 0.018$	0.000	0.025
$\text{Br}(b \rightarrow \mu + X) = 0.117 \pm 0.006$	0.001	0.002
$\text{Br}(c \rightarrow \mu + X) = 0.096 \pm 0.012$ <sup>1</sup>	0.001	0.005
$\Gamma_{b\bar{b}} = 378 \pm 10$ MeV	0.000	0.001
$\Gamma_{c\bar{c}} = 297 \pm 10$ MeV	0.000	0.001
Variation of the background fraction by $\pm 15\%$	0.001	0.004
Smearing of the muon momentum by $\Delta p/p = \Delta_\alpha \pm 30\%$ and smearing of the angle between the muon and the nearest jet by $(0.6 \pm 0.3)^\circ$	0.004	0.005
Changing the fragmentation parameter $\varepsilon_b = 0.050 \pm 0.006$ and changing the fragmentation parameter $\varepsilon_c = 0.5 \pm 0.1$	0.000	0.004
Charge confusion: $(0.2 \pm 0.2)\%$	0.001	0.001
Minimum number of Monte Carlo events sampled: 30 to 50	0.000	0.002
Total systematic error	0.005	0.028

<sup>1</sup>For  $\Delta A_{c\bar{c}}$  0.096  $\pm$  0.006 was taken.

Table 6.4: The various contributions to the systematic errors as derived by the likelihood fit method.

Mean $\sqrt{s}$	$A_{b\bar{b}}$
89.33 GeV	$0.044 \pm 0.067 \pm 0.008$
91.24 GeV	$0.086 \pm 0.022 \pm 0.008$
93.08 GeV	$0.102 \pm 0.053 \pm 0.008$

Table 6.5:  $A_{b\bar{b}}$  for different center-of-mass energies. Note that the systematic error 0.008 is common to all points.

$L_3$  measurements of  $A_{b\bar{b}}$  and  $A_{c\bar{c}}$ , which includes inclusive electron analysis as well, are  $0.086 \pm 0.015(\text{stat}) \pm 0.007(\text{syst})$  and  $0.083 \pm 0.038(\text{stat}) \pm 0.027(\text{syst})$  respectively [74], in good agreement with this analysis.

To study the asymmetry as a function of the centre of mass energy, the data sample is divided in energies below, on, and above the  $Z^0$  resonance. The results for  $A_{b\bar{b}}$  are shown in table 6.5. Because of limited statistics, this procedure has not been performed for the  $A_{c\bar{c}}$  measurement.

## 6.5 Determination of $\sin^2 \bar{\theta}_W$

After including the  $L_3$  measurement of  $A_{b\bar{b}}$  and  $A_{c\bar{c}}$  with inclusive electrons, the results for  $A_{b\bar{b}}$  and  $A_{c\bar{c}}$  are [74]:

$$\begin{aligned} A_{b\bar{b}} &= 0.086 \pm 0.015 \pm 0.007 \\ A_{c\bar{c}} &= 0.083 \pm 0.038 \pm 0.027 \end{aligned} \quad (6.15)$$

The program ZFITTER [14] is used to perform the QED and QCD corrections and extract  $\sin^2 \bar{\theta}_W$ :

$$\sin^2 \bar{\theta}_W = 0.2336 \pm 0.0029 \quad (6.16)$$

Figure 6.5 shows the energy dependence of  $A_{b\bar{b}}$  for the Standard Model expectation with  $\sin^2 \bar{\theta}_W = 0.2336$  compared with the data.

A comparison with the results from the  $L_3$  lepton asymmetry [45] and  $L_3$   $\tau$  polarisation measurement [75] is shown in figure 6.6. The measurement of  $\sin^2 \bar{\theta}_W$  from  $A_{b\bar{b}}$  has the smallest error (see section 4.1). Averaging the three numbers gives:  $0.2315 \pm 0.0019$ .

The top quark has not yet been observed directly. However, from the Born approximations for  $\Gamma_{b\bar{b}}$ , equation 1.11, and  $A_{b\bar{b}}$ , equation 1.19, one can see that depending on the isospin quantum number  $I_3^b$  the following is obtained:

$$\begin{aligned} \Gamma_{b\bar{b}}|_{I_3^b=-1/2} &\approx 380 \text{ MeV} & A_{b\bar{b}}|_{I_3^b=-1/2} &\approx 0.08 \\ \Gamma_{b\bar{b}}|_{I_3^b=0} &\approx 30 \text{ MeV} & A_{b\bar{b}}|_{I_3^b=0} &\approx 0 \end{aligned} \quad (6.17)$$

Clearly, the case  $I_3^b = 0$  (isospin singlet) is ruled out, not only by the measurement of  $\Gamma_{b\bar{b}} = 389 \pm 23 \text{ MeV}$ , as described in the next chapter, but by the  $A_{b\bar{b}}$  measurement as

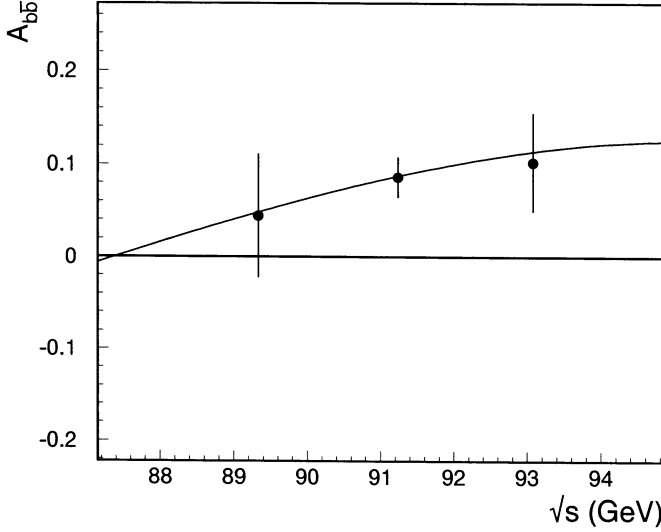


Figure 6.5: *The energy dependence of  $A_{b\bar{b}}$  compared to the Standard Model expectation with  $\sin^2 \bar{\theta}_W = 0.2336$ . The errors are statistical only.*

described in this chapter as well. Hence,  $I_3^b = -1/2$  and therefore the  $b$  quark must have an isospin  $I_3^f = +1/2$  partner, namely the top quark.

In fact the above mentioned observables do not only require the top quark to exist but also constrain its mass. From  $\sin^2 \bar{\theta}_W$ , obtained from the  $A_{b\bar{b}}$  measurement, a constraint on the top quark mass can be obtained. Using the  $L_3$  measurement of  $\sin^2 \theta_W = 0.227 \pm 0.005$  [45] and the relationship between  $\sin^2 \theta_W$  and  $\sin^2 \bar{\theta}_W$  (1.10), gives:

$$M_t = 157 \pm 75 \pm 13 \text{ (Higgs) GeV} \quad (6.18)$$

The second error on  $M_t$  is estimated by varying the mass of the Higgs boson from 50 GeV to 1000 GeV.

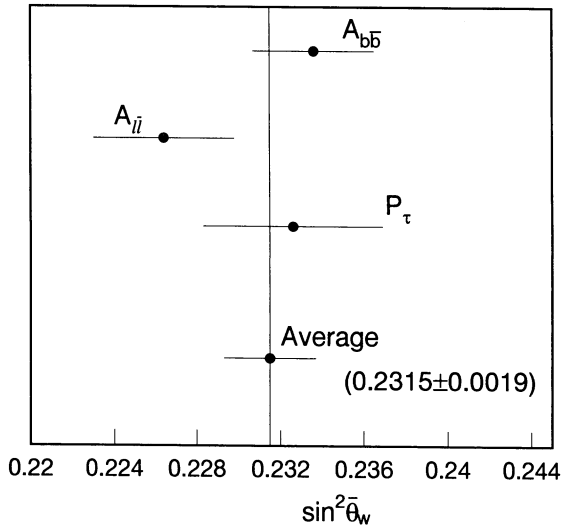


Figure 6.6: A comparison of the  $\sin^2 \bar{\theta}_W$  determination from  $A_{b\bar{b}}$  with the results from the  $L_3$  lepton asymmetry,  $A_{l\bar{l}}$ , and  $L_3$   $\tau$  polarisation measurement,  $P_\tau$ .

### Box 6.1 Results

$$\begin{aligned}
 A_{b\bar{b}} &= 0.088 \pm 0.020 \text{ (stat)} \pm 0.008 \text{ (syst)} \\
 A_{c\bar{c}} &= 0.095 \pm 0.039 \text{ (stat)} \pm 0.029 \text{ (syst)} \\
 \sin^2 \bar{\theta}_W &= 0.2336 \pm 0.0029 \\
 M_t &= 157 \pm 75 \pm 13 \text{ (Higgs) GeV}
 \end{aligned}$$



# Chapter 7

## Measurement of $\text{Br}(b \rightarrow \mu + X)$ , $\Gamma_{b\bar{b}}$ and $\Gamma_{c\bar{c}}$

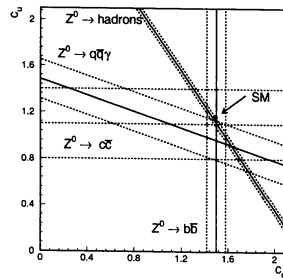


Figure 7.3. Constraints on the  $u$  and  $d$  type quark electroweak couplings derived from the total hadronic decay width of the  $Z^0$  (thin inclined band), from photon distributions in  $qq\gamma$  events (thick inclined band) and from the measurement of  $\Gamma_{bb}$  and  $\Gamma_{cc}$  as described in this thesis (thick vertical and horizontal bands). The Standard Model values of the couplings are shown as a solid circle.

## 7.1 Introduction

For the analyses described in this chapter, part of the 1992 data run has been added to the 1990 and 1991 data sample. This results in an approximate doubling of the data sample.

By counting the number of muons from a prompt  $b$  decay the branching ratio of  $B$  hadrons decaying into a muon,  $\text{Br}(b \rightarrow \mu + X)$ , times the fraction of  $b\bar{b}$  events produced,  $\Gamma_{b\bar{b}}/\Gamma_{\text{had}}$ , is obtained. In order to measure  $\Gamma_{b\bar{b}}/\Gamma_{\text{had}}$  one has to determine  $\text{Br}(b \rightarrow \mu + X)$  independently.

In the next section  $\text{Br}(b \rightarrow \mu + X)$  is calculated, exploiting the fact that the number of events with two prompt muons relative to the number of events with just one prompt muon is almost independent of  $\Gamma_{b\bar{b}}/\Gamma_{\text{had}}$ . With the value for  $\text{Br}(b \rightarrow \mu + X)$ , the CKM matrix element  $|V_{cb}|$  is calculated in section 7.3. In section 7.4,  $\Gamma_{b\bar{b}}$  and  $\Gamma_{c\bar{c}}$  are extracted from the data.

## 7.2 Determination of $\text{Br}(b \rightarrow \mu + X)$

By counting the number of dimuon events<sup>1</sup> and the number of single muon events, the branching ratio  $\text{Br}(b \rightarrow \mu + X)$  can be calculated. The ratio of dimuon events over single muon events is, to first order, proportional to  $\text{Br}(b \rightarrow \mu + X)$  and independent of  $\Gamma_{b\bar{b}}$ . This can easily be seen in the simplified picture where all inclusive muons come from prompt  $b \rightarrow \mu$  decay:

$$R = \frac{N_2}{N_1} = \frac{B^2}{2B(1-B)} \quad \text{or} \quad B = \frac{2R}{1+2R} \quad (7.1)$$

with  $B = \text{Br}(b \rightarrow \mu + X)$ . Due to the presence of background processes, equation 7.1 is an oversimplification of the real situation. For the purpose of calculating the branching ratio, all events are divided into four categories:

- 1:  $b \rightarrow \mu$  and  $b \rightarrow \mu$ : both  $b$  quarks decaying into a muon,
- 2:  $b \rightarrow \mu$  and  $b \not\rightarrow \mu$ : only one  $b$  quark decaying into a muon while the other does not,
- 3:  $b \not\rightarrow \mu$  and  $b \not\rightarrow \mu$ : both  $b$  quarks not decaying into a muon and
- 4:  $u, d, s, c$  events where no  $b$  quark is involved.

These four categories can then be subdivided into "seen as single muon event" (1a, 2a, 3a, 4a) and "seen as dimuon event" (1b, 2b, 3b, 4b). Let  $a_i$  and  $b_i$  ( $i = 1, \dots, 4$ ) be the acceptances for these eight subcategories, then equation 7.2 shows the relation between  $R$  and  $B = \text{Br}(b \rightarrow \mu + X)$ :

$$R = \frac{N_2}{N_1} = \frac{b_1 B^2 + 2b_2 B(1-B) + b_3(1-B)^2 + b_4(\Gamma_{\text{had}}/\Gamma_{b\bar{b}} - 1)}{a_1 B^2 + 2a_2 B(1-B) + a_3(1-B)^2 + a_4(\Gamma_{\text{had}}/\Gamma_{b\bar{b}} - 1)} \quad (7.2)$$

After requiring the muons to have a  $p_t$  larger than 1 GeV, the background fraction is largely reduced. From Monte Carlo the acceptances  $a_i$  and  $b_i$  are calculated for muons with

<sup>1</sup>Dimuon events are defined as in chapter 5.

Acceptances		
$i$	$a_i$	$b_i$
1	31.9 %	13.2 %
2	33.3 %	0.3 %
3	1.4 %	0.0 %
4	0.5 %	0.0 %

Table 7.1: Monte Carlo estimates of the acceptances of each subcategory in the 1991 data sample for  $p_t > 1.0$  GeV.

$p_t > 1.0$  GeV and listed in table 7.1. The simplified picture, used to argue that  $R$  gives information on  $\text{Br}(b \rightarrow \mu + X)$  independent of  $\Gamma_{b\bar{b}}$ , is obtained by taking  $a_2 = b_1$  and all other acceptances zero which is clearly too rough a simplification, as can be seen from table 7.1. Taking  $R$  from the data sample and using table 7.1, equation 7.2 can be solved for  $\text{Br}(b \rightarrow \mu + X)$ :

$$\text{Br}(b \rightarrow \mu + X) = 0.117 \pm 0.004 \quad (7.3)$$

where the error is statistical only.

A systematic error study is performed much the same way as in the previous analysis chapters. The influence of the minimum  $p_t$  cut is investigated in the same manner as described earlier. Figure 7.1 shows  $\text{Br}(b \rightarrow \mu + X)/\text{Br}(b \rightarrow \mu + X)^0$  as a function of the minimum  $p_t$  with  $\text{Br}(b \rightarrow \mu + X)^0$  the nominal value for a minimum  $p_t$  of 1.0 GeV:  $\text{Br}(b \rightarrow \mu + X)^0 = 0.117$ . Calculating  $\sigma(\Delta N_2)$  and  $\Delta N_{\text{tot}}$ , with  $N_{\text{tot}} = N_1 + N_2$ , the change in  $\text{Br}(b \rightarrow \mu + X)$  is calculated, using the equivalent formulae of equation 6.10 and equation 6.11. As the variations in  $\text{Br}(b \rightarrow \mu + X)/\text{Br}(b \rightarrow \mu + X)^0$  are statistically inconsistent, a systematic error due to this minimum  $p_t$  cut is assigned:  $\pm 0.002$ .

The quantities obtained in the previous analysis chapters were all insensitive to the absolute normalisation of the number of events. The measurement of  $\text{Br}(b \rightarrow \mu + X)$ , however, depends strongly on this normalisation. Therefore, the uncertainty on the inclusive muon selection efficiency is investigated. Using the numbers in table 3.3, obtained as described in section 3.6, this yields a systematic error on  $\text{Br}(b \rightarrow \mu + X)$  of 0.0012. Table 7.2 summarises the systematic error study. The two major contributions to the systematic error in this table come from the uncertainty in the  $D^{**}$  abundance and from the lack of Monte Carlo events. Whereas the latter contribution can be reduced by producing more simulated events in the future, the former has to be reduced by studying the  $D^{**}$  abundance itself, either at LEP or at other colliders like DORIS and CESR.

Combining this value for  $\text{Br}(b \rightarrow \mu + X)$  with the averaged PEP/PETRA/ $L_3$  result for inclusive leptons [62], from which the  $L_3$  muon content has been extracted, a semileptonic branching ratio  $\text{Br}(b \rightarrow \ell + X) = 0.118 \pm 0.005$  is obtained. This number will be used in the subsequent sections.

Contribution	$\Delta\text{Br}(b \rightarrow \mu + X)$
Changing the definition of opposite side from $45^\circ$ to $90^\circ$	0.0021
$\text{Br}(b \rightarrow \mu + X) = 0.117 \pm 0.006$	0.0006
$\text{Br}(c \rightarrow \mu + X) = 0.096 \pm 0.012$	0.0010
$D^{**}$ abundance ( $22 \pm 7$ )%	0.0042
$\Gamma_{b\bar{b}} = 376 \pm 10$ MeV	0.0002
$\Gamma_{c\bar{c}} = 297 \pm 10$ MeV	0.0001
Selection efficiency $\pm 1.0$ %	0.0012
Variation of the background fraction by $\pm 15\%$	0.0022
Smearing of the muon momentum by $\Delta p/p = \Delta_\alpha \pm 30\%$ and smearing of the angle between the muon and the nearest jet by $(0.6 \pm 0.3)^\circ$	0.0010
Changing the fragmentation parameter $\varepsilon_b = 0.050 \pm 0.006$ and changing the fragmentation parameter $\varepsilon_c = 0.5 \pm 0.1$	0.0030
Minimum $p_t$ cut	0.0020
Monte Carlo statistics	0.0050
Total systematic error in $\text{Br}(b \rightarrow \mu + X)$	0.0083

Table 7.2: The various contributions to the systematic error of  $\text{Br}(b \rightarrow \mu + X)$  as derived by the counting method.

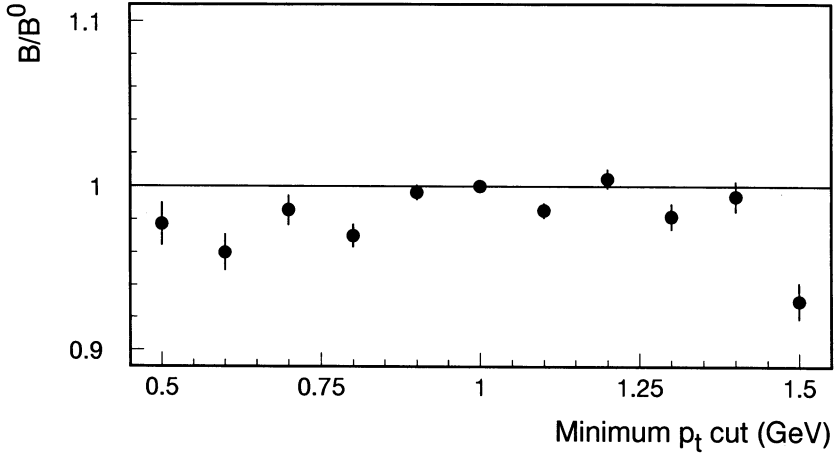


Figure 7.1: The variation of  $Br(b \rightarrow \mu + X)/Br(b \rightarrow \mu + X)^0$  as a function of the minimum  $p_t$ .

### 7.3 Determination of CKM matrix element $|V_{cb}|$

Section 1.7 describes how to determine the CKM matrix element  $|V_{cb}|$  from the  $B$ -hadron semileptonic branching ratio and its lifetime, using formula 1.35.

Figure 7.2 shows the elliptical curve in the  $|V_{cb}|$  versus  $|V_{ub}|$  plane, using the measured  $L_3$  value for  $\tau_B$  [72] and the  $B$ -hadron semileptonic branching ratio determined in the previous section. The solid line corresponds to the central values, and the dashed lines represent the one standard deviation errors, where the statistical and systematic errors have been added in quadrature. The systematic error has contributions from the measurements and from the uncertainties in the quark masses and  $\alpha_s$ . Because of the anti-correlation between  $m_b$  and  $f_c$ , the factor  $(m_b^5 f_c)$  in equation 1.35 varies by only  $\pm 12\%$  over the  $m_b$  range from 4.65 to 5.25 GeV, if the above error of  $\pm 0.02$  GeV on  $m_b - m_c$  is maintained. This has to be compared with the  $\pm 30\%$  change in  $m_b^5$  alone. However, there is much less of an anti-correlation between  $m_b$  and  $f_u$ . This explains the widening of the errors in figure 7.2 when going from the  $|V_{cb}|$  axis to the  $|V_{ub}|$  axis.

Measurements of the endpoint of the lepton momentum spectrum from  $B$ -meson semileptonic decays [76, 77] find the ratio  $|V_{ub}|/|V_{cb}|$  to be small. Model-dependent values in the range from 0.1 to 0.2 are obtained. The value of  $|V_{ub}|/|V_{cb}| = 0.15 \pm 0.10$  is used, which produces the solid straight line shown in figure 7.2. The dashed lines again correspond to the estimated error on the ratio. The two solid curves meet at a value

$$|V_{cb}| = 0.046 \pm 0.002 \pm 0.003, \quad (7.4)$$

where the first error is due to the statistical and systematic errors added in quadrature, and the second is due to uncertainties in the theory, including the errors on  $|V_{ub}|/|V_{cb}|$ ,

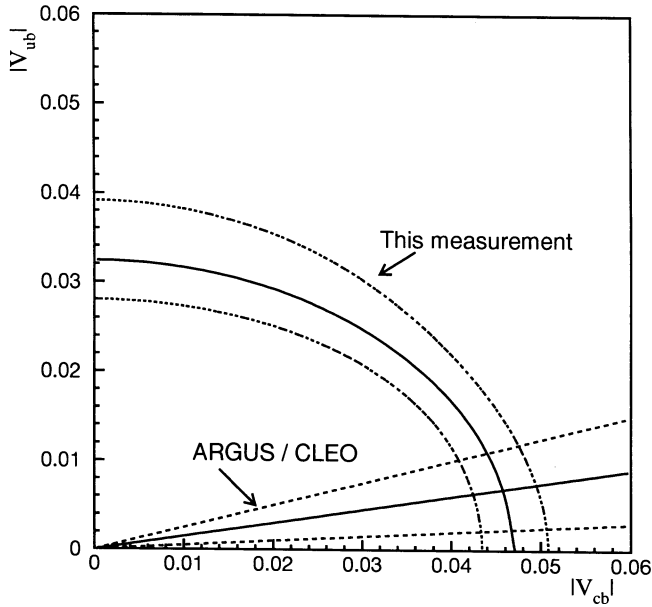


Figure 7.2: The contour plot of  $|V_{cb}|$  versus  $|V_{ub}|$ . The solid elliptical curve corresponds to the measurement of the  $B$  lifetime and the semileptonic branching ratio. The solid straight line comes from the ARGUS/CLEO measurement of  $|V_{ub}|/|V_{cb}|$ . The dashed lines correspond to one standard deviation errors, including the theoretical uncertainties.

the quark masses<sup>2</sup> and  $\alpha_s$ . This determination of  $|V_{cb}|$  is relatively insensitive to the exact value of  $|V_{ub}|/|V_{cb}|$ . Varying the ratio from 0.05 to 0.25, changes the value of  $|V_{cb}|$  by only  $\pm_{0.002}^{0.001}$ .

### Box 7.1 $\text{Br}(b \rightarrow \mu + X)$ and CKM constraint

$$\begin{aligned} \text{Br}(b \rightarrow \mu + X) &= 0.117 \pm 0.004 \text{ (stat)} \pm 0.008 \text{ (syst)} \\ |V_{cb}| &= 0.046 \pm 0.002 \pm 0.003 \end{aligned}$$

<sup>2</sup>If we use an error of 0.1 GeV on the  $m_b - m_c$ , it increases the error on  $|V_{cb}|$  due to uncertainties in the theory to  $\pm 0.004$

## 7.4 Determination of $\Gamma_{b\bar{b}}$ and $\Gamma_{c\bar{c}}$

An event by event unbinned maximum likelihood fit is performed to extract  $\Gamma_{b\bar{b}}$  and  $\Gamma_{c\bar{c}}$  from the data sample. This is done much the same way as the method used in the previous two chapters. For this fit, no  $p_t$  cut has been applied. The branching ratios  $\text{Br}(b \rightarrow \mu + X)$  and  $\text{Br}(c \rightarrow \mu + X)$  are fixed to the values of table 7.4.

The likelihood function is defined as

$$\mathcal{L} = \frac{M^N e^{-M}}{N!} \prod_{i=1}^N f(i) \quad \text{with} \quad f(i) = \frac{1}{M \cdot V_{\text{box}}(i)} \sum_k N_k(i) W_k(i) \quad (7.5)$$

in which  $f(i)$  is the probability density and  $N_k$  is the number of Monte Carlo muon events of type  $k$  found in the volume of the two dimensional box  $V_{\text{box}}(i)$  around data point  $i$  in  $(p, p_t)$  space.  $N(M)$  is the total number of data (Monte Carlo) events selected.  $M$  is normalised using the ratio of the number of selected data hadron events and the number of selected Monte Carlo hadron events.  $W_k(i)$ , the weighting function, is defined as follows:

$$W_k(i) = \frac{\Gamma_k}{\Gamma_k^0} = \tilde{\Gamma}_k \quad (7.6)$$

The normalised width for category  $k$ ,  $\tilde{\Gamma}_k$ , is given in table 7.3. Contrary to the fits described in the previous chapters, the weighting function,  $W_k(i)$ , changes the number of Monte Carlo events,  $M$ . Therefore, a normalisation factor is included, assuming that  $N$  is Poisson distributed with mean  $M$ . This gives the additional factor in the definition of  $\mathcal{L}$  with respect to equation 6.12.

The results of the likelihood fit are:

$$\Gamma_{b\bar{b}} = 386 \pm 4 \text{ MeV} \quad (7.7)$$

Category $k$	$\tilde{\Gamma}_k$
1: $b \rightarrow \mu$	$\Gamma_{b\bar{b}}/\Gamma_{b\bar{b}}^0$
2: $b \rightarrow c \rightarrow \mu$	$\Gamma_{b\bar{b}}/\Gamma_{b\bar{b}}^0$
3: $b \rightarrow \tau \rightarrow \mu$	$\Gamma_{b\bar{b}}/\Gamma_{b\bar{b}}^0$
4: $b \rightarrow \bar{c} \rightarrow \mu$	$\Gamma_{b\bar{b}}/\Gamma_{b\bar{b}}^0$
5: $b \rightarrow \text{background}$	$\Gamma_{b\bar{b}}/\Gamma_{b\bar{b}}^0$
6: $c \rightarrow \mu$	$\Gamma_{c\bar{c}}/\Gamma_{c\bar{c}}^0$
7: decay	1.0
8: punch through	1.0

Table 7.3: The normalised width used in the fit method for each category.  $\Gamma_{b\bar{b}}^0 = 376 \text{ MeV}$ ,  $\Gamma_{c\bar{c}}^0 = 297 \text{ MeV}$ .

Contribution	$\Delta\Gamma_{b\bar{b}}$ (MeV)	$\Delta\Gamma_{c\bar{c}}$ (MeV)
$\text{Br}(b \rightarrow \mu + X) = 0.118 \pm 0.005$	15	12
$\text{Br}(c \rightarrow \mu + X) = 0.096 \pm 0.012$ <sup>3</sup>	3	33
$D^{**}$ abundance $(22 \pm 7)\%$	13	16
Selection efficiency $\pm 1.0\%$	4	4
Variation of the background fraction by $\pm 15\%$	1	77
Smearing of the muon momentum by $\Delta p/p = \Delta_\alpha \pm 30\%$ and smearing of the angle between the muon and the nearest jet by $(0.6 \pm 0.3)^\circ$	3	6
Changing the fragmentation parameter $\varepsilon_b = 0.050 \pm 0.006$ and changing the fragmentation parameter $\varepsilon_c = 0.5 \pm 0.1$	2	16
Minimum number of Monte Carlo events sampled: 30 to 50	0	0
Total systematic error	21	88

<sup>3</sup>For  $\Delta\Gamma_{c\bar{c}}$   $0.096 \pm 0.006$  was taken.

Table 7.4: *The various contributions to the systematic errors as derived by the likelihood fit method.*

$$\Gamma_{c\bar{c}} = 293 \pm 10 \text{ MeV} \quad (7.8)$$

where the error is statistical only and the correlation, obtained from the fit, is  $-58\%$ .

By varying all known quantities that could contribute to the systematic error in the measurement by their measured or estimated error, the systematic errors are estimated, see table 7.4. The two largest contributions to the total systematic error on  $\Gamma_{b\bar{b}}$  originate from the uncertainty on  $\text{Br}(b \rightarrow \mu + X)$  and on the  $D^{**}$  abundance. In order to reduce the systematic error on  $\Gamma_{b\bar{b}}$  these two quantities will have to be studied in more detail. For the total systematic error on  $\Gamma_{c\bar{c}}$  the largest contribution comes from the uncertainty on the background fraction used in the Monte Carlo. In order to reduce this contribution, a special study has to be performed.

Fixing  $\Gamma_{c\bar{c}}$  to its Standard Model value of 297 MeV, the fitting method was repeated. This yielded:

$$\Gamma_{b\bar{b}} = 385 \pm 4 \text{ (stat)} \pm 24 \text{ (syst)} \text{ MeV} \quad (7.9)$$

in perfect agreement with the value obtained without constraining  $\Gamma_{c\bar{c}}$ .



### Box 7.2 Result from likelihood fit method

$$\begin{aligned}\Gamma_{b\bar{b}} &= 386 \pm 4 \text{ (stat)} \pm 21 \text{ (syst)} \text{ MeV} \\ \Gamma_{c\bar{c}} &= 293 \pm 10 \text{ (stat)} \pm 88 \text{ (syst)} \text{ MeV}\end{aligned}$$

Using  $\Gamma_{\text{had}} = 1747 \pm 11 \text{ MeV}$ [45], the ratio  $\Gamma_{b\bar{b}}/\Gamma_{\text{had}}$  equals  $0.223 \pm 0.013$ . Comparing this value and the value of  $\Gamma_{b\bar{b}}$  itself with figure 1.7 it can be concluded that  $\Gamma_{b\bar{b}}/\Gamma_{\text{had}}$  is potentially more powerful to constrain the mass of the top quark but the current accuracy does not (yet) give a constraint on  $M_t$ .

In order to check the internal consistency of the Standard Model, the  $u$  and  $d$  type quark electroweak couplings are compared. Let the combined effective coupling be defined by

$$c_f = 4(\bar{v}_f^2 + \bar{a}_f^2) \quad (7.10)$$

From the measured values of  $\Gamma_{b\bar{b}}$  and  $\Gamma_{c\bar{c}}$ ,  $c_b$  and  $c_c$  can be calculated using equations 1.9:

$$\begin{aligned}c_b &= 1.50 \pm 0.08 \\ c_c &= 1.1 \pm 0.3\end{aligned} \quad (7.11)$$

The additional top quark correction in equations 1.9 ( $\mathcal{O}(10^{-3})$ ) can be neglected at the present level of accuracy.

Figure 7.3 shows linear constraints on the  $u$  and  $d$  type quark electroweak couplings derived from the total hadronic decay width of the  $Z^0$  (thin inclined band) [45], from photon distributions in  $q\bar{q}\gamma$  events [78] (thick inclined band) and from the measurement of  $\Gamma_{b\bar{b}}$  and  $\Gamma_{c\bar{c}}$  as described in this thesis (thick vertical and horizontal bands). The Standard Model values of the couplings are shown as a solid circle. The four measurements are in perfect agreement with each other and the Standard Model prediction.

A comparison with other (LEP) experiments of the results described in this chapter and in the previous chapters is given in appendix A.

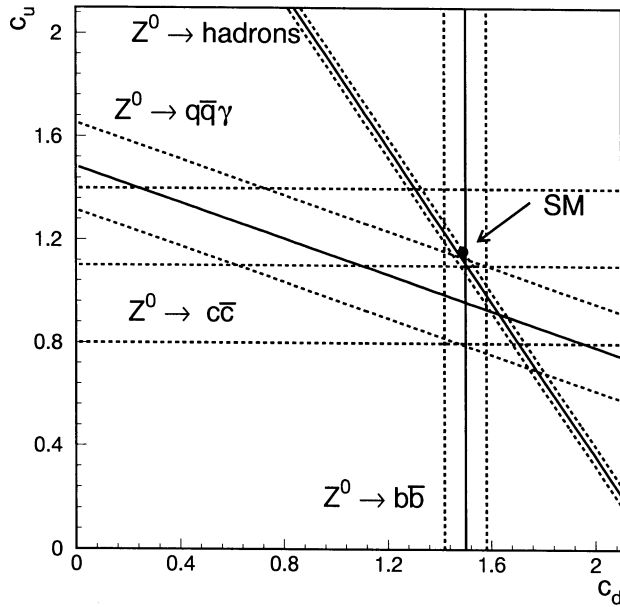


Figure 7.3: Constraints on the  $u$  and  $d$  type quark electroweak couplings derived from the total hadronic decay width of the  $Z^0$  (thin inclined band), from photon distributions in  $q\bar{q}\gamma$  events (thick inclined band) and from the measurement of  $\Gamma_{b\bar{b}}$  and  $\Gamma_{c\bar{c}}$  as described in this thesis (thick vertical and horizontal bands). The Standard Model values of the couplings are shown as a solid circle.

# Conclusion

The study of hadronic events containing  $b$  quarks, produced at the  $Z^0$  resonance, has resulted in significant improvement in the knowledge of various Standard Model parameters.

First, from studying the decay and oscillation of  $B$  hadrons constraints on three CKM matrix elements have been obtained:

$$\begin{aligned} |V_{td}/V_{ts}| &= 0.57 \pm 0.26 \\ |V_{cb}| &= 0.046 \pm 0.002 \pm 0.003 \end{aligned}$$

The result for  $|V_{cb}|$  has yielded a more stringent constraint than the previous world average, whereas the result for  $|V_{td}/V_{ts}|$  is merely consistent with it, see table A.5 in appendix A.

Furthermore, the study of the forward backward asymmetry in the production of  $b\bar{b}$  events,  $A_{b\bar{b}}$ , has resulted in a constraint on  $\sin^2 \bar{\theta}_W$  and  $M_t$ :

$$\begin{aligned} \sin^2 \bar{\theta}_W &= 0.2336 \pm 0.0029 \\ M_t &= 157 \pm 75 \pm 13 \text{ GeV} \end{aligned}$$

Indeed,  $A_{b\bar{b}}$  gives the best result on  $\sin^2 \bar{\theta}_W$  when compared with the results from the forward backward asymmetry of other fermions from the same total  $Z^0$  sample obtained by  $L_3$ . Both  $\sin^2 \bar{\theta}_W$  and  $M_t$  are consistent with the world averages (table A.6 in appendix A).

Finally, the partial width of the  $Z^0$  decaying into a  $b\bar{b}$  pair,  $\Gamma_{b\bar{b}}$ , divided by the total hadronic width,  $\Gamma_{\text{had}}$ , does not yield a competitive result for  $M_t$  due to the  $B$  decay model uncertainties.

The future outcome of the measurements as described in this thesis with increased statistics seems to be limited by systematic uncertainties, except for  $\chi_B$  and  $A_{b\bar{b}}^{\text{obs}}$ . This implies that  $\sin^2 \bar{\theta}_W$  will be determined even better from  $A_{b\bar{b}}$ . Improving the error on  $\chi_B$  by a factor three will reduce the error on the CKM matrix element constraint, obtained from  $\chi_B$ , by only a factor two due to the uncertainty on the value of  $\chi_d$ .

To improve the precision for the other quantities ( $\text{Br}(b \rightarrow \mu + X)$ ,  $\Gamma_{b\bar{b}}$ ,  $A_{c\bar{c}}$  and  $\Gamma_{c\bar{c}}$ ), more Monte Carlo events have to be produced and the quantities that have large contributions to the systematic errors have to be investigated in more detail, either at LEP or at other colliders like CESR and DORIS.

In conclusion, with the present experimental accuracy we have no reason to doubt the validity of the Standard Model as the correct theory for describing electroweak interactions.



# Appendix A

## Comparison with other (LEP) experiments

A comparison of the results of the analyses described in this thesis with those of the other LEP experiments is shown in tables A.1, A.2, A.3 and A.4. The errors mentioned in the tables is the combined statistical and systematic error. Since the partial decay widths  $\Gamma_{b\bar{b}}$  and  $\Gamma_{c\bar{c}}$  have been published in three different formats, viz.  $\Gamma_{b\bar{b}}$ ,  $\Gamma_{b\bar{b}}/\Gamma_{\text{had}}$  and  $\text{Br}(b \rightarrow \mu + X) \cdot \Gamma_{b\bar{b}}/\Gamma_{\text{had}}$  (likewise for  $c\bar{c}$ ), they are all put in the first format using  $\Gamma_{\text{had}} = 1747 \text{ MeV}$  and the semileptonic branching ratio used by the experiment itself.

The LEP values obtained for  $\chi_B$  (table A.1) and for  $A_{b\bar{b}}^{\text{obs}}$  and  $A_{c\bar{c}}$  (table A.3) are in perfect agreement. The two values obtained for  $\text{Br}(b \rightarrow \mu + X)$  are consistent. The  $L_3$  result is in very good agreement with the semileptonic branching ratios obtained at PEP and PETRA:  $\text{Br}(b \rightarrow \mu + X) = 0.117 \pm 0.010$  and  $\text{Br}(b \rightarrow e + X) = 0.121 \pm 0.010$  whereas the Delphi result is in good agreement with the semileptonic branching ratios obtained at CESR and DORIS at the  $\Upsilon(4S)$ :  $0.105 \pm 0.004[93]$ . Due to the different mixture of  $B$  hadrons at LEP compared to CESR and DORIS it is expected that the semileptonic branching ratio as measured at LEP will resemble the ones obtained at PEP and PETRA more than the results from the decay of the  $\Upsilon(4S)$ .

Although the results in table A.4 seem to be in good agreement one should be cautious in comparing the results on  $\Gamma_{b\bar{b}}$  and  $\Gamma_{c\bar{c}}$  due to the large differences in the values used for the semileptonic branching ratios: from 0.100 to 0.118.

Experiment	$\chi_B$	Remarks
This thesis/ $L_3$	$0.121 \pm 0.018$	[70]
Aleph	$0.129 \pm 0.022$	Aleph average of two methods [79]
Delphi	$0.121 \pm_{-0.043}^{0.047}$	[80]
Opal	$0.145 \pm_{-0.039}^{0.045}$	[81]

Table A.1: Comparison of the result on  $\chi_B$  described in this thesis with those published by the other LEP experiments. The error is the combined statistical and systematic error.

Experiment	$Br(b \rightarrow \mu + X)$	Remarks
This thesis	$0.117 \pm 0.009$	
Aleph	—	
Delphi	$0.100 \pm 0.010$	[80]
Opal	—	

Table A.2: Comparison of the result on  $Br(b \rightarrow \mu + X)$  described in this thesis with those published by the other LEP experiments. The error is the combined statistical and systematic error.

Experiment	$A_{b\bar{b}}^{\text{obs}}$	$A_{c\bar{c}}$	Remarks
This thesis/ $L_3$	$0.066 \pm 0.011$	$0.083 \pm 0.047$	[74]
Aleph	$0.093 \pm 0.022$	$0.064 \pm 0.049$	[82]
Delphi	$0.115 \pm 0.045$	—	[83]
Opal	$0.072 \pm 0.043$	—	Muons only [84]

Table A.3: Comparison of the results on  $A_{b\bar{b}}$  and  $A_{c\bar{c}}$  described in this thesis with those published by the other LEP experiments. The error is the combined statistical and systematic error.

Experiment	$\Gamma_{b\bar{b}}$ (MeV)	$\Gamma_{c\bar{c}}$ (MeV)	Remarks
This thesis	$386 \pm 21$	$293 \pm 89$	From lepton tagging
Aleph	$385 \pm 50$	$259 \pm_{101}^{110}$	From lepton tagging [85] ( $\Gamma_{c\bar{c}}$ from electrons only)
Delphi	—	$283 \pm 101$	From $D^*$ production [86]
	$383 \pm 41$	—	From jet shape variable [87]
	$386 \pm 45$	—	From lepton tagging [88]
	$405 \pm 31$	$264 \pm 73$	Neural nets [89]
Opal	$337 \pm 43$	$390 \pm 117$	Muons only [90]
	—	$325 \pm 70$	From $D^*$ production [91]
	$395 \pm 34$	—	Electrons only [92]

Table A.4: Comparison of the results on  $\Gamma_{b\bar{b}}$  and  $\Gamma_{c\bar{c}}$  described in this thesis with those published by the other LEP experiments. The error is the combined statistical and the systematic error.

Quantity	This thesis	Other experiments
$\chi_s$	$> 0.18$ at 90% C.L.	$> 0.4$ at 90% C.L. [94]
$\Delta M_d$	$(3.7 \pm 0.5) 10^{-4}$ eV	$(4.1 \pm 1.1) 10^{-4}$ eV [94]
$\Delta M_s$	$> 3.5 10^{-4}$ eV at 90% C.L.	—
$ V_{td}/V_{ts} $	$0.57 \pm 0.26$	$0.25 \pm 0.12$ [93] <sup>4</sup>
$ V_{cb} $	$0.046 \pm 0.002 \pm 0.003$	$0.043 \pm 0.007$ [93] <sup>4</sup>

<sup>4</sup>The results from other experiments on the CKM matrix elements have been subjected to the unitarity constraint of the CKM matrix.

Table A.5: Comparison of the results obtained from  $B$  physics described in this thesis with other experiments. The error is the combined statistical and systematic error.

Quantity	This thesis	Other experiments
$\sin^2 \bar{\theta}_W$	$0.2336 \pm 0.0029$	$0.2325 \pm 0.0008$ [93]
$M_t$	$157 \pm 75 \pm 13$ GeV	$132 \pm_{31}^{27} \pm_{19}^{18}$ [3]

Table A.6: Comparison of the results obtained from  $Z^0$  physics described in this thesis with other experiments. The error is the combined statistical and systematic error.

The (Standard Model) parameters derived from the above mentioned quantities are compared with other experiments in the table A.5 for  $B$  physics and table A.6 for  $Z^0$  physics. All values are in perfect agreement with each other.





# References

- [1] UA1 Collaboration, G. Arnison *et al.*, Phys. Lett. **B122** (1983) 103;  
UA1 Collaboration, G. Arnison *et al.*, Phys. Lett. **B126** (1983) 398;  
UA2 Collaboration, P. Bagnaia *et al.*, Phys. Lett. **B129** (1983) 130.
- [2] S.L. Glashow, Nucl. Phys. **22** (1961) 579.  
S. Weinberg, Phys. Lett. **19** (1967) 1264.  
A. Salam, in "Elementary Particle Theory" Relativistic Groups and Analyticity, ed. N. Svartholm (Almqvist and Wiksell, Stockholm, 1968) 367.
- [3] The LEP Collaborations: ALEPH, DELPHI, L3 and OPAL, Phys. Lett. **B276** (1992) 247.
- [4] P.W. Higgs, Phys. Lett. **12** (1964) 132; F. Englert and R. Brout, Phys. Rev. Lett. **13** (1964) 321.
- [5] M. Kobayashi and T. Maskawa Prog. Theor. Phys. **49** (1973) 652.
- [6] M.L. Perl *et al.*, Phys. Rev. Lett. **35** (1975) 489.
- [7] S.W. Herb *et al.* Phys. Rev. Lett. **39** (1977) 252.
- [8] ARGUS Collaboration, H. Albrecht *et al.* Phys. Lett. **B192** (1987) 245.
- [9] M. Consoli and W. Hollik in "Z Physics at LEP", CERN Report CERN-89-08, eds. G. Altarelli, R. Kleiss and C. Verzegnassi (CERN, Geneva, 1989) Vol. I, 10.
- [10] Particle Data Group, Phys. Lett. **B204** (1988).
- [11] Particle Data Group, Phys. Lett. **B239** (1990) III.49.
- [12] J. Kühn and P. Zerwas in "Z Physics at LEP", CERN Report CERN-89-08, eds. G. Altarelli, R. Kleiss and C. Verzegnassi (CERN, Geneva, 1989) Vol. I, 267.
- [13] A. Djouadi *et al.*, Z. Phys. **C46** (1990) 411.
- [14] D. Bardin *et al.*, CERN-TH 6443/92 (1992).
- [15] L3 Collaboration, B. Adeva *et al.*, Z. Phys. **C51** (1991) 179.
- [16] L3 Collaboration, B. Adeva *et al.*, Phys. Lett. **B257** (1991) 464.
- [17] P.J. Franzini, Phys. Rep. **173** (1989) 1.
- [18] OPAL Collaboration, G. Alexander *et al.*, Phys. Lett. **B264** (1991) 467.
- [19] JADE Collaboration, W. Bartel *et al.*, Z. Phys. **C20** (1983) 187.
- [20] TASSO Collaboration, M. Althoff *et al.*, Z. Phys. **C27** (1985) 27.
- [21] J.D. Bjorken, Phys. Rev. **D17** (1978) 171; M. Suzuki, Phys. Lett. **B71** (1977) 189.
- [22] B. Mele and P. Nason, Phys. Lett. **B245** (1990) 635.
- [23] B. Anderson *et al.*, Phys. Rep. **C97** (1983) 33.
- [24] R.D. Field and R.P. Feynman, Nucl. Phys. **B136** (1978) 1.  
P. Hoyer *et al.*, Nucl. Phys. **B161** (1979) 349.  
A. Ali *et al.*, Phys. Lett. **B93** (1980) 155.

- [25] G. Marchesini and B.R. Webber, Nucl. Phys. **B310** (1988) 461.
- [26] L3 Collaboration, B. Adeva *et al.*, Z. Phys. **C55** (1992) 39 and references therein.
- [27] B. Anderson *et al.*, Z. Phys. **C20** (1983) 317.
- [28] Peterson *et al.*, Phys. Rev. **D27** (1983) 105.
- [29] P. Collins and T. Spiller, J. Phys. **G11** (1985) 1289.
- [30] V.G. Kartvelishvili *et al.*, Phys. Lett. **B78** (1978) 615.
- [31] J. Chrin, Z. Phys. **C36** (1987) 163.
- [32] G. Altarelli *et al.*, Nucl. Phys. **B207** (1982) 365.
- [33] ARGUS Collaboration, H. Albrecht *et al.*, Phys. Lett. **B249** (1990) 359.
- [34] J. Kühn and P. Zerwas in "Z Physics at LEP", CERN Report CERN-89-08, eds. G. Altarelli, R. Kleiss and C. Verzegnassi (CERN, Geneva, 1989) Vol. I, 316.
- [35] B. Adeva *et al.*, Nucl. Instr. and Meth. **277** (1989) 187.
- [36] L3 Collaboration, Letter of intent (January 1982)  
L3 Collaboration, Technical Proposal (May 1983)  
L3 Collaboration, B. Adeva *et al.*, Nucl. Instr. and Meth. **A289** (1990) 121.  
"The construction of the L3 experiment".
- [37] J. Onvlee, "The behaviour of the L3 muon chambers in a magnetic field", PhD Thesis Univ. of Amsterdam (1989), unpublished.
- [38] P. Duinker *et al.*, Nucl. Instr. and Meth. **201** (1982) 351.
- [39] Y. Peng, "The muon spectrometer of the L3 detector at LEP" PhD Thesis Univ. of Amsterdam (1988), unpublished.
- [40] X. Leijtens, "Production of  $\tau^+\tau^-$  at the Z-resonance" to be published as PhD Thesis at the Univ. of Amsterdam in 1993.
- [41] D.H. Zhang, "Study of Muon Pair Production at LEP" to be published as PhD Thesis at the Univ. of Amsterdam in 1993.
- [42] O. Adriani *et al.*, Nucl. Instr. and Meth. **A302** (1991) 53.
- [43] M. Merk, "Study of Bhabha Scattering at the  $Z^0$ -Resonance using the  $L_3$  Detector", PhD Thesis Univ. of Nijmegen (1992), unpublished.
- [44] L3 Collaboration, B. Adeva *et al.*, Phys. Lett. **B275** (1992) 209.
- [45] L3 Collaboration, O. Adriani *et al.*, "Experimental Results from L3 at LEP: Electron-Positron Physics at the Z Pole", to be published in Phys. Rep.
- [46] R. Brun *et al.*, "Geant3", CERN DD/EE/84-1 (Revised), September 1987. Hadronic interactions are simulated using the GHEISHA program, see:  
H. Fesefeldt, RWTH Aachen Preprint PITHA 85/02 (1985).
- [47] R. Baily *et al.*, "LEP Energy Calibration", CERN SL/90-05 (1990).
- [48] L. Arnaudon *et al.*, "The Energy Calibration of LEP in 1991", CERN PPE/92-125, CERN SL/92-37(DI) (1992).
- [49] ALEPH Collaboration, D. Decamp *et al.*, Nucl. Instr. Meth. **A294** (1990) 121.  
"ALEPH: A Detector for Electron-Positron Annihilations at LEP".

- [50] DELPHI Collaboration, P. Aarnio *et al.*, Nucl. Instr. Meth. **A303** (1990) 233.  
"The DELPHI Detector at LEP".
- [51] OPAL Collaboration, M.Z. Akrawy *et al.*, Nucl. Instr. Meth. **A305** (1990) 275.  
"The OPAL Detector at LEP".
- [52] C. Brouwer *et al.*, Nucl. Instr. and Meth. **A313** (1992) 50.
- [53] T. Foreman. Unpublished notes, NIKHEFH (1989).
- [54] A. van Vucht, Masters Thesis Univ. of Amsterdam (1989), unpublished.
- [55] V. Innocente, M. Maire and E. Nagy, *GEANE: Average Tracking and Error Propagation Package*, CERN Program Library W5013-E, July 1991.
- [56] V. Innocente and E. Nagy, "Trajectory Fit in Presence of Dense materials", Nucl. Instr. and Meth. **A324** (1993) 297.
- [57] T.S. Dai and T. Foreman, "Determination of the Muon Chamber Efficiency in the 1990 Data", L3 note 954 (1991).
- [58] M. Hebert and G. Wang, "Efficiencies Affecting the Inclusive Lepton Analysis", L3 note 1178 (1992).
- [59] T.S. Dai, "Heavy Flavor Production in  $Z^0$  Decays" PhD Thesis Massachusetts Institute of Technology (1991), unpublished.
- [60] T. Sjöstrand and M. Bengtsson, Comput. Phys. Commun. 43 (1987) 367; T. Sjöstrand, in: "Z physics at LEP", CERN Report CERN-89-08, Vol. III, p. 143.
- [61] L3 Collaboration, B. Adeva *et al.*, Phys. Lett. **B241** (1990) 416.
- [62] L3 Collaboration, B. Adeva *et al.*, Phys. Lett. **B261** (1991) 177.
- [63] Particle Data Group, Phys. Lett. **B239** (1990) VII.113. The PETRA and PEP measurements have been averaged according to the procedure used by the Particle Data Group.
- [64] ARGUS Collaboration, H. Albrecht *et al.*, DESY 92-146 (October 1992).
- [65] CLEO Collaboration, S. Henderson *et al.*, Phys. Rev. **D45** (1992) 2212.
- [66] K.N. Qureshi, "Studying Beauty Production in  $Z^0$  Decays Using Different Fragmentation Models" PhD Thesis Quaid-I-Azam Univ. Islamabad (1993), unpublished.
- [67] B. Grinstein and M.B. Wise, Phys. Lett. **B197** (1987) 249.  
N. Isgur *et al.*, Phys. Rev. Lett. **D39** (1989) 799.
- [68] R. Wilhelm, "The L3 Event Visualisation System And Its Use In The  $Z^0$  Line Shape Analysis", PhD Thesis Univ. of Amsterdam (1992), unpublished.
- [69] R. James and M. Roos, "MINUIT Function Minimization and Error Analysis", CERN, **D506** (1989) 1.
- [70] L3 Collaboration, B. Adeva *et al.*, Phys. Lett. **B288** (1992) 395.
- [71] ARGUS Collaboration, H. Albrecht *et al.*, Z. Phys. **C55** (1992) 357;  
CLEO Collaboration, R. Fulton *et al.*, Preliminary (1992).
- [72] L3 Collaboration, B. Adeva *et al.*, Phys. Lett. **B270** (1991) 111.
- [73] J. Kühn and P. Zerwas in "Z Physics at LEP", CERN Report CERN-89-08, eds. G. Altarelli, R. Kleiss and C. Verzegnassi (CERN, Geneva, 1989) Vol. I, 353.
- [74] L3 Collaboration, B. Adeva *et al.*, Phys. Lett. **B292** (1992) 454.

- [75] L3 Collaboration, O. Adriani *et al.*, Phys. Lett. **B294** (1992) 466.
- [76] CLEO Collaboration, R. Fulton *et al.*, Phys. Rev. Lett. **64** (1990) 16.
- [77] ARGUS Collaboration, H. Albrecht *et al.*, Phys. Lett. **B255** (1991) 297.
- [78] L3 Collaboration, O. Adriani *et al.*, CERN-PPE/92-209 (1992).
- [79] Aleph Collaboration, D. Buskulic *et al.*, Phys. Lett. **B284** (1992) 177.
- [80] Delphi Collaboration, P. Abreu *et al.*, CERN-PPE/92-203 (1992).
- [81] Opal Collaboration, P.D. Acton *et al.*, Phys. Lett. **B276** (1992) 379.
- [82] Aleph Collaboration, D. Buskulic *et al.*, Phys. Lett. **B263** (1991) 112.
- [83] Delphi Collaboration, P. Abreu *et al.*, Phys. Lett. **B276** (1992) 536.
- [84] Opal Collaboration, P.D. Acton *et al.*, Phys. Lett. **B263** (1991) 311.
- [85] Aleph Collaboration, D. Buskulic *et al.*, Phys. Lett. **B244** (1990) 551.
- [86] Delphi Collaboration, P. Abreu *et al.*, Phys. Lett. **B252** (1990) 140.
- [87] Delphi Collaboration, P. Abreu *et al.*, Phys. Lett. **B281** (1992) 383.
- [88] Delphi Collaboration, P. Abreu *et al.*, Z. Phys. **C56** (1992) 47.
- [89] Delphi Collaboration, P. Abreu *et al.*, Phys. Lett. **B295** (1992) 383.
- [90] Opal Collaboration, P.D. Acton *et al.*, Phys. Lett. **B263** (1991) 311.
- [91] Opal Collaboration, P.D. Acton *et al.*, Phys. Lett. **B262** (1991) 341.
- [92] Opal Collaboration, P.D. Acton *et al.*, Z. Phys. **C55** (1992) 191.
- [93] Particle Data Group, Phys. Rev. **D45**, Part 2, (1992).
- [94] H. Schröder, Rep. Prog. Phys. **52** (1989) 765.

# Summary

This thesis describes the study of heavy flavour production, in particular the production of the bottom quark, at the  $Z^0$  resonance.

The theory describing the interactions between all fundamental particles, called the Standard Model, is shortly described in the first chapter. The production of bottom quarks at LEP, the Large Electron Positron collider at CERN, is dominated by the  $Z^0$  exchange and the study of this process is one of the goals of this thesis. The theoretical expressions for the cross section and the forward backward asymmetry are given. After the electroweak production of the quarks a process called fragmentation takes place forming the detectable hadrons. The phenomenological models invented to describe this process are explained.  $B^0\bar{B}^0$  mixing, a second order process in which a  $B$  meson oscillates between two mass eigenstates, is modeled and the decay of  $B$  hadrons is described.

The second chapter describes the  $L_3$  experiment. A detailed description of the  $L_3$  muon detector is given together with the other subdetectors. The  $L_3$  muon detector consists of two Ferris wheels each containing eight independent units called octants. Each octant is made out of five precision drift chambers. There are two chambers in the outer layer, two chambers in the middle and one inner chamber. These chambers measure the track coordinates in the bending plane. In addition, the top and bottom covers of the inner and outer chambers are made of (less precise) drift chambers and they measure the coordinate along the beam. The detector is completed with a central detector, an electromagnetic and hadron calorimeter, scintillation counters and a luminosity monitor. The data flow is clarified and the general  $L_3$  software packages for simulation and reconstruction of the data are described.

Chapter 3 is dedicated to the  $L_3$  muon simulation and reconstruction. First, the simulation of muons traversing the muon detector, yielding signals in the same format as the real detector, is described. Tracks in the muon chambers are reconstructed in several steps. During the first step the reconstruction is limited to the individual P and Z chambers. Two dimensional pattern recognition is performed yielding candidate track segments: P segments in  $xy$  and Z segments in  $yz$ . For this purpose a "drift time drift distance" relationship is exploited. In the next step, these segments are associated with one another to form three dimensional track candidates. The combination of the information from the muon chambers and the other subdetectors is explained. Chapter 3 finishes with the resolution of the muon chamber system and the differences found between the simulated and real muon data.

In chapter 4, the selection of heavy flavours is discussed, followed by a detailed study of the Monte Carlo and event samples thus obtained. The event selection is focused mainly on selecting  $e^+e^- \rightarrow b\bar{b}$  events, but as  $e^+e^- \rightarrow c\bar{c}$  events are not rejected rigorously by this selection, most of them are still present in the sample. Bottom quark events are selected by first requiring them to pass the hadronic selection criteria. Once the event has passed this requirement, heavy flavours are selected by the "lepton tagging" method. This method

relies upon certain properties of the lepton to indicate the production of a heavy quark pair. Since the production of inclusive taus is very small and the tau life time very short as compared to muons and electrons, only the latter leptons are suited for this kind of analysis. This thesis focuses on the part of the analysis that is done by muon tagging only. The above mentioned procedure results in a 83% pure  $b\bar{b}$  sample with a total efficiency of 35%.

The mixing parameter,  $\chi_B$ , is determined in chapter 5. In the simplified picture with all inclusive muons from prompt  $b \rightarrow \mu$  decay, an event with two like charge inclusive muons is a signature for  $B^0\bar{B}^0$  mixing since the promptly produced muons propagate the sign of the  $b$  quark contained in the  $B$  meson. Therefore, two high  $p_t$  opposite side same charge muons are a signature for an event in which a  $B^0\bar{B}^0$  transition took place. Two methods are used to measure this mixing parameter  $\chi_B$ . One is based on counting the number of high  $p_t$  dimuon events with the same charge as compared to the number with opposite charge and serves as a cross check for the second method. The second method is based on a four dimensional fit to the complete  $p$  and  $p_t$  spectra of the dimuons which uses the full information of the event but requires large Monte Carlo statistics to accurately determine the probability functions used by this method. The former method results in  $\chi_B = 0.090 \pm 0.029 \pm 0.012$  where the first error is statistical and the second systematic. The latter method yields  $\chi_B = 0.118 \pm 0.027 \pm 0.008$ , in good agreement. Combining this result with the inclusive electrons, gives the  $L_3$  value,  $\chi_B = 0.121 \pm 0.017 \pm 0.006$ . This together with mixing results from ARGUS and CLEO constrains two Cabibbo-Kobayashi-Maskawa matrix elements:  $|V_{td}/V_{ts}| = 0.56 \pm 0.26$ .

In chapter 6, the observed forward backward asymmetry,  $A_{b\bar{b}}^{\text{obs}}$ , is measured, which together with the mixing parameter gives the forward backward asymmetry  $A_{b\bar{b}}$ . The  $b$  quark asymmetry is determined in two ways. The first, based on a simple method, yields  $A_{b\bar{b}} = 0.086 \pm 0.022 \pm 0.009$ . Since the data contains  $c\bar{c}$  events, the forward backward asymmetry for  $e^+e^- \rightarrow c\bar{c}$ ,  $A_{c\bar{c}}$ , can also be measured with the second, more complicated, method:  $A_{b\bar{b}} = 0.088 \pm 0.020 \pm 0.008$  and  $A_{c\bar{c}} = 0.095 \pm 0.039 \pm 0.028$ . Both methods are in perfect agreement. Having obtained  $A_{b\bar{b}}$ , the Standard Model weak mixing angle and the top quark mass are calculated after including the  $L_3$  inclusive electron results:  $\sin^2 \bar{\theta}_W = 0.2336 \pm 0.0029$  and  $M_t = 157 \pm 75 \pm 13$  GeV.  $A_{b\bar{b}}$  gives the best result on  $\sin^2 \bar{\theta}_W$  when compared with the results from the forward backward asymmetry of other fermions from the same total  $Z^0$  sample obtained by  $L_3$ .

The branching ratio  $\text{Br}(b \rightarrow \mu + X)$  is determined in chapter 7. Like the mixing parameter, this quantity serves two purposes as well: it constrains the quark mixing angles and it allows for determining the partial width of the  $Z^0$  decaying into a  $b\bar{b}$  pair,  $\Gamma_{b\bar{b}}$ , both described in the same chapter. Apart from  $\Gamma_{b\bar{b}}$ ,  $\Gamma_{c\bar{c}}$  is also extracted from the data. The branching ratio is calculated by counting the number of events with two inclusive muons and the events with just one inclusive muon. The ratio of these two numbers is, to first order, proportional to the branching ratio and results in  $\text{Br}(b \rightarrow \mu + X) = 0.117 \pm 0.004 \pm 0.008$ . Combining this with the PEP/PETRA and  $L_3$  inclusive electron results gives  $\text{Br}(b \rightarrow \ell + X) = 0.118 \pm 0.005$ . This result and the measured  $L_3$  value for the  $B$  hadron lifetime constrains the Cabibbo-Kobayashi-Maskawa matrix element  $V_{cb}$ :  $|V_{cb}| = 0.046 \pm 0.002 \pm 0.003$ . Finally  $\Gamma_{b\bar{b}}$  and  $\Gamma_{c\bar{c}}$  are calculated, yielding  $\Gamma_{b\bar{b}} = 386 \pm 4 \pm 21$  MeV and  $\Gamma_{c\bar{c}} = 293 \pm 10 \pm 88$  MeV, in good agreement with the Standard Model predictions of 376 MeV and 297 MeV

respectively.

In conclusion, the study of hadronic events containing  $b$  quarks, produced at the  $Z^0$  resonance, has resulted in significant improvement in the knowledge of various Standard Model parameters. Even with the present experimental accuracy we have no reason to doubt the validity of the Standard Model as the correct theory for describing electroweak interactions.





# Samenvatting

Dit proefschrift beschrijft het onderzoek naar de productie van zware quarks, met name de productie van bottom quarks, bij de  $Z^0$  resonantie.

De theorie die de interacties beschrijft tussen alle fundamentele deeltjes, het zogenaamde Standaard Model, wordt in het kort beschreven in het eerste hoofdstuk. De productie van bottom quarks in LEP, de Large Electron Positron botser te CERN, wordt gedomineerd door het uitwisselen van het  $Z^0$  deeltje en de studie van dit proces vormt een van de onderwerpen van dit proefschrift. De theoretische formules voor de werkzame doorsnede en voorwaartse achterwaartse asymmetrie worden gegeven. Na de electrozwakke productie van de quarks, vindt er een proces plaats dat fragmentatie heet. Tijdens dit proces worden de waarneembare hadronen gevormd. De fenomenologische modellen die hiervoor zijn bedacht worden beschreven.  $B^0\bar{B}^0$  menging, een tweede orde proces waarbij een  $B$  meson oscilleert tussen twee massa eigentoestanden, en het verval van  $B$  hadronen worden beschreven.

Het tweede hoofdstuk beschrijft het  $L_3$  experiment. Een gedetailleerde beschrijving van de  $L_3$  muon detector en de andere subdetectoren wordt gegeven. De  $L_3$  muon detector bestaat uit twee grote "wielen" die elk acht onafhankelijke delen bevat en die octanten worden genoemd. Elk octant is opgebouwd uit vijf precisie driftkamers. Er zijn twee kamers opgenomen in de buitenste laag, twee kamers in de middelste laag en één kamer in de binnenste. Daar aan toegevoegd zijn (minder precieze) drift kamers die de coördinaten parallel aan de bundellijn meten. Deze kamers vormen de onder en boven laag van de binnenste en buitenste kamers. De detector wordt gecompleteerd door een binnen detector, een electromagnetische en hadronische calorimeter, scintillatie tellers en een luminositeits meter. De informatiestroom wordt toegelicht en de algemene  $L_3$  datasimulatie en -reconstructie software pakketten worden beschreven.

Hoofdstuk 3 is gewijd aan de  $L_3$  muonsimulatie en -reconstructie. Allereerst wordt de simulatie van muonen in de muon detector beschreven. Sporen in de muon kamers worden gereconstrueerd in een aantal stappen. Tijdens de eerste stap beperkt de reconstructie zich tot één enkele P of Z kamer. Patroonherkenning wordt uitgevoerd in twee dimensies hetgeen een kandidaat spoorsegment oplevert: P segmenten in  $xy$  en Z segmenten in  $yz$ . Hiervoor wordt een "drifttijd-driftafstand" relatie gebruikt. In de volgende stap worden deze segmenten gecombineerd tot een drie dimensionaal spoor. Vervolgens wordt er dan gebruik gemaakt van de informatie uit de andere subdetectoren. Hoofdstuk 3 eindigt met de resolutie van het muon kamer systeem en de verschillen tussen gesimuleerde en echte muon data.

In hoofdstuk 4 wordt de selectie van zware quarks beschreven, gevolgd door een studie van de Monte Carlo en data gebeurtenissen. De selectie van dergelijke gebeurtenissen is voornamelijk gericht op het selecteren van  $e^+e^- \rightarrow b\bar{b}$  gebeurtenissen, maar aangezien  $e^+e^- \rightarrow c\bar{c}$  gebeurtenissen niet rigoreus worden geëlimineerd, zijn de meeste van hen nog aanwezig in de geselecteerde verzameling. Bottom quarks worden geselecteerd door eerst

de hadronische selectie-eisen op te leggen. Uit de gebeurtenissen, die aan deze voorwaarden voldoen, worden de zware quarks geselecteerd met behulp van de "lepton identificatie" methode. Deze methode berust op het feit dat bepaalde eigenschappen van het lepton duiden op de productie van een zwaar quarkpaar. Aangezien de productie van inclusieve tau's heel laag is en de tau levensduur zeer kort vergeleken met electronen en muonen zijn alleen de laatst genoemde leptonen bruikbaar in deze methode. Dit proefschrift beschrijft dat deel van de analyse dat gedaan is met muon identificatie. De boven beschreven methode levert een 83% zuivere  $b\bar{b}$  verzameling gebeurtenissen op met een totale efficiëntie van 35%.

De mengparameter,  $\chi_B$ , wordt bepaald in hoofdstuk 5. In het eenvoudige geval waarin alle inclusieve muonen directe  $b \rightarrow \mu$  muonen zijn, is een gebeurtenis met twee gelijk geladen muonen een teken voor  $B^0\bar{B}^0$  menging aangezien direct geproduceerde muonen de lading van het  $b$  quark in het  $B$  hadron propageren. Daarom zijn twee hoge  $p, p_t$  tegengesteld gerichte gelijk geladen muonen een teken voor een gebeurtenis waarin een  $B^0\bar{B}^0$  overgang plaatsvond. Twee methoden worden gebruikt om deze mengparameter  $\chi_B$  te meten. Eén is gebaseerd op het tellen van het aantal hoge  $p_t$  dimuon gebeurtenissen met de zelfde lading vergeleken met het aantal tegengesteld geladen muon gebeurtenissen en dient als controle voor de tweede methode. De tweede methode is gebaseerd op een vier dimensionele fit aan het complete  $p$  en  $p_t$  spectrum van de dimuonen en gebruikt alle informatie. Deze methode heeft grote hoeveelheden gesimuleerde gebeurtenissen nodig. De eerst genoemde methode levert  $\chi_B = 0.090 \pm 0.029 \pm 0.012$  op waarbij de eerste fout statistisch is en de tweede systematisch. De tweede methode geeft  $\chi_B = 0.118 \pm 0.027 \pm 0.008$ , in goede overeenstemming met de eerste. Door dit resultaat te combineren met het resultaat van de  $L_3$  inclusieve electronen, krijgt men het  $L_3$  resultaat:  $\chi_B = 0.121 \pm 0.017 \pm 0.006$ . Dit, samen met de resultaten van ARGUS en CLEO, begrenst twee Cabibbo-Kobayashi-Maskawa matrix elementen:  $|V_{td}/V_{ts}| = 0.56 \pm 0.26$ .

In hoofdstuk 6, wordt de waargenomen voorwaartse achterwaartse asymmetrie gemeten, die samen met de mengparameter de voorwaartse achterwaartse asymmetrie  $A_{b\bar{b}}$  geeft. De  $b$  quark asymmetrie wordt op twee manieren bepaald. De eerste, gebaseerd op een simpele methode, geeft  $A_{b\bar{b}} = 0.086 \pm 0.022 \pm 0.009$ . Aangezien de verzameling gebeurtenissen ook  $c\bar{c}$  events bevat, kan met de tweede, ingewikkeldere, methode ook de voorwaartse achterwaartse asymmetrie voor  $e^+e^- \rightarrow c\bar{c}$ ,  $A_{c\bar{c}}$ , bepaald worden:  $A_{b\bar{b}} = 0.088 \pm 0.020 \pm 0.008$  en  $A_{c\bar{c}} = 0.095 \pm 0.039 \pm 0.028$ . Beide methoden zijn in perfecte overeenstemming. Na  $A_{b\bar{b}}$  bepaald te hebben, worden de Standaard Model zwakke menghoek en de top quark massa uitgerekend, na het resultaat van de  $L_3$  inclusieve electronen te hebben toegevoegd:  $\sin^2 \bar{\theta}_W = 0.2336 \pm 0.0029$  en  $M_t = 157 \pm 75 \pm 13$  GeV.  $A_{b\bar{b}}$  geeft het beste resultaat voor  $\sin^2 \bar{\theta}_W$  vergeleken met de resultaten zoals verkregen uit de voorwaartse achterwaartse asymmetrie van andere fermionen van dezelfde totale  $L_3 Z^0$  verzameling.

De vertakkingsverhouding  $\text{Br}(b \rightarrow \mu + X)$  wordt bepaald in hoofdstuk 7. Net als de mengparameter, dient de bepaling van deze grootte ook twee doelen: het begrenst de quark menghoeken en het maakt de bepaling van de partiële vervalsbreedte van de  $Z^0$  in een  $b\bar{b}$  paar,  $\Gamma_{b\bar{b}}$ , mogelijk. Naast  $\Gamma_{b\bar{b}}$  wordt ook  $\Gamma_{c\bar{c}}$  bepaald.  $\text{Br}(b \rightarrow \mu + X)$  wordt uitgerekend door het aantal gebeurtenissen te tellen met twee inclusieve muonen en met maar één inclusief muon. De verhouding van deze twee getallen is, in eerste benadering, evenredig met  $\text{Br}(b \rightarrow \mu + X)$  en geeft:  $\text{Br}(b \rightarrow \mu + X) = 0.117 \pm 0.004 \pm 0.008$ .

Door dit te combineren met de PEP/PETRA en de  $L_3$  inclusieve electronen resultaten krijgt men:  $\text{Br}(\bar{b} \rightarrow \ell + X) = 0.118 \pm 0.005$ . Door dit weer te combineren met de  $L_3$   $B$  hadron levensduur wordt het Cabibbo-Kobayashi-Maskawa matrix element  $V_{cb}$  bepaald:  $|V_{cb}| = 0.046 \pm 0.002 \pm 0.003$ . Als laatste worden  $\Gamma_{b\bar{b}}$  en  $\Gamma_{c\bar{c}}$  uitgerekend:  $\Gamma_{b\bar{b}} = 386 \pm 4 \pm 21$  MeV en  $\Gamma_{c\bar{c}} = 293 \pm 10 \pm 88$  MeV, in goede overeenstemming met de voorspellingen van het Standaard Model: 376 MeV en 297 MeV respectievelijk.

Concluderend, heeft de studie van hadronische events met  $b$  quarks, geproduceerd bij de  $Z^0$  resonantie, een significante verbetering opgeleverd voor enkele Standaard Model parameters. Zelfs met de huidige experimentele nauwkeurigheid hebben we geen reden om het Standaard Model, als theorie voor het beschrijven van de electrozwakke interacties, in twijfel te trekken.



# Acknowledgements

My gratitude is expressed to all who contributed, directly or indirectly, to the results described in this thesis. From all the people I met at CERN, I would like to thank in particular, Jim Branson, Ian Brock, Bob Clare, Tiesheng Dai, Vincenzo Innocente, my copromotor, Howard Stone and Patty McBride. Our discussions, the results of which can be found in this thesis, have enlarged my insights a lot.

I owe my promotor Piet Duinker special thanks for the many inspiring sessions, in which I was forced to write down my results as accurate as possible. I have appreciated very much the careful reading of the manuscript and the suggestions given by Graziano Massaro.

I want to thank my (former) NIKHEF-H  $L_3$  colleagues: Zhang Dehong, who made it into Italy thanks to Ruud Gullit and with whom I could always discuss all software and analysis problems, Frits Ern , who introduced me to the interesting field of  $B$  physics, Xaveer Leijtens, who "beat" me in becoming a father and could therefore offer me parental advice, Hans Onvlee, who introduced me to the  $L_3$  muon software, Ren  Wilhelm, who showed me the first principles of the POSTSCRIPT page description language, Monty IJzerman, whose bad french made me get shot at, Bob van der Zwaan, my "successor", who offered me lots of help from CERN when I was in Amsterdam and Gerjan Bobbink, Bram Bouwens, Theo Driever, Frank Filthaut, Detlev Hauschildt, Els Koffeman, Herv  Kuyten, Frank Linde, Marcel Merk, Yue Peng, Gerhard Raven, Raymond Rosmalen and Wim van Rossum, for their pleasant company.

I would also like to thank Bernard de Wit, who got me in contact with the  $L_3$  group in Amsterdam.

I have appreciated the help from the computer group and the secretaries at NIKHEF-H.

I thank my parents for arousing my interest in physics and my in-laws for their support over the last ten years.

Margret and Yuri. Margret, I thank for her love, her continuous support and patience, also at times when I left her alone in Holland. Yuri, I thank for his always available smile just when I needed it most. He is an inspiration for life.



1. De bewering dat  $b\bar{b}$  gebeurtenissen even zuiver (75%) edoch efficiënter, en wel 40%, geselecteerd kunnen worden met een  $p_t/E_{\text{jet}}$  snede in plaats van een  $p_t$  snede is onjuist.  
*T. Aziz, Phys. Lett. B265 (1991) 445.*
2. Om onderscheid te kunnen maken tussen de diverse fragmentatie schaalfuncties is ongeveer 10 keer zoveel LEP data nodig als in 1991 voorhanden.
3.  $A_{b\bar{b}}$  geeft het beste resultaat voor  $\sin^2 \bar{\theta}_W$  vergeleken met de resultaten zoals verkregen uit de voorwaartse achterwaartse asymmetrie van andere fermionen van dezelfde totale  $L_3 Z^0$  verzameling.  
*Dit proefschrift.*
4. De massieve Yang-Mills theorie zonder Higgs bosonen zoals gepresenteerd door Delbourgo en Thompson is niet renormaliseerbaar.  
*R. Delbourgo and G. Thompson, Phys. Rev. Lett. 21 (1986) 2610.*
5. Met de huidige experimentele nauwkeurigheid hebben we geen reden om het Standaard Model, als theorie voor het beschrijven van de electrozwakke interacties, in twijfel te trekken.  
*Dit proefschrift.*
6. Bij de instelling van het AIO- en OIO-schap is het proefschrift, in de vorm zoals we die nu kennen, als wetenschappelijke (dubbel)publicatie achterhaald.  
*H.H.M. de Boer, G. Henneman en P.E. Voorhoeve, Ned. Tijdschr. Geneeskd. 137, nr. 12 (1993) 612.*
7. Cervonzuur, 22:6n-3, is een essentieel vetzuur voor premature pasgeborenen.
8. Het is praktisch gezien onmogelijk om de tijdsafhankelijke gebreken van een detector te simuleren.
9. Bij het schrijven, onderhouden en documenteren van de LHC software is het gebruik van een CASE tool onvermijdelijk.
10. Onderdeel 35, de geleidingsrail van de kofferdeksel, op pagina 74 in de geïllustreerde originele VW1302/1303 onderdelen catalogus (1991) deugt niet (roest rust niet).
11. Wedstrijddansen is topsport.
12. De eerste keer is juist daarom zo aantrekkelijk omdat er pas daarna meer kunnen volgen.

# Stellingen

behorende bij het proefschrift:

Bottom quark production  
at the Z resonance

OP DINSDAG 22 JUNI 1993 TE 10.30 UUR TE  
VERDEDIGEN DOOR TIM FOREMAN IN DE AULA DER  
UNIVERSITEIT VAN AMSTERDAM, OUDE LUTHERSE  
KERK, INGANG SINGEL 411, HOEK SPUI.



# Curriculum Vitae

De auteur van dit proefschrift werd geboren op 29 oktober 1964 te Haarlem. Hij behaalde in 1983 het diploma Gymnasium  $\beta$  aan het Stedelijk Lyceum te Maastricht. In dat jaar begon hij de studie natuur- en wiskunde aan de Rijksuniversiteit Utrecht. Na het propedeutisch examen natuurkunde met fundamentele wiskunde (1984) behaalde hij in 1988 het doctoraalexamen theoretische natuurkunde. De afstudeerscriptie onder leiding van prof. dr. B.Q.P.J. de Wit betrof een theoretisch onderzoek naar de mogelijkheid van een massieve Yang-Mills theory zonder Higgs bosonen.

Van 1988 tot 1993 was de auteur, eerst in dienst van het FOM later van de UvA, werkzaam als wetenschappelijk medewerker aan het "Nationaal Instituut voor Kernfysica en Hoge-Energie Fysica (NIKHEF-H)" in Amsterdam. Tijdens dit promotie-onderzoek bezocht hij de 1989 Hoge Energie Fysica Aken-België-Nederland Zomerschool, te Chevetogne, België en de 1992 CERN school of Computing te l'Aquila, Italië. Op de "QCD, 20 years later" workshop te Aken, 9 – 13 juni 1992, presenteerde hij de LEP (Aleph, Delphi,  $L_3$ , OPAL) "Heavy Flavour Fragmentation at LEP" resultaten.

De resultaten van het onderzoek dat hij in deze periode verrichtte zijn voor het merendeel vervat in dit proefschrift.